



T.C.
MANİSA CELAL BAYAR ÜNİVERSİTESİ
FEN BİLİMLERİ ENSTİTÜSÜ

MANİSA CELAL BAYAR UNIVERSITY
INSTITUTE OF NATURAL&APPLIED
SCIENCE

CİLT:19 SAYI:2 YIL:2023
VOLUME:19 ISSUE:2 YEAR:2023

ISSN: 1305-130X
e-ISSN: 1305-1385

**CELAL BAYAR ÜNİVERSİTESİ
FEN BİLİMLERİ DERGİSİ**

**CELAL BAYAR UNIVERSITY
JOURNAL OF SCIENCE**

**CELAL BAYAR
ÜNİVERSİTESİ**

Journal of Science

Volume: 19, Issue: 2, Year: 2023

Contact

Manisa Celal Bayar University
Institute of Natural and Applied Sciences
Campus of Şehit Prof Dr İlhan Varank 45140 Yunussemre – MANİSA, TÜRKİYE
Tel: (00 90) 236 201 27 05
Fax: (00 90) 236 241 21 49
e-mail: cbujos@gmail.com
Web: <https://dergipark.org.tr/tr/pub/cbayarfbe>

“CBU Journal of Science is indexed by ULAKBIM-TUBITAK TR-DIZIN”



ISSN 1305-130X

E-ISSN 1305-1385

CBUJOS is published quarterly at Manisa Celal Bayar University Printing House

“CBU Journal of Science is a refereed scientific journal”



Celal Bayar University Journal of Science

Owner

Manisa Celal Bayar University,

Editors : Prof. Dr. Kamil ŞİRİN

Assoc. Prof. Dr.. Emine KEMİKLİOĞLU

Assistant Editor: Assoc. Prof. Dr. Mustafa AKYOL

Layout and Language Editor & Secretary

Assoc. Prof. Dr. İlker Çetin KESKİN

Subject Editors

Prof. Dr. Abdullah AKDOĞAN, Pamukkale University, Chemical Engineering

Prof. Dr. Ayhan ORAL, Çanakkale Onsekiz Mart University, Chemistry

Prof. Dr. Ali DEMİR, Manisa Celal Bayar University, Civil Engineering

Prof. Dr. Fatih KALYONCU, Manisa Celal Bayar University, Mathematics

Prof. Dr. Fatih KALYONCU, Manisa Celal Bayar University, Biology

Prof. Dr. Halil BABACAN, Manisa Celal Bayar University, Physics

Prof. Dr. Mehmet ÇEVİK, Katip Çelebi University, Mechanical Engineering

Prof. Dr. Mustafa CAN, Katip Çelebi University, Bioengineering

Prof. Dr. Oğuz GÜRSOY; Mehmet Akif Ersoy University, Food Engineering

Prof. Dr. Sezai TAŞKIN, Manisa Celal Bayar University, Electrical and Electronic Engineering

Prof. Dr. Şerafettin DEMİÇ, Katip Çelebi University, Materials Engineering

Assoc. Prof. Dr. İbrahim Fadıl SOYKÖK, Manisa Celal Bayar University, Mechatronics Engineering

Assoc. Prof. Dr. İzzet YÜKSEK, Manisa Celal Bayar University, Architecture

Assoc. Prof. Dr. Mehmet Ali ILGIN, Manisa Celal Bayar University, Industrial Engineering

Assoc. Prof. Dr. Tuğba ÖZACAR ÖZTÜRK, Manisa Celal Bayar University, Computer Engineering

International Scientific Advisory Board

Prof. Dr. Arianit REKA; State University of Tetova, Macedonia

Prof. Dr. Tomasz NIEMIEC; Warsaw University of Life Sciences, Poland

Prof. Dr. Alyani ISMAIL; Universiti Putra, Malaysia

Prof. Dr. Iuliana APRODU; Dunarea de Jos University, Romania

Assoc. Prof. Can BAYRAM; University of Illinois, USA

Assoc. Prof. Dr. Johanan Christian PRASANNA; Madras Christian College, South India

Assoc. Prof. Dr. Noureddine ISSAOUI; Université de Monastir, Tunisie.

Assoc. Dr. Edward Albert UECKERMANN; North-West University, South Africa

Assoc. Dr. Zhi-Qiang ZHANG; The University of Auckland, Holland

Assist. Prof. Dr. Young Ki KIM; Pohang University of Science and Technology, South Korea

Assist. Prof. Dr. Mona MIRHEYDARI; Rutgers University, USA

Assist. Prof. Dr. Donatella ALBANESE; Università Degli Studi Di Salerno, Italy

Assist. Prof. Dr. Jinghua JIANG; The University of Memphis, USA

Assist. Prof. Dr. Jens OLDELAND; University of Hamburg, Germany

Dr. Cheng CHENG; Apple Inc., USA

Dr. Sajedah AFGHAH; Microsoft Corporation, USA

Dr. Jinghua JIANG; The University of Memphis

National Scientific Advisory Board

Prof. Dr. Mustafa Ersöz; Selçuk University

Prof. Dr. Oğuz Gürsoy; Mehmet Akif University

Prof. Dr. Mehmet Çevik; İzmir Katip Çelebi University

Prof. Dr. Sezgin Çelik; Yıldız Teknik University

Prof. Dr. Osman Dayan; Çanakkale Onsekiz Mart University

Prof. Dr. Serdar İplikçi; Pamukkale University

Prof. Dr. Yasin Üst; Yıldız Teknik University

Prof. Dr. Mahmut Kuş; Konya Teknik University

Prof. Dr. Ertunç Gündüz; Hacettepe University

Prof. Dr. Tülin Aydemir; Manisa Celal Bayar University

Prof. Dr. Sezai Taşkın; Manisa Celal Bayar University

Prof. Dr. Fatma Şaşmaz Ören; Manisa Celal Bayar University

Prof. Dr. Fatih Selimefendigil; Manisa Celal Bayar University

Prof. Dr. Osman Çulha; Manisa Celal Bayar University

Prof. Dr. Ali Konuralp; Manisa Celal Bayar University

Prof. Dr. Erol Akpınar; Abant İzzet Baysal University

Prof. Dr. Ali Demir; Manisa Celal Bayar University

Prof. Dr. Serap Derman; Yıldız Teknik University

Assoc. Prof. Dr. Fatih Doğan; Çanakkale Onsekiz Mart University

Assoc. Prof. Dr. Yeliz Yıldırım; Ege University

Assoc. Prof. Dr. Hayati Mamur; Manisa Celal Bayar University

Assoc. Prof. Dr. Özlem Çağındı; Manisa Celal Bayar University

Assoc. Prof. Dr. Mehmet Söylemez; Adıyaman University

Assoc. Prof. Dr. Nil Mansuroğlu; Ahi Evran University

Assist. Prof. Dr. Zeynep Çipiloğlu Yıldız; Manisa Celal Bayar University



CBU Journal of Science

Celal Bayar University Journal of Science (CBUJOS) covers scientific studies in the fields of Engineering and Science and publishes accounts of original research articles concerned with all aspects of experimental and theoretical studies. CBU Journal of Science is a refereed scientific journal published four times annually (March, June, September and December) by Institute of Natural and Applied Sciences of Manisa Celal Bayar University. CBU Journal of Science considers the original research articles written in English for evaluation.

CBU Journal of Science is indexed by TUBİTAK ULAKBİM TR-DİZİN, and also is included in DOAJ, Cite Factor, Journal TOCS, Advanced Science Index and OAJI databases. Digital Object Identifier (DOI) number will be assigned for all the articles being published in CBU Journal of Science.

Instructions for Authors and Article Template can be found on the main page of MCBU Institute of Natural and Applied Sciences (<http://fbe.cbu.edu.tr>)





Vol: 19, Issue: 2, Year: 2023

Contents

Research Article

Pages

Influence of Edible Coating and Process Conditions on The Osmotic Dehydration of Carrot Slices

DOI: 10.18466/cbayarfbe.1257257

Osman Yağız Turan, Ebru Fıratlıgil

107-112

Investigation of the Viability of Different Cancer Cells on Decellularized Adipose Tissue

DOI: 10.18466/cbayarfbe.1212604

Esin Akbay Çetin

113-119

Epigenetic Alterations in Mouse Muscle Cells After In Vitro Treatments with COVID-19 and Influenza Vaccines

DOI: 10.18466/cbayarfbe.1245847

Selcen Çelik Uzuner

121-130

Study of *Anemone coronaria* L. (Manisa Tulip) Species, Symbol Plant of Manisa Province, for Biomonitor and Phytoremediation Purposes

DOI: 10.18466/cbayarfbe.1193450

Feyza Candan

131-136

Boric Acid Treatment Strengthens the Cytotoxic Effect of Sorafenib on Triple Negative Breast Cancer Cell Lines

DOI: 10.18466/cbayarfbe.1201068

Erkan Kahraman, Erdem Göker

137-141

Radiological Properties of Some Chemotherapy Drugs for Electron, Proton and Carbon Ion Interactions in the Energy Region 10 keV – 400 MeV

DOI: 10.18466/cbayarfbe.1140327

Mehmet Büyükyıldız, Murat Türemiş

143-149

On the Continuity Properties of the Set of Trajectories of the Control System with Limited Control Resources

DOI: 10.18466/cbayarfbe.1198603

Anar Huseyin

151-157

An Occupational Safety Fuzzy Risk Analysis: An Application in a Building Construction Sites

DOI: 10.18466/cbayarfbe.1213357

Orhan Engin, Raife Canlar Durmaz

159-165

Noise-Robust Spoofed Speech Detection Using Discriminative Autoencoder

DOI: 10.18466/cbayarfbe.1132319

Gökay Dişken, Zekeriya Tüfekçi

167-174



- Evaluation of the Relationship of Surface Roughness with Machining Parameters in Milling of AA 7075 Material with Experimental and Deform 3D Simulation 175-182
DOI: 10.18466/cbayarfbe.1231009
Ömer Erkan
- Investigation of Different Oriented 2D Straight Breakwater Under Dynamic Conditions 183-188
DOI: 10.18466/cbayarfbe.1229763
Mustafa Murat Yavuz, Pınar Sarı Çavdar
- Influence of Nanofibrillated Cellulose on Mechanical and Thermal Properties of Polyester Composites 189-195
DOI: 10.18466/cbayarfbe.1089023
Bayram Poyraz, Şevki Eren, Serkan Subaşı, Ayhan Tozluoğlu

Influence of Edible Coating and Process Conditions on The Osmotic Dehydration of Carrot Slices

Osman Yağız Turan¹ , Ebru Fıratlıgil^{1*} 

İstanbul Technical University, Department of Food Engineering, Maslak, İstanbul, Türkiye

*ebruf@itu.edu.tr

*Orcid No: 0000-0002-9637-3770

Received: 28 February 2023

Accepted: 15 June 2023

DOI: 10.18466/cbayarfbe.1257257

Abstract

Optimization of process parameters in osmotic dehydration is critical to achieve desired levels of water removal and solid uptake. To minimize the solid gain, food materials are coated with edible films prior to drying. In this study, the effects of solution temperature (25°C, 35°C and 45°C), sugar solution concentration (40%, 50% and 60%) and edible film coatings on solid gain (SG) and water loss (WL) of osmotically dehydrated carrot slices were investigated. Solid gain and water loss rates after osmotic dehydration were determined and dehydration efficiency index values were calculated. It is observed that WL and SG values increase with the increasing temperature and solution concentration. The solid permeability of cornstarch coating was lower compared to plum coated and non-coated samples. Weight loss of dehydrated carrot slices coated with cornstarch were higher than the non-coated ones. Cornstarch based edible coatings did not have a negative effect on water loss while plum based edible coatings caused the water loss to decrease. Optimum mass transfer rates for water and solids were achieved at 25°C with a solution concentration of 60%. Highest dehydration efficiencies recorded were of starch-coated samples at all process parameters. Plum coating showed a slight improvement against non-coated samples at optimum process parameters.

Keywords: Dehydration efficiency, edible coating, osmotic dehydration, solid gain, water loss

1. Introduction

Drying is an ancient and basic operation used to preserve food materials for further consumption and to enhance food safety. In conventional drying process, food material is subjected to extensive heat energy and as a result sensorial, physical, and nutritional properties of the food material are affected adversely [1]. Non-thermal novel processes are being developed and optimized to overcome this obstacle. Osmotic dehydration, one of the non-thermal water removal processes, can be defined as partially removal of water by immersion of the food material into a hypertonic solution. Water is removed from the product without changing its phase up to a level of 50% and a minimally processed food material is obtained. Due to non-thermal characteristics of osmotic drying, nutritional and sensory losses can be kept at minimum while deterioration reactions such as browning or oxidation are inhibited [2-4].

During osmotic dehydration, a pressure gradient is formed in solution medium across the cell surface, thus water molecules move through surface of food material

to the solution and simultaneously solutes are transferred into the tissue [5]. Materials used to formulate the osmotic solution can be selected from a wide range of options such as sugars like glucose, sucrose and fructose or salts or a combination of these. Type of the food material to be dried is critical in the selection of osmotic solution due to the potential sensorial effect of the solute uptake. Therefore, the prominent considerations in osmotic dehydration are the type and extent of solute as this selection directly affects both the properties of food material and the rate of operation [6,7].

During the osmotic dehydration, water loss of the food material is the main interest of the operation; besides this preferred case, solute uptake is the undesirable side effect due to mainly sensorial changes and also the formation of a surface barrier by solids which reduces the water loss [8,9]. Thus, it is critical to inhibit excessive solid uptake without creating a negative effect on the rate of water loss. Adjustment of the process parameters such as temperature and duration is essential but not sufficient to lower the solid uptake to a desired level. Using edible coatings to lower solute uptake without blocking water

loss of the food material can be considered as an efficient improvement in the process [10]. Edible coatings are developed with the use of bio-based polymers such as starches, proteins, lipids, gums or cellulose derivatives that are made from various agricultural commodities. Edibility, biocompatibility and barrier properties are the main features of edible coatings [11,12]. Use of edible coatings offers the potential to reduce the unfavorable effects of osmotic dehydration [13,14].

The objective of this study was to investigate the effects of starch and plum based edible coatings on osmotic dehydration of carrots (*Daucus carota* L. ssp. *sativus*) and to examine the effects of process parameters such as temperature and solution concentration on the dehydration kinetics.

2. Materials and Methods

2.1. Materials

Carrot (*Daucus carota* L. ssp. *sativus*) samples were osmotically dehydrated in this work. Samples were purchased daily from a local market in Istanbul. Samples were selected to ensure minimal variation and refrigerated at 4 °C until experiments. Edible films used in the study were prepared with cornstarch (commercial) and damson plum (*Prunus domestica* subsp. *insititia*). Sucrose (commercial sugar) was used as the osmotic agent.

2.2. Materials preparation

Carrot samples were cut into slices with a thickness of 0.5±0.1 cm and a diameter of 2.0±0.1 cm after peeling. Sucrose solutions (300 g. each) with the concentrations of 40%, 50% and 60% w/w were prepared in 600 ml beakers with deionized water. Product/solution ratio was adjusted to 1:10 (weight basis) to avoid any dilution in osmotic media.

2.3. Coating treatments

Cornstarch solution (3% w/w) was prepared by heating and stirring the water/starch mix at 80°C and 90 °C, for 15 minutes at each temperature. Solution was cooled to room temperature and carrot samples were immersed in solution for 3 minutes. Coating was fixed on samples by heating at 70°C for 25 minutes in a convection oven. Plum coating solution was prepared by mashing the peeled fruit and diluting to 10° Brix with deionized water. Carrots were immersed in solution for 3 minutes and the coating fixed by heating at 70°C for 60 minutes.

2.4. Osmotic dehydration treatment

Coated and non-coated carrot samples submerged in osmotic solutions and kept in contact with the solution during the dehydration period by using a form of plastic cage. Processes carried out for 210 minutes (3.5 h) at

three levels of temperatures. Solution-sample containing beakers placed in incubators during dehydration process at 25, 35 and 45 °C to ensure uniform temperature distribution in experimental units. Immediately after osmotic process, carrot samples were removed from solution and blotted with adhesive paper to remove residual sugar solution. Samples weighed and moisture contents were calculated. A portion of the osmotically dehydrated and non-treated carrot samples were oven-dried by the standard method to calculate the initial and final dry matter [15].

Weight reduction (WR), water loss (WL) and solid gain (SG) data were calculated to indicate overall mass exchange between sample and solution. Dehydration efficiency index (WL/SG ratio) was also used to indicate the efficiency of process. The mass amount of solids leaching from the product (sugars, acids, vitamins and minerals) assumed to be negligible [16]. Following equations were used to calculate mass balances during osmotic dehydration [17,18]. Weight reduction is the overall weight loss during the operation, solid gain is the amount of solutes transferred to samples and water loss is the total amount of water removed from samples with respect to initial weight of the sample.

$$WR = \frac{w_i - w_f}{w_i} \times 100 \quad (1.1)$$

$$SG = \frac{w_{sf} - w_{si}}{w_i} \times 100 \quad (1.2)$$

$$WL = \frac{w_i w_{wi} - w_f w_{wf}}{w_i} \times 100 \quad (1.3)$$

Where w_i is initial weight of the sample, w_f is the weight of the sample after osmotic dehydration. w_{sf} and w_{si} are the initial and final dry matter content of samples and w_{wi} and w_{wf} are the initial and final amount of water in samples.

2.5. Statistical analysis

Experiments were conducted in triplicates for each level of parameters and variations among the replicates were given as error bars. Statistical analyzes were carried out using *MINITAB 17* software. Variations among the means of treatments were calculated to perform analysis of variance, and the means were compared according to Tukey and Fisher's tests to determine significant differences.

3. Results and discussion

Rates of water loss and solid gain are the main responses of an osmotic dehydration process. Therefore, the remarks on these values explain the influence of different factors applied in the process. The extent of water loss and solid gain were calculated and shown in Tables 1 and 2, respectively. Levels of each factor (temperature, concentration and coating treatment) were given as they have substantial impact on mass exchange values.

Table 1. Effects of temperature, concentration and coating treatment on the water loss of carrot during osmotic dehydration.

Temp. (°C)	Conc. (%)	Non-coated	Starch Coated	Plum Coated
25	40	45.09 ± 1.18 ^A	45.00 ± 1.03 ^A	37.79 ± 0.49 ^B
	50	55.41 ± 0.52 ^A	55.59 ± 0.68 ^A	51.10 ± 0.27 ^B
	60	60.01 ± 1.06 ^B	65.17 ± 0.01 ^A	61.28 ± 0.35 ^B
35	40	49.09 ± 0.03 ^A	49.60 ± 0.58 ^A	36.70 ± 0.33 ^B
	50	57.66 ± 0.47 ^B	61.83 ± 1.05 ^A	51.56 ± 1.36 ^C
	60	65.63 ± 0.64 ^B	68.15 ± 0.13 ^A	59.02 ± 0.78 ^C
45	40	51.60 ± 1.60 ^A	51.85 ± 1.05 ^A	39.93 ± 0.37 ^B
	50	62.49 ± 0.96 ^A	61.34 ± 0.81 ^A	54.48 ± 0.12 ^B
	60	69.80 ± 0.92 ^A	68.88 ± 0.49 ^A	63.85 ± 0.27 ^B

*Results are expressed as the Means ± Standard Deviation for triplicates

**Means that do not share a capital letter in the same line are significantly different at $p \leq 0.05$ according to Tukey and Fisher tests.

Table 2. Effects of temperature, concentration and coating treatment on the solid gain of carrot during osmotic dehydration.

Temp. (°C)	Conc. (%)	Non-coated	Starch Coated	Plum Coated
25	40	6.09 ± 0.29 ^A	5.32 ± 0.30 ^A	5.65 ± 0.92 ^A
	50	7.29 ± 0.48 ^A	6.15 ± 0.03 ^B	6.60 ± 0.65 ^B
	60	7.57 ± 0.54 ^A	6.47 ± 0.28 ^B	7.15 ± 0.02 ^{AB}
35	40	7.80 ± 0.26 ^A	6.42 ± 0.21 ^B	6.63 ± 0.27 ^B
	50	8.72 ± 0.57 ^A	6.61 ± 0.08 ^B	6.94 ± 0.09 ^B
	60	8.77 ± 0.49 ^A	6.89 ± 0.05 ^B	7.18 ± 0.21 ^B
45	40	8.15 ± 0.82 ^A	6.48 ± 0.61 ^B	8.20 ± 0.47 ^A
	50	8.74 ± 0.40 ^A	7.11 ± 0.33 ^B	8.73 ± 0.23 ^A
	60	8.89 ± 0.42 ^A	7.30 ± 0.42 ^B	8.78 ± 0.42 ^A

*Results are expressed as the Means ± Standard Deviation for triplicates

**Means that do not share a capital letter in the same line are significantly different at $p \leq 0.05$ according to Tukey and Fisher tests.

3.1. Effects of process temperature

Increase in the process temperature results in increased values of water loss and solid gain for each type of coating. Although the increase caused by temperature rise in water loss is significant, increase in the solid gain seemed to be more effective, especially from 25 to 35°C for non-coated and starch coated samples. The effect of temperature increase from 25 to 35°C was relatively poor on plum coated samples regarding both water loss and solid gain. Diffusion is a temperature dependent process, thus the increase in water loss from the product and the diffusion of osmotic agent into the product would be enhanced by the increase in the temperature due to lower viscosity of the medium and swelling of cell membranes [19]. Increase of water loss for starch-coated samples was around 10%, which was relatively higher than plum coated or non-coated samples regarding the temperature

increase from 25 to 35°C. Solid gain, on the other hand, seemed to increase in a higher manner from 25 to 35°C. The rate of this increase was very high at lower concentrations, which were 28% for non-coated, 21% for starch coated and 17% for plum coated samples at 40% sugar concentration. Another apparent change in solid gain with temperature was recorded for plum coated samples, the rises were around 23% when the temperature increased from 35 to 45°C for all concentrations. As a general perspective of osmotic dehydration, mass transfer rates increase with temperature, but over 45°C browning and flavor change takes place and over 60 °C tissue characteristic alter remarkably resulting the solids to impregnate into the intercellular spaces of the food material. Thus, the optimum process temperature depends on the food material [20]. In the case of green beans, for instance, 20°C is considered preferable compared to 40 °C [21].

3.2. Effects of solution concentration

The increase in sugar concentration results in increased percentage of water loss for all types of coatings at all temperatures. As seen in Table 1, increasing the concentration from 40 to 50% results in a high increase in water loss. This value was approximately 20% for non-coated and starch coated samples. For plum coated samples, increase in water loss boosts up to 40%. Besides, when the concentration increased to a level of 60%, the rise in water loss is roughly half the previous value. This is most likely because the concentration gradient between the food material and hypertonic solution reaches to a maximum and the further increase in concentration would have relatively lower effect on mass transfer. Similar trend was observed for solid gain, which can be seen in Table 2. Increase in solid gain was observed to be between 4-19% for different temperatures and types of coatings when the concentration was increased to 50%. A lower rise was seen when the concentration was increased to 60%, between approximately 1% and 8%. Increased concentrations apparently increase the sugar uptake and promotes the formation of a solid layer across the food product-osmotic medium interface, which decelerates the mass transfer, for both solids and water. Suppression of solid uptake seems to be more intense regarding the molecular size difference between sugar and water. Increase in water loss and solid gain by the change in solution concentration also determined in various other studies. Calculation of modelling parameters showed an increase in mass transfer rates for the osmotic dehydration of cherry tomato [16] and apple [22] at higher concentrations, which is referred to the cellular response of the food material to the osmotic pressure increment.

3.3. Effects of edible coatings

Edible coatings have a significant effect on the mass transfer during osmotic dehydration of food materials. Reducing the solid uptake is the main interest of coating samples but the reduction of water loss is the negative response of the process. Experimental results show that edible coatings substantially reduce solid uptake during the dehydration process. It can be seen in Table 2, that percentage of solid gain was lower for coated samples than non-coated samples at all parameters except 45 °C. Non-coated and plum coated samples seem to have similar rates of solid gain at 45 °C, which were higher than starch coated samples. Concurrently, edible coatings have a considerable effect on water loss, which can be a critical limitation. There seemed to be no significant difference between non-coated and starch coated samples for most of the cases. For sugar concentration of 60%, starch coated samples showed a higher water loss than non-coated samples at 25 and 35 °C. Similar effects of edible coatings on water loss and solid gain were reported by various authors. Garcia et. al. [23] showed that papaya samples with chitosan based coatings have lower solid

gain and higher water loss values, because of the blockage of solute penetration by the solids accumulated on the surface of the coating. Also, Jalaei et. al. [17] stated that carboxyl-methyl cellulose, low-methoxyl pectinate and corn starch coatings on apple samples had a beneficial effect on reducing solid gain without having much impact on water removal. On the other hand, plum coated samples showed a relatively lower water loss rates. This may be a result of redundant heat used for fixation of coating onto samples. Coating solution had a low viscosity and a high water content as described previously in section 2.3, this resulted in the need for a longer period of surface drying to avoid leakage of coating. The fixation period of the coating caused a mild initial surface dehydration, thus affecting the rate of water loss adversely. Consequently, percentage of water loss values of plum coated samples were slightly lower than non-coated and starch coated samples.

3.4. Dehydration efficiency index

Dehydration efficiency index is the term used to express the extent of solid gain relatively to water loss of the sample. High ratio of water loss to solid gain (WL/SG) means the process is focused on dehydration with minimal solid uptake, while low ratios mean the process targeted to extensive solid gain for operations like salting or candying [24,25]. The WL/SG ratio can accurately reveal the influence of process conditions and coating treatments. In the case of osmotic dehydration of fruits and vegetables, it is mostly aimed to achieve high levels of water loss and minimal solute uptake. Therefore, high DEI values are preferred. DEI values observed in this work are given in Figure 1 to illustrate the effects of temperature and solution concentration regarding to different coating treatments.

Coated and non-coated samples shows similar behavior against changes in process parameters. Highest values of DEI were observed at lowest temperatures (25°C) for each coating and each concentration. In addition, it can be seen in Fig. 1 that the solution concentration has a favorable effect at each process parameter; highest sugar concentration treatment in this study (60%) has the highest proportional difference between water loss and solid gain values. Correspondingly, Lazarides et. al. [26] stated that the largest difference between moisture diffusivity and soluble solids diffusivity for the osmotic dehydration of Granny Smith apples and white potatoes was observed at the lowest process temperature (20 °C) with the highest solution concentration (65%). It is also shown in a study conducted on a model food (agar gel) that the gap between water loss and solid gain values expands in a positive manner with increasing concentration, thus a dewatering situation occurs rather than a candying situation [27]. Effects of edible coatings on mass transfer kinetics of carrot samples can be clearly seen by the use of DEI data. As previously stated, effects of coatings individually on water and solids transfer were

dissimilar, thus the dehydration efficiency index shows a more prominent outcome as it is the ratio of these mass transfer variables. Starch coated samples seem to have the highest value of DEI as seen in Fig. 1. Min. and max. DEI values for starch were 7.73 and 10.07, which

observed at 35 °C with 40% concentration and at 25 °C with 60% concentration, respectively. To highlight the difference between the coating treatments, WL/SG values at the optimum process temperature (25 °C) were given in Figure 2.

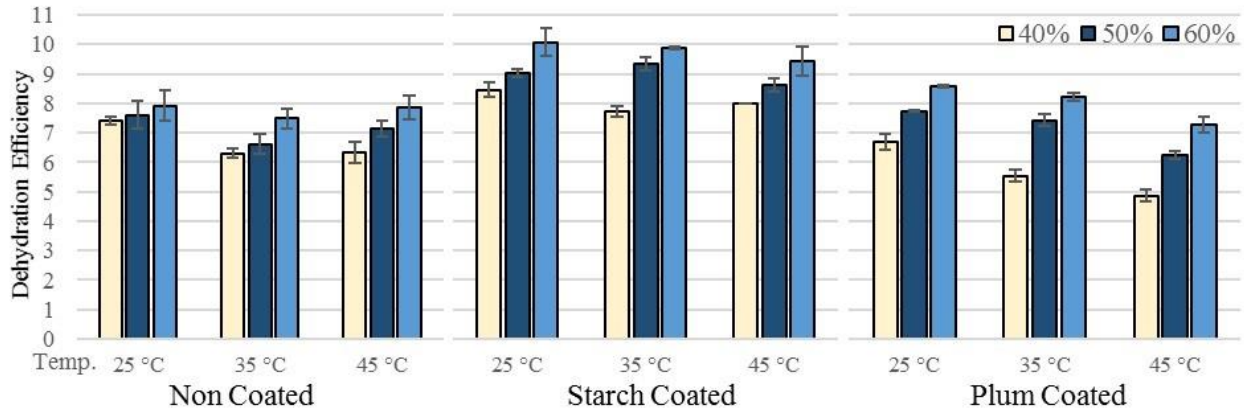


Figure 1. Effect of process conditions on dehydration efficiency index of non-coated, starch coated and plum coated samples.

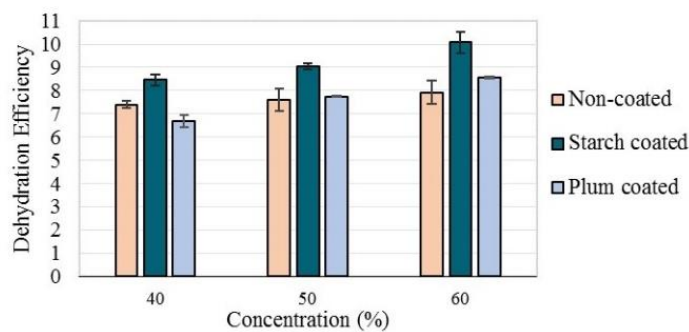


Figure 2. Effect of coating treatments on dehydration efficiency index of carrot samples at 25°C.

Increase in concentration does not seem to have a significant effect on non-coated samples, regarding the DEI at 25 °C. On the other hand, plum coated samples give better values when the concentration increased to the optimum level (60%), increasing from 6.69 to 8.57, while non-coated samples remain at 8.09. These outcomes suggest that it would be suitable to use plum coating at higher osmotic pressures to achieve a practical dehydration efficiency.

4. Conclusion

Increase in studied process parameters, temperature and solution concentration lead to a significant increase in water and solids diffusivity. However, temperature had an inverse effect on dehydration efficiency regarding the increase in solid gain of sample thus causing the lowest temperature (25 °C) to be the most efficient. Besides,

highest water loss/solid gain ratio was obtained at the highest solution concentration (60%). Selecting the adequate solution concentration ensures the aimed increase in water loss without an excessive rise in solute uptake. It is also found that, use of edible coatings can significantly inhibit solute uptake during osmotic dehydration without critically affecting the water loss of samples. In this study, cornstarch coated samples showed an excellent behavior in terms of solid and water diffusion. Solid gain values of coated samples dropped significantly without having any impact on water loss in comparison with non-coated samples. On the other hand, application of plum coating seemed to have affected water loss adversely while inhibiting solute uptake. Considering the optimum process parameters, plum coating showed a slight improvement against non-coated samples. Nevertheless, starch coating offers better values of water loss and solid gain compared to plum coating.

Acknowledgement

This research did not receive any specific grant from funding agencies in the public, commercial, or not-for-profit sectors.

Author's Contributions

Osman Yağız Turan: Drafted and wrote the manuscript, performed the experiment and result analysis.

Ebru Firatgil: Assisted in analytical analysis on the structure, supervised the experiment's progress, result interpretation and helped in manuscript preparation.


Ethics

There are no ethical issues after the publication of this manuscript.

References

- [1]. Kowalski, S.J., Szadzińska, J., Lechtańska, J., 2013. Non-stationary drying of carrot: Effect on product quality. *Journal of Food Engineering*, 118(4): 393-399.
- [2]. Silva, K.S., Fernandes, M.A., Mauro, M.A., 2014. Effect of calcium on the osmotic dehydration kinetics and quality of pineapple. *Journal of Food Engineering*, 134: 37-44.
- [3]. Liu, B. and Peng, B.Z., 2017. Modelling and optimization of process parameters for strawberry osmotic dehydration using central composite rotatable design. *Journal of Food Quality*, 2017.
- [4]. Muhamad, N. and Basri, M.S.N., 2019. Effect of osmotic dehydration on physicochemical characteristics of dried Manis Terengganu melon. *Bioscience Research*, 16(1): 182-191.
- [5]. Nowacka, M., Tylewicz, U., Laghi, L., Dalla Rosa, M., Witrowa-Rajchert, D., 2014. Effect of ultrasound treatment on the water state in kiwifruit during osmotic dehydration. *Food Chemistry* 144, 18-25.
- [6]. Ganjloo, A. and Bimakr, M. 2015. Influence of sucrose solution concentration and temperature on mass exchange during osmotic dehydration of eggplant (*Solanum melongena* L.) cubes. *International Food Research Journal*, 22(2): 807-811.
- [7]. Derossi, A., Severini, C., Del Mastro, A., De Pilli, T. 2015. Study and optimization of osmotic dehydration of cherry tomatoes in complex solution by response surface methodology and desirability approach. *LWT-Food Science and Technology*, 60(2): 641-648.
- [8]. Mitrakas, G.E., Koutsoumanis, K.P., Lazarides, H.N., 2008. Impact of edible coating with or without anti-microbial agent on microbial growth during osmotic dehydration and refrigerated storage of a model plant material. *Innovative Food Science and Emerging Technologies*, 9(4): 550-555.
- [9]. Lazarides, H.N., Mitrakas, G.E., Matsos, K.I., 2007. Edible coating and counter-current product/solution contacting: A novel approach to monitoring solids uptake during osmotic dehydration of a model food system. *Journal of Food Engineering*, 82(2): 171-177.
- [10]. Matuska, M., Lenart, A., Lazarides, H.N., 2006. On the use of edible coatings to monitor osmotic dehydration kinetics for minimal solids uptake. *Journal of Food Engineering* 72, 85-91.
- [11]. Sanchez-Ortega, I., Garcia-Almendarez, B.E., Santos-Lopez, E.M., Reyes-Gonzalez, L.R., Regalado, C., 2016. Characterization and antimicrobial effect of starch-based edible coating suspensions. *Food Hydrocoll.*, 52, 906-913.
- [12]. Elsabee, M.Z., Abdou, E.S., 2013. Chitosan based edible films and coatings: A review. *Materials Science and Engineering C*, 33, 1819-1841.
- [13]. Taghizadeh, M., Fathi, M., Sajjadi, A.L., 2016. Effect of coating concentration and combined osmotic and hot-air dehydration on some physicochemical, textural, and sensory properties of apple slabs. *Acta Alimentaria*, 45(1): 119-128.
- [14]. Rodriguez, A., Soteras, M., Campanone, L. 2021. Review: Effect of the combined application of edible coatings and osmotic dehydration on the performance of the process and the quality of pear cubes. *International Journal of Food Science and Tech.*, 56(12): 6474-6483.
- [15]. AOAC, 2002. Official Methods of Analysis, Vol. 2, No. 934.06. Assoc. Off. Anal. Chem. Rockville, MD, USA.
- [16]. Azoubel, P.M., Murr, F.E.X., 2004. Mass transfer kinetics of osmotic dehydration of cherry tomato. *Journal of Food Engineering*, 61, 291-295.
- [17]. Jalae, F., Fazeli, A., Fatemian, H., Tavakolipour, H., 2011. Mass transfer coefficient and the characteristics of coated apples in osmotic dehydrating. *Food and Bioproducts Processing*, 89, 367-374.
- [18]. Jain, S.K., Verma, R.C., Murdia, L.K., Jain, H.K., Sharma, G.P., 2011. Optimization of process parameters for osmotic dehydration of papaya cubes. *Journal of Food Science and Technology*, 48, 211-217.
- [19]. Lazarides, H.N., Katsanidis, E., Nickolaidis, A., 1995. Mass transfer kinetics during osmotic pre-concentration aiming at minimal solid uptake. *Journal of Food Engineering*, 25: 151-166.
- [20]. Torreggiani, D., 1993. Osmotic dehydration in fruit and vegetable processing. *Food Research International*, 26: 59-68.
- [21]. Biswal, R.N., Bozorgmehr, K., Tompkins, F.D., Liu, X., 1991. Osmotic concentration of green beans prior to freezing. *Journal of Food Science*, 56, 1008-1012.
- [22]. Sacchetti, G., Gianotti, A., Dalla Rosa, M., 2001. Sucrose-salt combined effects on mass transfer kinetics and product acceptability. Study on apple osmotic treatments. *Journal of Food Engineering*, 49, 163-173.
- [23]. Garcia, M., Diaz, R., Martinez, Y., Casariego, A., 2010. Effects of chitosan coating on mass transfer during osmotic dehydration of papaya. *Food Research International*, 43, 1656-1660.
- [24]. Lazarides, H.N., 2001. Reasons and Possibilities to Control Solids Uptake during Osmotic Treatment of Fruits and Vegetables, in: Pedro, F., Amparo, C., Jose Manuel, B., Walter E. L., S., Diana, B. (Eds.), *Osmotic Dehydration and Vacuum Impregnation: Applications in Food Industries*. Technomic Publishing Co. Inc.
- [25]. Jokic, A., Zavargo, Z., Gyura, J., Prodanic, B., 2008. Possibilities to control solid uptake during osmotic dehydration of sugar beet, in: Cantor, J.M. (Ed.), *Progress in Food Engineering Research and Development*. Nova Publishers, pp. 243-261.
- [26]. Lazarides, H.N., Gekas, V., Mavroudis, N., 1997. Apparent mass diffusivities in fruit and vegetable tissues undergoing osmotic processing. *Journal of Food Engineering* 31, 315-324.
- [27]. Raoult-Wack, A.L., 1994. Recent advances in the osmotic dehydration of foods. *Trends in Food Science and Technology* 5, 255-260.

Investigation of the Viability of Different Cancer Cells on Decellularized Adipose Tissue

Esin Akbay Çetin^{1*} 

¹Department of Biology, Faculty of Science, Hacettepe University, 06800, Ankara, Türkiye

*akbayesin@gmail.com

*Orcid No: 0000-0002-0797-8322

Received: 30 November 2022

Accepted: 15 June 2023

DOI: 10.18466/cbayarfbe.1212604

Abstract

Cancer is one of the most severe diseases diagnosed in millions of people worldwide each year. Despite many studies, there is insufficient information on how tumor formation prevents cancer treatment development. Although clinical trials are the most effective way to examine tumor formation and test anti-tumor drugs, ethical and safety limitations prevent this method from being widely used. This study aims to test the cellular behavior of different cancer cell lines on the platform obtained from decellularized adipose tissue *in vitro*. Detergent-based decellularization protocol applied to adipose tissue and cancer cell lines were seeded on obtained extracellular matrixes. Cell viability and apoptosis were observed by 3-(4,5-dimethylthiazol-2-yl)-2,5-diphenyltetrazolium bromide (MTT) assay and Acridine orange/Propidium iodide double staining, respectively. Also, cell-cell and cell-matrix interactions were investigated via pan-cadherin immunostaining. All cancer cell lines were also seeded in a cell culture dish to compare three-dimensional culture results with two-dimensional culture. As a result, the decellularization protocol allowed the original structure of the tissue scaffold to be preserved. According to cell viability analysis and immunocytochemical staining results, glioblastoma cell line (T98G) and human hepatoma cell line (Hep3B) were observed to have higher adhesion and viability potential than colon adenocarcinoma cell line (WiDr) on the tissue matrix obtained. With this study, it can be said that different cancer cells have different behaviors on decellularized matrixes. Finally, developing *in vitro* models as a more economical, scalable, and reproducible way to test drugs and therapeutics is crucial for successful clinical translation.

Keywords: Adipose tissue, Cancer cell lines, Decellularization, Extracellular matrix, Three-dimensional culture model

1. Introduction

In recent years, it has been known that cancer is one of the leading causes of death, especially in developed countries. Significant efforts have been made to overcome this disease, which has not yet had a definitive cure [1]. These efforts focused mainly on unlimited replication, causes of cell migration, genetic mutations, and intracellular signaling [2]. Cancer has recently begun to be considered a tissue to understand its general mechanism better. For this reason, the focus was on the extracellular matrix (ECM), critical in regulating cell behavior in cancer tissues and all tissues [3, 4].

Scientists rely on various scientific tools to test promising therapeutics and understand the biology underlying health and disease. One of the most widely used models is *in vivo* animal models.

While extensive animal experiments were the best approach until recently, different models have been preferred for ethical and scientific reasons [4]. Today, many three-dimensional *in vitro* cancer models are trying to be developed as a more straightforward alternative to animal models. Ideal for the three-dimensional model is to expect the three-dimensional structure of the tumor, especially the presence of cell-cell and cell-matrix interactions [5].

Recent studies in the extraction and purification of decellularized ECM from healthy tissues show that ECMs can be used for physio mimetic 3D *in vitro* tumor models in terms of their basic biomolecular properties and dynamic cancer cell-ECM interactions [6]. ECM is an important structure consisting of various protein and carbohydrate types, providing tissue-specific cellular functions and specific features for each tissue and organ type.

Functional ECMs are preferred in tissue engineering because they are a platform that will support cells and have a structure that will support the adhesion, migration, proliferation, and differentiation of cells to this platform. The difficulty of synthetic scaffolds in mimicking *in vivo* ECM structures has led to the widespread use of naturally derived ECMs. While natural ECMs are used in tissue engineering applications, they must first be cleansed from all cells (by decellularization) [7]. It has been also reported that the composition and architecture of the ECM may vary according to the tumor type and stage of progression [6, 8]. The resulting ECMs have a dynamic structure. It is important to note that ECMs serve many functions, including scaffolding, storing growth factors that are pro- and anti-tumor, and regulating differentiation, immune stimulation, and tumor migration [9-11].

Decellularization methods include physical, chemical, enzymatic, or combined use. Which method will be used is chosen by the characteristics of the target tissue/organ. All these methods have advantages and limitations, but the common use is to cleanse the tissue from all its cells entirely and to have the least component loss and damage to the ECM during this process [5]. The standardized adipose tissue decellularization method we reported was preferred in this study as it is reliable [12].

This study obtained natural scaffolds by decellularizing rat adipose tissue to mimic the *in vivo* microenvironment. It is aimed to study and compare the proliferation and adhesion profiles of different cancer cells (T98G, WiDr, and Hep3B) on this natural scaffold.

2. Materials and Methods

2.1. Obtaining Adipose Tissue

Within the scope of the study, 5 *Wistar albino* rats (300-350 gr) were used with the approval of the Hacettepe University Animal Care and Use Committee (Permit no. 2012/52). The rats were humanely killed after intraperitoneal injection with an overdose of anesthesia (10% ketamine - 2% xylazine). Subcutaneous adipose tissues isolated under sterile conditions were washed twice with sterile phosphate buffer solution (PBS) before being cut into 5 cm x 5 cm pieces. Upon the collection of adipose tissue pieces, PBS containing 1% penicillin-streptomycin (P/S) was used as a solution to preserve the tissues until the pieces were decellularized at +4 °C.

2.2. Decellularization Method

Rat subcutaneous adipose tissues, which were decellularized using the standardized decellularization method in our previous studies, were cut into pieces after they were obtained and stored under appropriate conditions until the experiments were started [12-14].

Briefly, samples were treated in 0.5% sodium dodecyl sulfate (SDS) solution for two days.

Following this application, it was exposed to 1% SDS solution for 24 hours, and in the last step, 1% TritonX-100 solution was used for one hour. Between each step, samples were washed with PBS. The decellularized samples were washed twice with PBS and stored in PBS containing 1% P/S at +4 °C until lyophilization. Non-decellularized adipose tissue samples were used as a control group.

2.3. Histological Staining

Histological analyzes were performed to observe the effectiveness of decellularization. Hematoxylin, Eosin (H&E), and Masson Trichrome (MT) staining methods were used. Briefly, 10% formalin was used for fixation. Both decellularized control and decellularized tissue matrices were fixed. The fixed samples were passed through the alcohol batch, embedded in paraffin blocks, and cut into 5 µm slices with a microtome. Sections were stained with both stains according to the protocols and observed under a light microscope (Leica DM100, Germany).

2.4. Lyophilization and Sterilization Methods

Before lyophilization, all samples obtained were stored at -80 °C overnight. For the lyophilization process, the samples were dried in a freeze dryer (Chris Alpha1-2 LD plus, M Christ GmbH, Germany) for 24 h. The lyophilized samples were stored at -20 °C until the stage in which the cells were seeded.

For sterilization, the lyophilized decellularized matrix was transferred to 24-well plates. All matrix surfaces were exposed to ultraviolet (UV) irradiation for 45 minutes. At the same time, parafilm, used to prevent the cells from adhering to the surface of the wells, was soaked in 70% ethanol before they were placed in the wells. Plates, the surfaces of which were coated with parafilm, were sterilized with 70% ethanol and finally exposed to UV irradiation for 20 minutes [15].

2.5. Culture of Cancer Cell Lines

The cancer cell lines that are tried to be modeled *in vitro* within the scope of this study are human brain cancer (T98G, CRL-1690™), human hepatoma (Hep3B, HB-8064™), and human colon carcinoma cell lines (WiDr, CCL-218™). All cell lines were purchased from the American Type Culture Collection (ATCC), Rockville, MD, USA. T98G and Hep3B cell lines were cultured in 75 cm² culture flasks (Corning, USA) using Dulbecco's modified Eagle's medium (DMEM) supplemented with 10% fetal bovine serum (FBS), 1% glutamine, 1% P/S while WiDr cell line was routinely cultured in high glucose DMEM supplemented with 10% FBS and 1% P/S. All cells were incubated at standard conditions of 37 °C, 95% relative humidity, and 5% CO₂.

2.6. Cell Seeding

To grow cells as two-dimensional, cells were cultured with their specific medium for each cancer cell type on culture flasks in a traditional incubator (5% CO₂, 95% humidity, 37 °C) [15]. For three-dimensional cell culture, it was determined as 2x10⁵ cells / 5 mm matrix for cell cultivation considering the literature [16, 17]. All cancer cells were trypsinized before cell seeding. Cells in a suspended state were prepared for cultivation with their specific medium. The matrices were placed in 24-well plates covered with parafilm, one for each well. A 20 µl of cell suspension was seeded onto each matrix and incubated in an incubator (37 °C / 5% CO₂) for 2 h. Finally, a 200 µl medium was added to each scaffold to maintain the density of 2x10⁵ cells/matrix inoculation [18, 19]. The matrices were stored in an incubator for 12 h before reaching the final volume of 500 µl in each well. Simultaneously decellularized control scaffolds were incubated in cell-free DMEM/F12. For equal cell seeding into each matrix, the cell suspension was gently pipetted before each use.

Acridine Orange and Propidium Iodide (AO/PI) double staining, immunocytochemical staining and MTT tests were performed at 24., 48., and 72. h following the cell cultivation. Separate matrices were used for all experiments with 3 replications.

2.7. AO/PI Staining

AO and PI double staining method was preferred to determine the apoptotic potential of cells on matrices. Briefly, the culture medium on the matrix was removed at 24, 48, and 72 h. Then, the matrices were transferred to a new 24-well plate. For the cells to absorb the dye well, the matrices were washed with PBS and stained for one minute with an AO/PI solution prepared at a ratio of 1: 1 (v: v). At the end of the staining protocol, the matrices were washed three times with PBS. Matrix images were examined using an inverted microscope (Olympus IX70 Inverted Microscope, Japan).

As in previous study [20], apoptotic cells were scored in photographs obtained by AO/PI staining, and apoptosis (early and late) inducing potential in cells of different groups was determined as a percentage.

2.8. Cell Viability Analysis

MTT analysis, widely used in the quantitative evaluation of cell viability, was preferred in this study [21]. Briefly, the culture medium was removed from wells at 24, 48, and 72 h. Then, the scaffolds were transferred to the new 24-well plate. For the 10% MTT solution to be used for analysis, 600 µl of DMEM was added to each well in which the matrices were previously placed. Then, 60 µl of MTT solution was carefully injected into the matrices and the plate was left in a gentle shaker for 10 minutes to activate the

solution in the wells. Afterwards, the plate was removed from the incubator for a 4-hour incubation. After incubation, the matrices were taken into a new 24-well plate, and isopropanol alcohol was added to each well. As a result of the interaction, the solutions obtained by carefully crushing and dissolving the formazan crystals in the matrices were taken into clean 96-well wells, and the absorbance was analyzed with a microplate reader (EZ Read 400; Microplate Reader, Biochrom) at wavelength 570 nm. As a control, the MTT method was applied to cell-free scaffolds, and these data were extracted from the values obtained from the cell included matrix.

2.9. Immunostaining

Adhesion molecules play a role in the orientation of cells to tissues, recognizing each other and regulating phenomena such as embryogenesis, cell growth, cell differentiation, and inflammation. By immunocytochemistry staining method, we investigated the presence of pan-cadherin, one of the adhesion molecules, mainly because of its roles in cell-cell and cell-matrix interactions. Briefly, seeded cells into decellularized scaffolds were washed with PBS twice, fixed with methanol for five minutes, and blocked-in blocking serum for 20 minutes. After washing with PBS, cells were incubated with primary antibody (1:100 dilutions, anti-pan cadherin antibody, ab16505, Abcam, UK) overnight. After this duration, cells were washed with PBS and incubated with secondary antibody (1:200 dilutions, goat anti-rat IgG H&L FITC, ab6840, Abcam, UK) for 45 minutes. At the end of this process, DAPI was used for the staining of nuclei, and cell-matrix complexes were examined under an inverted microscope (Olympus IX70 Inverted Microscope, Japan).

2.10. Statistical Analysis

In all experiments, data were represented as a mean ± standard deviation (SD). GraphPad Prism version 5.0 (GraphPad Software Inc., San Diego, CA, USA) was used for statistical analysis. Two-way analyses of variance were conducted to compare results. P values of 0.05 are considered statistically significant. At least three replications of each experiment were conducted.

Results

This study showed that a three-dimensional biomimetic decellularized adipose tissue matrix could be used to model different cancer types in vitro to mimic the cell-cell and cell-matrix interaction of the cancer microenvironment.

2.11. Decellularized Adipose Tissue

Adipose tissue is classified as loose connective tissue and consists of adipocytes. It also has a very thin extracellular matrix layer containing many vessels with

a fiber backbone such as collagen fibers. As a result of the decellularization process applied, a white, dry, and fibrous matrix was obtained from adipose tissue. After H&E staining, no nuclei were found in the matrixes obtained (**Figure 1**). It was also observed by MT staining that the tissue integrity was not impaired (**Figure 1**). Decellularization results showed that the detergent-based method used for the heart in our previous studies yields decellularized ECM scaffolds within the adipose tissue that retain properties similar to their natural structure [12, 13].

2.12. Cell Viability

To compare the viability profile of T98G, Hep3B, and WiDr cancer cells in two- and three-dimensional cultures, an MTT assay was performed on 24th, 48th, and 72nd h (**Figure 2**). The MTT results were examined for differences in cell viability potential between 2D and 3D

and whether there was a difference between different cancer cells in 3D. Cells in two-dimensional cultures exhibited a constant proliferation curve for three days, while each cell type in three-dimensional culture showed a different proliferation profile than in two-dimensional culture. Cancer lines were also found to have different proliferation potentials. In the T98G cell line, a significant increase in viability was observed in 3D compared to 2D at 24 hours (*: $p < 0.05$).

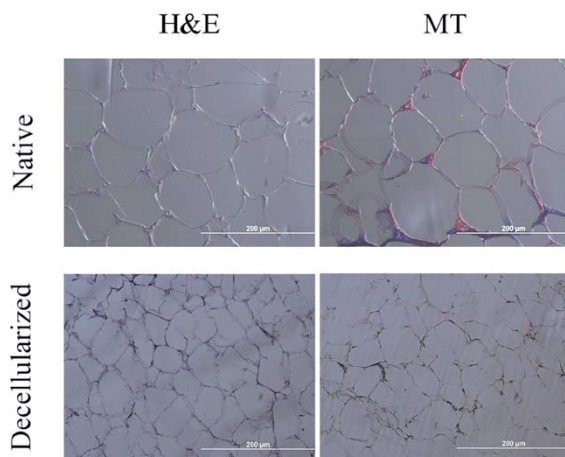


Figure 1. Histological staining of native and decellularized adipose tissue. H&E were used to detect either the presence of residual cells or cell fragments, and MT was used to show collagen content and organization. (H&E: Hematoxylin & Eosin, MT: Masson Trichrome, Scale bar = $\times 10$).

It was observed that the WiDr cell line was much lower in terms of cell viability in the three-dimensional environment than the results obtained in the two-dimensional environment. This difference was found to be significantly lower for all time periods (*: $p < 0.05$).

In Hep3B cell lines, while a decrease was observed in the viability rate in 3D compared to 2D at all hours, it was also determined that this decrease was not statistically significant. Comparing the viability of different cancer cell lines in 3D, it was observed that only T98G cells showed higher cell viability in the matrix at all periods compared to other cell lines (*: $p < 0.05$).

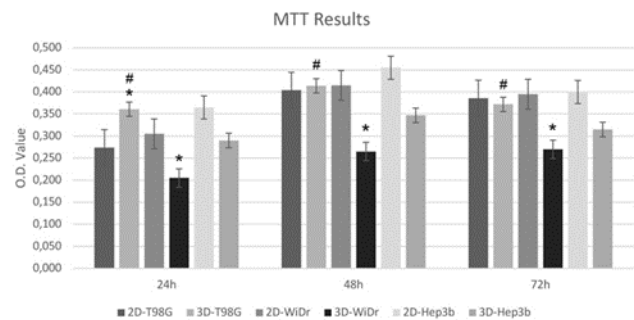


Figure 2. Cell growth potential comparison of the cancer cells in two- and three-dimensional culture. Cell proliferation was measured by MTT assays. Different cancer cells were statistically examined in terms of different time periods within and with each other. (n = 3; h: hours; *: $p < 0.05$, #: $p < 0.05$).

AO/PI staining images were also obtained to support the MTT results (**Figure 3**). Staining in the form of cell aggregates in the matrix was observed, especially in T98G and Hep3B cells at the 24th-hour staining. However, a significant decrease was observed in the number of cells in the matrix at 48th and 72nd h in WiDr cells as seen at Figure 3.

Calculation of the % apoptosis rate was based on the images obtained by AO/PI staining (**Figure 4**). Also, these results support the cell viability potential of results.

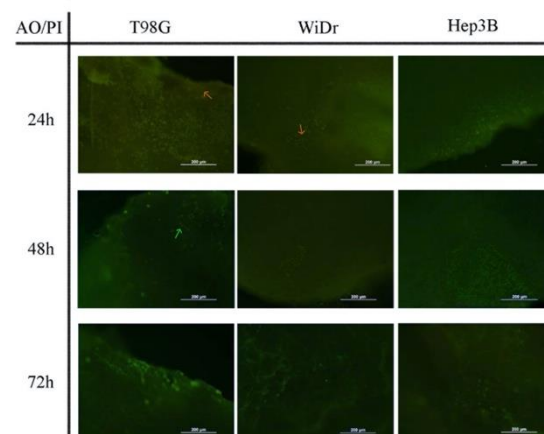


Figure 3. Image of cancer cells on the decellularized adipose matrix at different times. A double staining was performed with AO/PI on the cells. Orange arrows indicate late apoptosis and green arrow live cells. (Magnification: $\times 10$).

2.13. Immunostaining Results

The cell-matrix composition was stained with an anti-pan cadherin antibody to observe cell-cell and cell-ECM interactions after cell lines were seeded into the matrix. Anti-pan cadherin staining results were observed to support the other results obtained. In all cell lines, especially on 24 h images, cellular aggregates bound together were observed within the scaffolds despite poor staining potential (Figure 5).

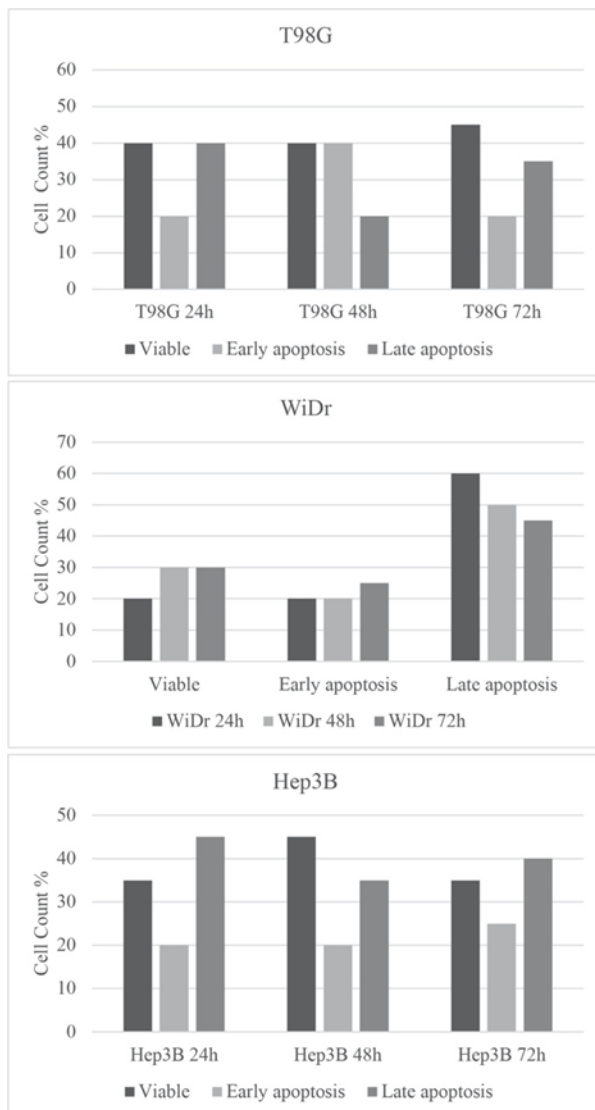


Figure 4. Graph of % apoptosis after AO/PI staining. Calculation of % was made by counting a total of 100 cells from 3 different photographs.

3. Discussion

Successfully designed decellularized tissues and organs should resemble the natural organ in size and structure and have similar biomechanical properties to these structures. It should also not induce an immunogenic response and should be able to support cell proliferation [22, 23].

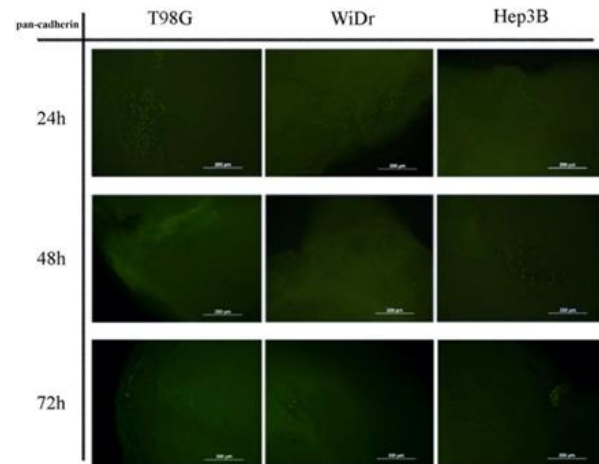


Figure 5. Pan-cadherin immunostaining of adipose matrix at different times (Magnification: $\times 10$).

In different studies, models known as chimeric, human cells on matrices obtained from different species have been tested, as well as studies in which matrix-cell interactions obtained from the same species are examined [18, 24]. The reason for this is the absence of immune cells in the matrices obtained by the decellularization process. Accordingly, detergent-based decellularization was used to decellularize rat adipose tissue within the scope of this study. Proliferation profiles of different cancer cell lines (T98G, WiDr, and Hep3B) were investigated on these matrices.

The ECM scaffolds that are naturally derived are ideal candidates for tissue engineering applications. This is in large part because the ECM establishes cell-cell and cell-matrix relationships while organizing cellular functions like differentiation and proliferation [18, 24]. Since adipose tissue is abundant in the body, it is widely used in tissue engineering as a source of ECM [25]. An extracellular matrix derived from human adipose tissue (hDAM) was employed in a previous study to study breast cancer growth, with the results showing that this system functions like a biomimetic microenvironment for cancer cells [18]. Dunne et al. [18] and Chaitin et al. [24] used both physical and chemical decellularization methods in their studies, whereas only chemical decellularization method was used in the current study. The most important difference between these two methods is that the damage that can be caused by the physical decellularization method in the extracellular matrix is minimized [18, 24]. At the same time, the short duration of the method used in the present study is an important factor for maintaining the integrity of the ECM. In our study, different from the studies mentioned above, different cancer cell types were examined. As a result of the literature review, no study was found with these cell types in terms of their adhesion capacity and cellular behavior on the decellularized adipose tissue matrix.

Various methods have been proposed and compared in the literature for the decellularization of adipose tissue [26, 27]. In this study, the detergent method we standardized in our previous studies was applied [12-14]. The most important difference of this method from other decellularization methods is its reduced application time and efficiency. These features of the detergent method made us think it might be preferable in the adipose tissue engineering approach, mainly because of the sensitive ECM of adipose tissue. In this study, decellularization results showed that dry, white, fibrous, and porous scaffolds were obtained. It was observed that the tissue structure was preserved, and the proliferative potential of different cancer cell lines had a profile close to the two-dimensional culture medium. AO/PI staining results also supported cell viability analysis.

Decellularized matrices of organs can serve as promising platforms for building in vitro cancer models. Its advantages include the specificity of the molecular composition of a particular organ and the preservation of tissue integrity; these properties allow for simulating the tumorigenesis processes with a high degree of affinity [28].

We used T98G, WiDr, and Hep3B cell lines to evaluate the ability to sustain cancer cell proliferation in the decellularized adipose matrixes we obtained. We have observed that the recellularization process is reproducible and reliable, but different cancer cells colonize the scaffold differently (**Figures 3 and 4**). In the three-dimensional matrix model, we observed that the tumor cells are located on the edge surfaces of the matrix. Moreover, in immunocytochemistry analyzes, we observed that cell-cell and cell-matrix interactions differ according to the proliferation potential of tumor cells in ECM. It was observed that T98G and Hep3B cells were more common in the margins of the matrix surface due to their easier access to nutrients and oxygen. This behavior of cells can be explained by the relationship between the location of the tumor tissue in the body close to the capillaries and the active proliferation power of cancer cells thanks to this location. The proliferation potential of T98G and Hep3B cells continued on the third day. This result showed that the decellularized scaffold has a cytocompatibility structure. The tissue architecture well preserved on AO/PI staining suggested that these cells have a much higher capacity for cell adhesion potential. However, the possibility of cells being deep in the tissue and not imaging with fluorescent staining is the limiting part of the study. Further studies (such as electron microscopic examination) are required to demonstrate cells embedded in the ECM.

4. Conclusion

As a result, it is seen that the porous structure of the adipose tissue matrix obtained by the chemical decellularization method preserves its natural ECM properties, and this tissue matrix can mimic the desired cancer tissue microenvironment. Removing cellular contents from the tissue with the shortest processing time showed the method's effectiveness. The reduced processing time and the applicability of the method can make it a preferable method in decellularization methods. It was thought that the proliferation profile of T98G, WiDr, and Hep3B in these scaffolds should be examined for longer periods, and these scaffolds should be obtained from different tissues and tested according to the cancer model. Likewise, it can be said that studies should be designed considering that different cancer cells showed different proliferation behaviors on decellularized matrices and that the compatibility of cancer cells and matrix may differ in the in vitro model to be designed for this.

Acknowledgement

The author did not receive any specific grant for this research from any funding agency in the public, commercial, or not-for-profit sectors.

Author's Contributions

Esin Akbay Çetin: Conceptualized the study, performed the experiments and analyses of result, drafted and wrote the manuscript.

Ethics


In this study animal was used for experiment with the approval of the Hacettepe University Animal Care and Use Committee (Permit no. 2012/52).

References

- [1]. Kocarnik, J. M., Compton, K., et al., 2022, Cancer incidence, mortality, years of life lost, years lived with disability, and disability-adjusted life years for 29 cancer groups from 2010 to 2019: a systematic analysis for the global burden of disease study 2019. *JAMA Oncology*, 8: 420-444.
- [2]. Han, S. J., Kwon, S., Kim, K. S., 2022, Contribution of mechanical homeostasis to epithelial-mesenchymal transition. *Cellular Oncology*, 45:1119-1136.
- [3]. Walker, C., Mojares, E., del Río Hernández, A., 2018, Role of extracellular matrix in development and cancer progression. *International Journal of Molecular Sciences*, 19:3028.
- [4]. Sensi, F., D'Angelo, E., et al., 2020, Recellularized colorectal cancer patient-derived scaffolds as in vitro pre-clinical 3D model for drug screening. *Cancers*, 12:681.

- [5]. Brancato, V., Oliveira, J.M., et al., 2020, Could 3D models of cancer enhance drug screening?. *Biomaterials*, 232:119744.
- [6]. Pospelov, A.D., Timofeeva, L.B., et al., 2020, Comparative analysis of two protocols of mouse tissues decellularization for application in experimental oncology. *Opera Medica et Physiologica*, 7:13.
- [7]. Ferreira, L.P., Gaspar, V.M., 2020, Decellularized extracellular matrix for bioengineering physiometric 3D in vitro tumor models. *Trends in Biotechnology*, 38:1397-1414.
- [8]. Rijal, G., Li, W., 2018, Native-mimicking in vitro microenvironment: an elusive and seductive future for tumor modeling and tissue engineering. *Journal of Biological Engineering*, 12:1-22
- [9]. Mavrogatou, E., Pratsinis, H., et al., 2019, Extracellular matrix alterations in senescent cells and their significance in tissue homeostasis. *Matrix Biology*, 75:27-42.
- [10]. Theocharis, A.D., Karamanos, N.K., 2019, Proteoglycans remodeling in cancer: Underlying molecular mechanisms. *Matrix Biology*, 75:220-259.
- [11]. Ajeti, V., Lara-Santiago, J., et al., 2017, Ovarian and breast cancer migration dynamics on laminin and fibronectin bi-directional gradient fibers fabricated via multiphoton excited photochemistry. *Cellular and Molecular Bioengineering*, 10:295-311.
- [12]. Sesli, M., Akbay, E., Onur, M. A., 2018, Decellularization of rat adipose tissue, diaphragm, and heart: a comparison of two decellularization methods. *Turkish Journal of Biology*, 42:537.
- [13]. Akbay, E., Onur, M. A., 2019, Investigation of survival and migration potential of differentiated cardiomyocytes transplanted with decellularized heart scaffold. *Journal of Biomedical Materials Research Part A*, 107:561-570.
- [14]. Akbay, E., Onur, M. A., 2018, Myocardial Tissue Engineering: A Comparative Study of Different Solutions for Use as a Natural Scaffold Being of Heart a Comparative Study of Different Solutions for Decellularization Heart Scaffold. *Biomedical Journal*, 2:4.
- [15]. Thevenot, P., Nair, A., et al., 2008, Method to analyze three-dimensional cell distribution and infiltration in degradable scaffolds. *Tissue Engineering Part C Methods*, 14:319-31.
- [16]. Lim, P.J., Gan, C.S., et al., 2019, Lipid lowering effect of *Eurycoma longifolia* Jack aqueous root extract in hepatocytes. *Kuwait Journal of Science*, 46: 2.
- [17]. Wang, L., Johnson, J.A., et al., 2013, Combining decellularized human adipose tissue extracellular matrix and adipose-derived stem cells for adipose tissue engineering. *Acta Biomaterialia*, 9:8921-31.
- [18]. Dunne, L.W., Huang, Z., et al., 2014, Human decellularized adipose tissue scaffold as a model for breast cancer cell growth and drug treatments. *Biomaterials*, 35:4940-49.
- [19]. Tığlı, S.R., Ghosh, S., et al., 2009, Comparative chondrogenesis of human cell sources in 3D scaffolds. *Journal of Tissue Engineering and Regenerative Medicine*, 3:348-60.
- [20]. Abdel Wahab, S.I., Abdul, A.B., et al., 2009, In vitro ultramorphological assessment of apoptosis induced by Zerumbone on (HeLa). *Journal of Biomedicine and Biotechnology*, 2009.
- [21]. Mosmann, T., 1983, Rapid colorimetric assay for cellular growth and survival: application to proliferation and cytotoxicity assays. *Journal of Immunological Methods*, 65:55-63.
- [22]. Gubareva, E.A., Sjöqvist, S., et al., 2016, Orthotopic transplantation of a tissue engineered diaphragm in rats. *Biomaterials*, 77:320-35.
- [23]. Fisher, M.F., Rao, S.S., 2020, Three-dimensional culture models to study drug resistance in breast cancer. *Biotechnology and Bioengineering*, 117:2262-78.
- [24]. Chaitin, H., Lu, M.L., et al., 2021, Development of a decellularized porcine esophageal matrix for potential applications in cancer modeling. *Cells*, 10:1055.
- [25]. Flynn, L.E., 2010, The use of decellularized adipose tissue to provide an inductive microenvironment for the adipogenic differentiation of human adipose-derived stem cells. *Biomaterials*, 31:4715-24.
- [26]. Brown, B.N., Freund, J.M., et al., 2011, Comparison of three methods for the derivation of a biologic scaffold composed of adipose tissue extracellular matrix. *Tissue Engineering Part C Methods*, 17:411-21.
- [27]. Chun, S.Y., Lim, J.O., et al., 2019, Preparation and characterization of human adipose tissue-derived extracellular matrix, growth factors, and stem cells: a concise review. *Tissue Engineering and Regenerative Medicine*, 16:385-93.
- [28]. Varol, C., Sagi, I., 2018, Phagocyte-extracellular matrix crosstalk empowers tumor development and dissemination. *The FEBS Journal*, 285:734-51.

Epigenetic Alterations in Mouse Muscle Cells After In Vitro Treatments with COVID-19 and Influenza Vaccines

Selcen Çelik Uzuner^{1*} 

¹ Department of Molecular Biology and Genetics, Faculty of Science, Karadeniz Technical University, Trabzon, Türkiye

*selcen.celik@ktu.edu.tr

*Orcid No: 0000-0002-9558-7048

Received: 1 February 2023

Accepted: 15 June 2023

DOI: 10.18466/cbayarfbe.1245847

Abstract

The importance of vaccination has come up again with a new form of coronavirus disease, COVID-19, which appeared in late 2019. This virus spread very fast around the globe, and it has numerous variants determined so far. Many studies focus on the effects of COVID-19 in humans and clinical-follow up after vaccination for the understanding whether the disease has been taken under control. Other studies mostly focus on omics analyses and molecular characteristics of COVID-19 itself. However, this is not clear whether COVID-19 vaccines induce epigenetic differences in the host tissues. This study aimed to reveal whether *in vitro* treatment of muscle cells with mRNA-based vaccine for COVID-19 and/or attenuated vaccines (whole virus attenuated for COVID-19 or split virion for quadrivalent influenza) can result in the changes in the global levels of DNA methylation (5meC) and/or DNA hydroxymethylation (5hmC). DNA methylation and DNA hydroxymethylation were individually detected by immunofluorescence and global patterns of epigenetic marks were analysed by fluorescence microscopy in mouse muscle cells after the incubation with vaccines for 24h or 48h. Results showed that each type of attenuated vaccine induced epigenetic changes by different patterns, but the mRNA-based vaccine affected both global levels of 5meC and 5hmC in a similar manner. Findings indicate that vaccines can affect epigenome. These preliminary results suggest that epigenetic profiles of specific genes across different human tissues after vaccination may add further information, therefore, reveal biological significance in detail.

Keywords: COVID-19, coronavirus, influenza, vaccine, epigenetics, DNA methylation, DNA hydroxymethylation

1. Introduction

The COVID-19 pandemic has been an important situation around the globe since late 2019. This is caused by SARS-CoV2 (Severe Acute Respiratory Syndrome CoronaVirus-2) that has several mutant variants (1,2). Although there are other members of *Coronaviruses* that share similarity with COVID-19 in terms of genomic pattern and symptomatic effects, COVID-19 is the variant that spread rapidly around the world. Today, all countries suffer from clinical, social, and economic outcomes of the pandemic. Dealing with the spread, treatment and protection has been of the main interest in governments and scientific institutions. There are different vaccine strategies to protect people from the mortal effects of COVID-19 as inducing the immune recognition and response in advance. Vaccination rate

around the world has been increasing by time. Some groups of vaccines are produced by classical attenuation methods, but other types are produced using new approaches of biotechnology, such mRNA technology, adenovirus-based methods, and virus-like particles, or combined of classical and new methods.

Use of vaccines has been an old but still useful approach to fight with infections. The classical vaccines derived by Pasteur's method are attenuated whole viruses that induce immune response against the pathogens before possible infection in the future. mRNA-based vaccine technology is a rather new and biotechnologically produced vaccine. These are not routinely used in the clinic but for COVID-19 infection F.D.A. has urgently approved mRNA vaccine. This technology has been broadly examined for cancer prevention (3,4) as well as

infectious diseases including viral (5) and bacterial antigens (6). In the clinic, the immunity of vaccines is primarily studied by comparing unvaccinated and vaccinated people (7,8). There are also some studies using drug repurposing strategies (9,10) or newly synthesized compounds for COVID-19 therapy (11,12). However, the effect of vaccines at molecular level has remained unclear. Epigenetic regulations are the machineries in the cells that manage differential gene expression for a range of various extra-, intra-, and intercellular stimuli. The vaccines can regulate the epigenome of the host organism by the changes in the genes/proteins involved in the innate and adaptive system (13,14) as well as the infections themselves (15). The epigenetic response in the cells after COVID-19 vaccination is one of the interests, and this study aims to elucidate global methylation and hydroxymethylation patterns after vaccine treatments *in vitro*. To the best of knowledge, there is no understanding of epigenetic (including 5mC and 5hmC) patterns in the genome of host muscle cells right after vaccination for COVID-19.

2. Materials and Methods

2.1. Cell culture and vaccine treatments

Sol8 (ATCC, CRL-2174TM) mouse muscle cells were cultured in DMEM (Wisent Inc., Cat No 319-005-CL, Quebec, Canada) media including 10% fetal bovine serum (Capricorn Scientific GmbH, Cat No FBS11-A, Ebsdorfergrund, Germany) and 1% penicillin-streptomycin (Wisent, Cat No 450-201-EL) antibiotics at 37°C humidified with 5% CO₂ until reach to 80% confluency. Cells were seeded as 25000 cells per well in a 96-well plate. After they reached to confluency, they were treated with vaccines individually for 24h or 48h. COVID-19 vaccines used were 1) inactive whole virus attenuated (Sinovac/CoronaVac, Sinovac Biontech Ltd.; Beijing, P.R. China) and 2) mRNA-based vaccine, BNT162b2 (Biopharmaceutical New Technologies, BioNTech; Mainz, Germany). Both COVID-19 vaccines have been developed using wild type COVID-19 which is the first variant raised in China resulting in the pandemic. Adjuvant compounds in inactive attenuated COVID-19 vaccine are aluminium hydroxide, sodium chloride, sodium hydroxide and monosodium and disodium hydrogen sulphate, dissolved in water (Sinovac Research & Development Co., Ltd, China). Ingredients in mRNA COVID-19 vaccine includes mRNA (for spike protein of the virus) and lipids ((4-hydroxybutyl)azanediyl)bis(hexane-6,1-diyl)bis(2hexyldecanoate), 2 [(polyethylene glycol)-2000]-N,N-ditetradecylacetamide, 1,2 Distearoyl-sn-glycero-3-phosphocholine, and cholesterol). Adjuvant compounds in mRNA based COVID-19 vaccine include potassium chloride, monobasic potassium phosphate, sodium chloride, dibasic sodium phosphate dihydrate, and sucrose or tromethamine, tromethamine hydrochloride, and sucrose (16) (Table 1).

Influenza vaccine (VAXIGRIP TETRA; manufactured by Sanofi Pasteur, France to TURKEY) used were inactive split virion. Influenza vaccine includes 1) 15 micrograms of A/Victoria/2570/2019 (H1N1) pdm09- (A/Victoria/2570/2019, IVR-215) like variant, 2) 15 micrograms of A/Cambodia/e0826360/2020 (H3N2) – (A/Tasmania/503/2020, IVR-221) like variant, 3) 15 micrograms of B/Washington/02/2019- (B/Washington/02/2019, wild type) like variant and 4) 15 micrograms of B/Phuket/3073/2013, wild type) like variant. Adjuvants in influenza vaccine are sodium chloride, potassium chloride, disodium phosphate dihydrate, potassium dihydrogen phosphate, dissolved in water and traces of ovalbumin (egg protein), neomycin, octoxinol-9, and formaldehyde (Sanofi Pasteur, Turkey) (Table 1). But prescriptions do not indicate final concentrations of adjuvants in the vaccines used.

Estimation of the dose /concentration for application to cells was carried out as follows: 1) In clinical use, 500 microliters of vaccine (for inactive COVID-19 and inactive influenza vaccines) and 300 microliters of vaccine (for mRNA-based COVID-19) have been applied to individuals intramuscularly. An average number of total human cells in a body is around 30 trillion cells (30x10¹²) (17). 2) 500 µl of vaccine is applied for 30x10¹² cells so that 1 µl of vaccine is applicable for 6x10¹⁰ cells, only 1 µl of vaccine is taken from leftovers of vaccines that were used in the clinic. 3) Main stocks of the vaccines were prepared as 1 µl of vaccine in 1000 µl of culture media (for 6x10⁷ cells). 4) Main stock was diluted depending on the cell number subjected to be treated with vaccine and the total volume of media needed for the cells cultured in a number of wells in the 96 well plate. *i.e.*, in a design that 400.000 cells seeded into 16 wells, the main stock vaccine was diluted 1:150 in total media (ml) needed (200 µl per well) and split into the wells. Control wells were left untreated, but media without vaccines was renewed. For mRNA-based vaccine used as 300 µl, a similar calculation was performed.

2.2. Immunofluorescence

After treatment, cells were stained by immunofluorescence method as previously described (18). In this protocol, media was removed from the vessels and cells were then washed with 1xPBS (phosphate buffered saline) (with calcium and magnesium ions that facilitate adhesion of cells onto culture vessel) (Wisent, Cat No 311-011-CL) for 3 times. After washing, cells were fixed with 4% paraformaldehyde (w/v) (ChemSolute, Th. Geyer GmbH & Co., Cat No 8416-0500, Germany) for 15 minutes at 37°C followed by 1xPBS wash for 3 times.

Fixed cells were then permeabilized with 1xPBS including 0.75% (v/v) Triton-X (Biomatik, Cat No A4025) and 0.75% (v/v) Tween-20 (Sigma Aldrich Co., Cat No P1379, St. Louis) for 1 hr at RT. After permeabilization, cells were blocked in 50% (v/v) goat serum (Capricorn, Cat No GOA-1B) in 1XPBS at 4°C overnight. Some cells were incubated with mouse anti-5meC-antibody (1:400) (Active Motif, Carlsbad, CA, US, Cat No 39649) for 1h at room temperature (RT), others with rabbit anti-5hmC antibody (1:500) (Active Motif, Cat No 39791) for 2.5h at RT. After primary antibody incubation, secondary antibodies including either anti-mouse Alexa-488 (Abcam, Cat No 150113) for 5meC (1:400) or 2) anti-rabbit Alexa-488 (Abcam, Cat No 150077) for 5hmC (1:500) were treated for 1h and 2h at RT in the dark, respectively. Secondary antibodies were then removed and washed with 1xPBS for 3 times. Staining patterns were visualized under the fluorescence microscope (AxioVert, Zeiss, Germany). Microscopy images were captured with an integrated camera using a set of gamma and exposure values.

2.3. ImageJ Analysis

Microscope images were analysed using ImageJ (NIH, US) software. For this, the colour threshold was set first for each image. After individual nuclei were automatically selected in each image, mean fluorescence intensity and area were measured for each nucleus. Total staining of 5meC or 5hmC (arbitrary units, a.u) were then calculated by mean fluorescence intensity \times nucleus area. Total staining values (Sum values, arbitrary units, a.u) were represented by bar graphs using SPSS software (Version 23) and shown with \pm standard error of the mean from three repeats.

2.4. Statistics

The comparison of sum values was performed by univariate analysis of variance (UNIANOVA) of SPSS software. Pair-wise analyses were performed using post-Hoc analysis. Significance levels used were $p < 0.05$ (*), $p < 0.01$ (**), $p < 0.001$ (***), and $p < 0.0001$ (****).

Table 1. Comparison of adjuvants in each vaccine.

Adjuvant Compounds	Attenuated inactive COVID-19	Split virion inactive Influenza	mRNA based COVID-19
Sodium chloride	Yes	Yes	Yes
Aluminium hydroxide	Yes	No	No
Potassium chloride	No	Yes	Yes
Sodium hydroxide	Yes	No	No
Monosodium hydrogen sulphate	Yes	No	No
Disodium hydrogen sulphate	Yes	No	No
Monobasic potassium phosphate	No	No	Yes
Dibasic sodium phosphate dihydrate	No	No	Yes
Sucrose	No	No	Yes
Tromethamine	No	No	Occasional
Tromethamine hydrochloride	No	No	Yes
Disodium phosphate dihydrate	No	Yes	No
Potassium dihydrogen phosphate	No	Yes	No
Ovalbumin (egg protein)	No	Yes	No
Neomycin	No	Yes	No
Octoxinol-9	No	Yes	No
Formaldehyde	No	Yes	No
Water	Yes	Yes	No

3. Results and Discussion

After the treatment with whole virus attenuated, global level of DNA methylation (5meC) significantly increased at 24h ($p = 0.000$) but decreased for additional 24h ($p \leq 0.025$) (Figure 1). After mRNA-based vaccine, its level did not change at 24h ($p > 0.05$), whereas this amount decreased at 48h ($p = 0.000$) compared to untreated cells (Figure 2). After the inactive split virion vaccine, DNA methylation pattern was completely opposite compared to treatment with whole virus attenuated as it decreased

at 24h ($p \leq 0.013$) but increased at 48h ($p = 0.000$) (Figure 3).

In contrast to DNA methylation, the level of DNA hydroxymethylation (5hmC) decreased at 24h ($p = 0.000$) but increased at 48h ($p = 0.000$) after whole virus attenuated (Figure 4). mRNA-based vaccine induced similar alterations in DNA hydroxymethylation as in DNA methylation with a significant decrease at 48h only (Figure 5). After the inactive split virion vaccine, 5hmC level was only changed at 48h with an increase as well as 5meC. But differentially this was not affected at short-

term ($p > 0.05$) (**Figure 6**). **Table 2** shows comparisons for each vaccine treatment with significance (p values) and level trends (increase or decrease) for each epigenetic mark. Preliminary results indicate that 5mC and 5hmC patterns have a tendency towards similar reprogramming after mRNA-based and split virion vaccines, but whole virus inactivated vaccine induced an opposite effect for both.

This study aimed to understand whether two major epigenetic modifications occurring on DNA (5mC and 5hmC) are significantly affected after vaccine treatments of cells in the culture. These results suggest that vaccines are able to induce epigenetic reprogramming in the cells (muscle cells in the present study) by different patterns. However, this study does not explore or declare any biological significance of these patterns at gene or cell level. Nevertheless, the results create awareness about the potential of vaccines in terms of epigenetic regulations.

Vaccines are the savers of human life by assisting the immune system to prepare itself before infections and even cancer. As all the compounds including numerous drugs, vaccines are supposed to change epigenetic mechanisms in the cells. This is not surprising that the epigenome, a dynamic representative of the genome, is subject to alter after internal and external stimuli. Although the genome is more robust and rigid in terms of changes in DNA sequence, the epigenome is a kind of dynamic response of cells to any conditions so that it regulates gene expressions to manage the current situation. The vaccination can regulate the host epigenome in particular genes involved in adaptive and innate immunity. For instance, BCG vaccine, (Bacille Calmette-Guerin, a vaccine for tuberculosis) induced NOD2 receptor pathway which is involved in innate immunity, compared to unvaccinated counterparts (19,20). BCG vaccine also stimulated the changes in TNF- α and IL-6 promoters which are related to inflammation (19). A study with healthy people (50–74-year-olds) showed that the changes in the genome wide DNA methylation patterns were at low level whereas the levels of methylation in a specific group of CpG sites were decreased, and these changes were associated with lower humoral immune response to influenza vaccination (13). Correspondingly, decrease in the level of *RNF39* gene which encodes a transcription factor in the major histocompatibility complex (MHC) class I region, was found to be related with a weak response against HBV vaccine in newborns (14). The response of vaccines in terms of epigenetics has been found to be associated with age. The study showed a high level of epigenetic reprogramming in older people (>50 years-old) after influenza vaccination (21). These suggest that vaccination can reprogram the host's epigenome during the response of immunization. This should be also noted that infections can also induce epigenetic changes in the infected organism. The patterns of DNA methylation in

more than 500 genes were found to be different in newborns exposed to active HBV infection in utero (15). But, to the best of knowledge there has been no study that tried to experience global epigenetic changes in the host genome after COVID-19 vaccination. This study presents the first preliminary findings for possible changes in epigenetic patterns after *in vitro* treatment of mouse cells with two different types of COVID-19 vaccines and an influenza viral vaccine, and the findings point out that each type of viral vaccine significantly affected the host epigenome but through different ways. This is also the first study to examine the second-common DNA modification, 5hmC-DNA hydroxymethylation, after both COVID-19 and influenza vaccine treatments *in vitro*. However, this study does not provide any information at the gene level and is limited to only one cell line from rats. Human cells should be included, and even *in vivo* studies can give more comprehensive outcomes, *i.e.*, blood cells can be obtained from vaccinated people. This will lead to understanding the direct effect of vaccines on immune system cells. The vaccines may regulate the epigenome of the immune system cells in the process of pathogen recognition for the future. This is also possible that infection, *i.e.*, COVID-19, can affect the host's epigenome to trigger immunizations (22). Previous works identified detailed epigenetic changes in the host genome after trivalent influenza vaccination containing the influenza A/California/7/2009 H1N1-like, A/Perth/16/2009 H3N2-like and B/Brisbane/60/2008-like viral strains. (23). These changes include a range of pathways regulating immune response such as T cell receptor pathway, T cell activation and golgi to plasma membrane protein transport for short term (3 days) and long term (28 days). The presented study, to the best of the knowledge, is the first to evaluate epigenetic response in the muscle cells after COVID-19 vaccination. However, by this study, it is hard to conclude the biological significance of the observed changes, but statistical significance exists. Revealing gene and/or tissue specific changes provides a broader perspective for the effects of vaccines in detail. Upregulation of genes by changes in epigenetic markers on DNA may be relevant to immunization of cells against the pathogen. Immunization is not only for immune system cells but also fibroblast cells were shown to have immunization activity as well (24–26). Muscle has been known to play a mediator role for immune system training (27) so that it supports the epigenomic changes in muscle cells after vaccination. Vaccines are applied intramuscularly; thereby muscle cells are the first responsive cells in the body.

Another limitation of this study is not to include a group of control cells treated with adjuvant compounds only. This is because lists of adjuvants are given in each vaccine (**Table 1**), but the concentrations of adjuvants are not provided. This limits the mimicking of the precise content within the vaccines and reliability of the

experiments. Control cells were therefore designed with only canonical cell culture media environment. One or more adjuvants possibly can affect the host epigenome itself. For instance long term exposure of low dose formaldehyde (exist in only influenza vaccine used in the present study) induced decrease in the global level of DNA methylation in human bronchial epithelial cell line (28). A kind of detergent, Octoxinol-9, another adjuvant in influenza vaccine, is declared as safe compared to other octoxinols (octoxynols) which are shorter chain than 8 (29), but there is no study showing its effect on epigenetic profile. A part of the epigenome is open to change after intra- and extracellular inducements, but these do not always mean a pathological response.

The attenuated vaccines are a kind of whole virus inactivated vaccine, such one produced by Sinovac. The split-virion vaccines are also inactivated but these are

produced by disruption of virus envelope and releasing the virion particles (30), such as the quadrivalent influenza vaccine used in the study. mRNA based vaccines are totally different from other types as mRNA of target protein within the virus genome is packaged within a liposomal structure. The different designs of three vaccines examined suggest the different epigenetic response in the cells. The changes in the levels of DNA methylation and DNA hydroxymethylation were found to differ from treatments of each vaccine in this study. The variation may be derived from the differential structures of vaccines suggesting regulation of different cellular responses. To reveal the biological action within the cells, detailed investigations based on whole genome sequencing are required.

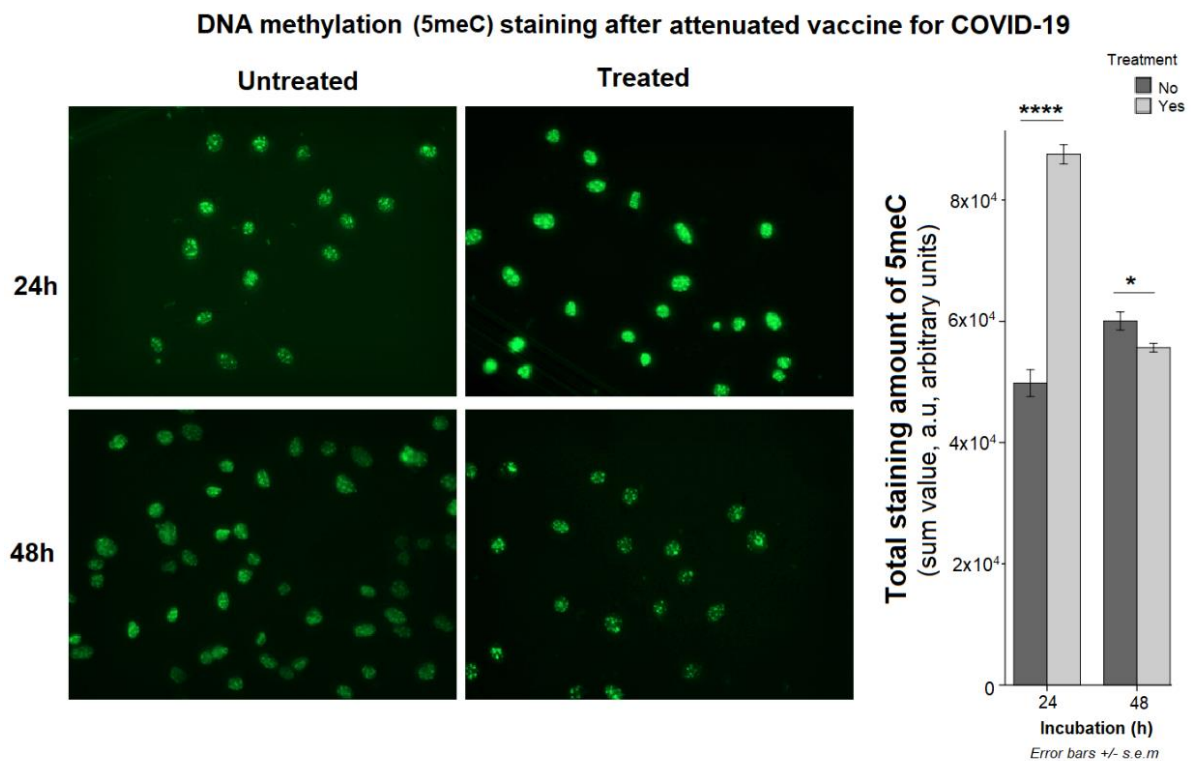


Figure 1. DNA methylation profile after attenuated vaccine for COVID-19.

DNA methylation (5meC) staining after mRNA vaccine for COVID-19

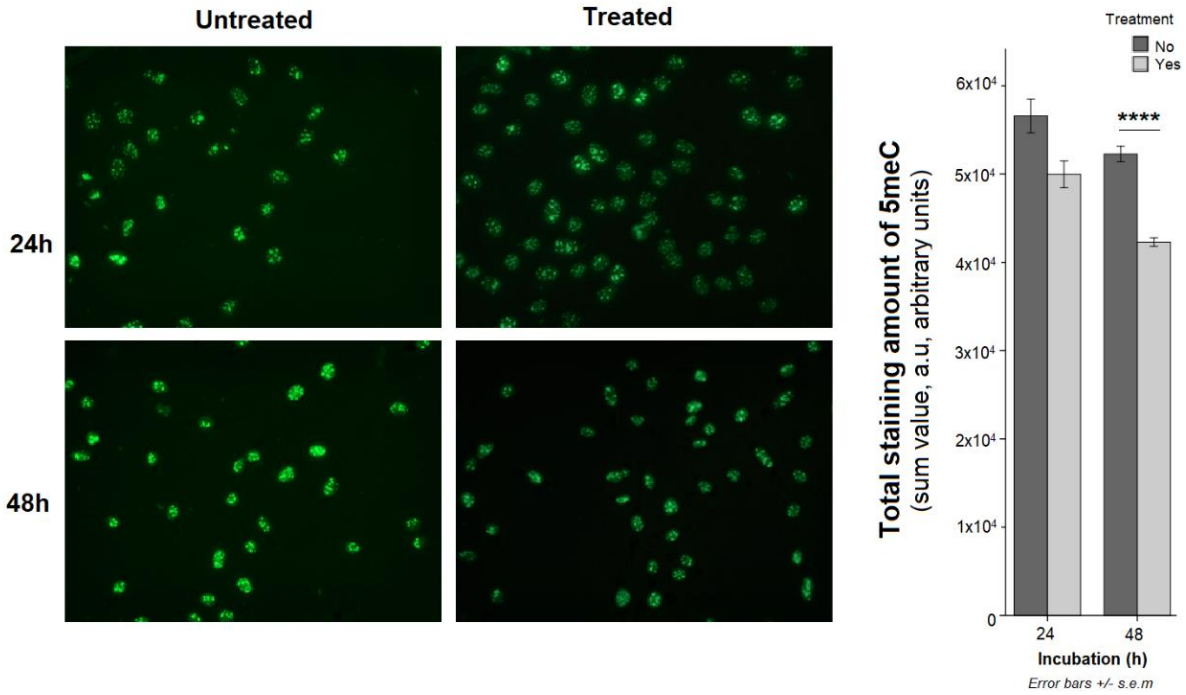


Figure 2. DNA methylation profile after mRNA vaccine for COVID-19.

Table 2. Significant changes in epigenetic markers of DNA (5meC and 5hmC) after vaccines in vitro.

Vaccine Type	Incubation	Comparison	5meC	5hmC
Whole virus attenuated (COVID-19)	24	Untreated vs Treated	$p \leq 0.000$ ↑	$p \leq 0.000$ ↓
	48		$p \leq 0.025$ ↓	$p \leq 0.000$ ↑
mRNA based (COVID-19)	24		n.s ×	n.s ×
	48		$p \leq 0.000$ ↓	$p \leq 0.000$ ↓
Inactive split-virion (Influenza)	24		$p \leq 0.013$ ↓	n.s ×
	48		$p \leq 0.000$ ↑	$p \leq 0.000$ ↑

n.s; not significant ↑ increase ↓ decrease

DNA methylation (5meC) staining after inactive split virion influenza vaccine

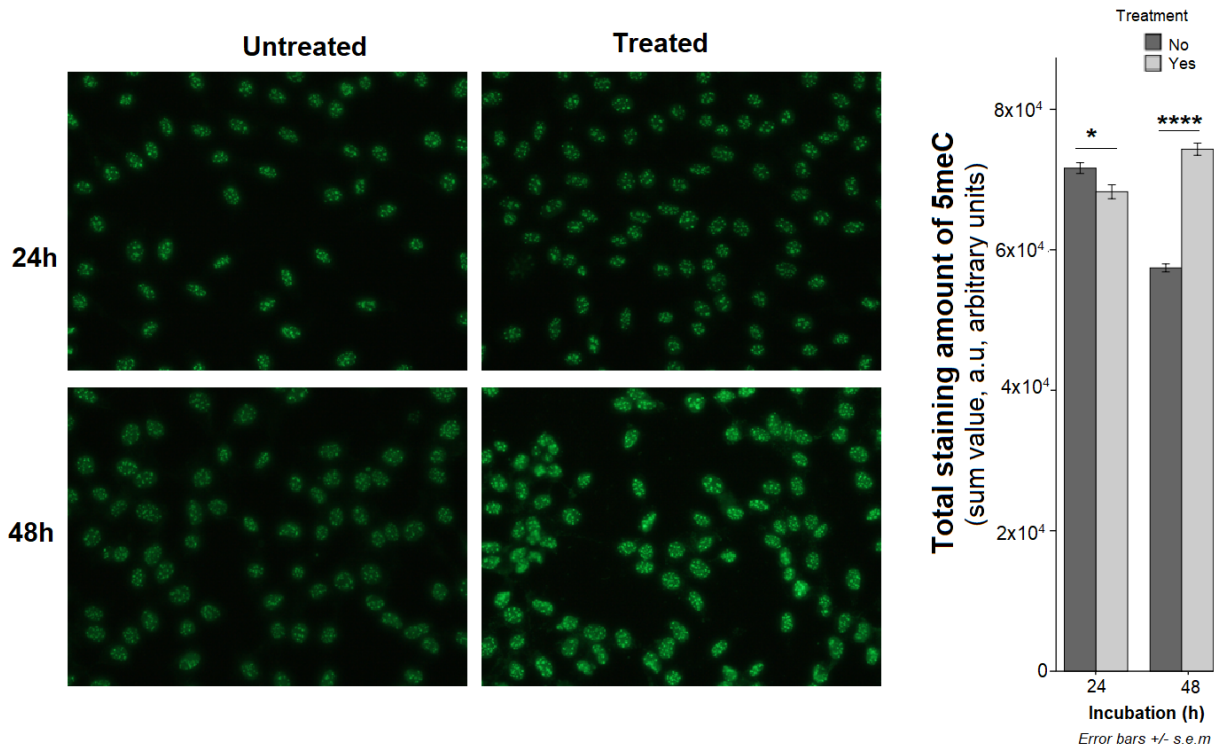


Figure 3. DNA methylation profile after inactive split virion influenza vaccine.

DNA hydroxymethylation (5hmC) staining after attenuated vaccine for COVID-19

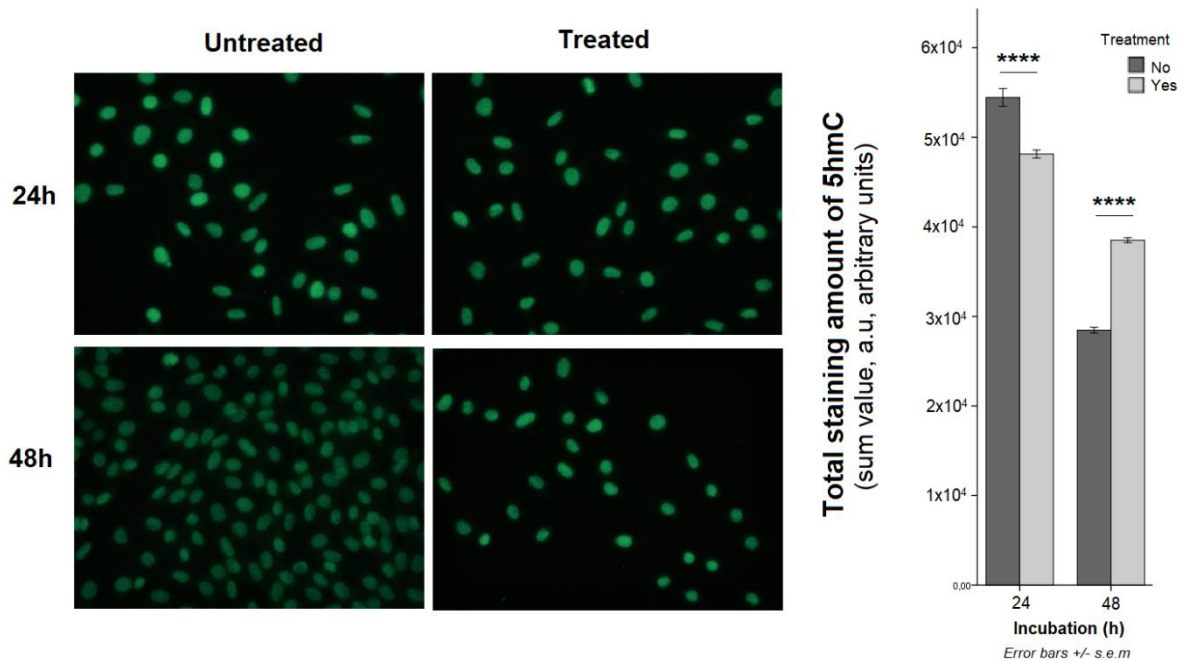


Figure 4. DNA hydroxymethylation profile after attenuated vaccine for COVID-19.

DNA hydroxymethylation (5hmC) staining after mRNA vaccine for COVID-19

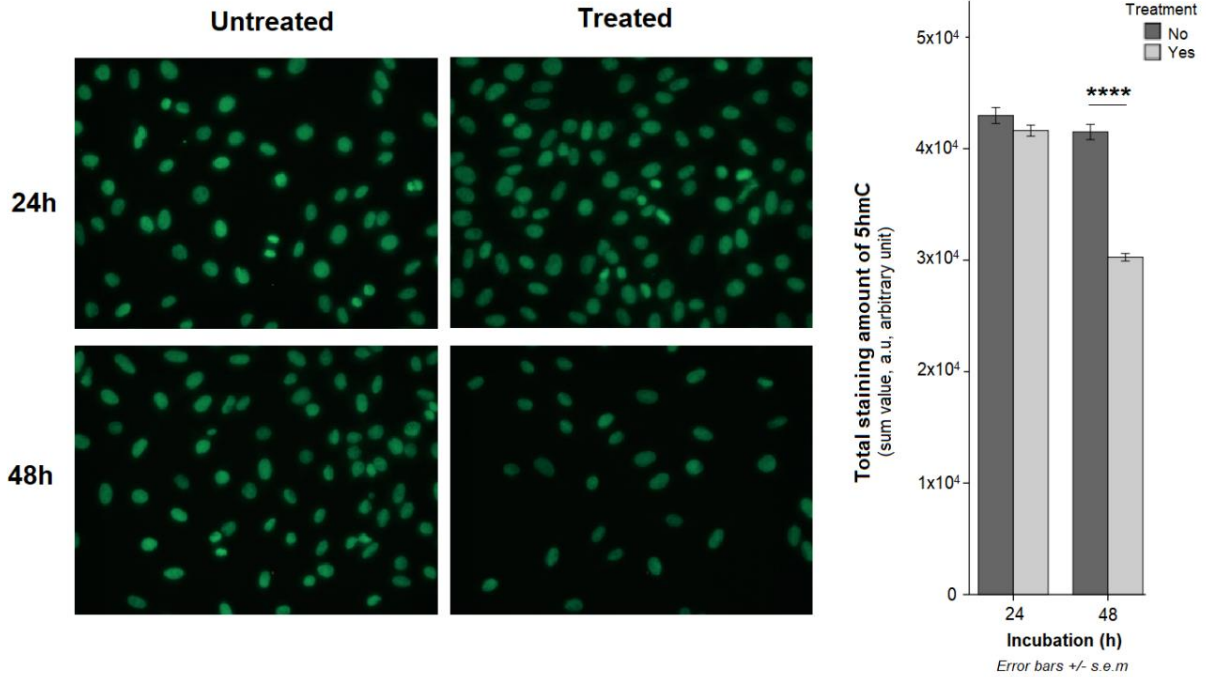


Figure 5. DNA hydroxymethylation profile after mRNA vaccine for COVID-19.

DNA hydroxymethylation (5hmC) staining after inactive split virion influenza vaccine

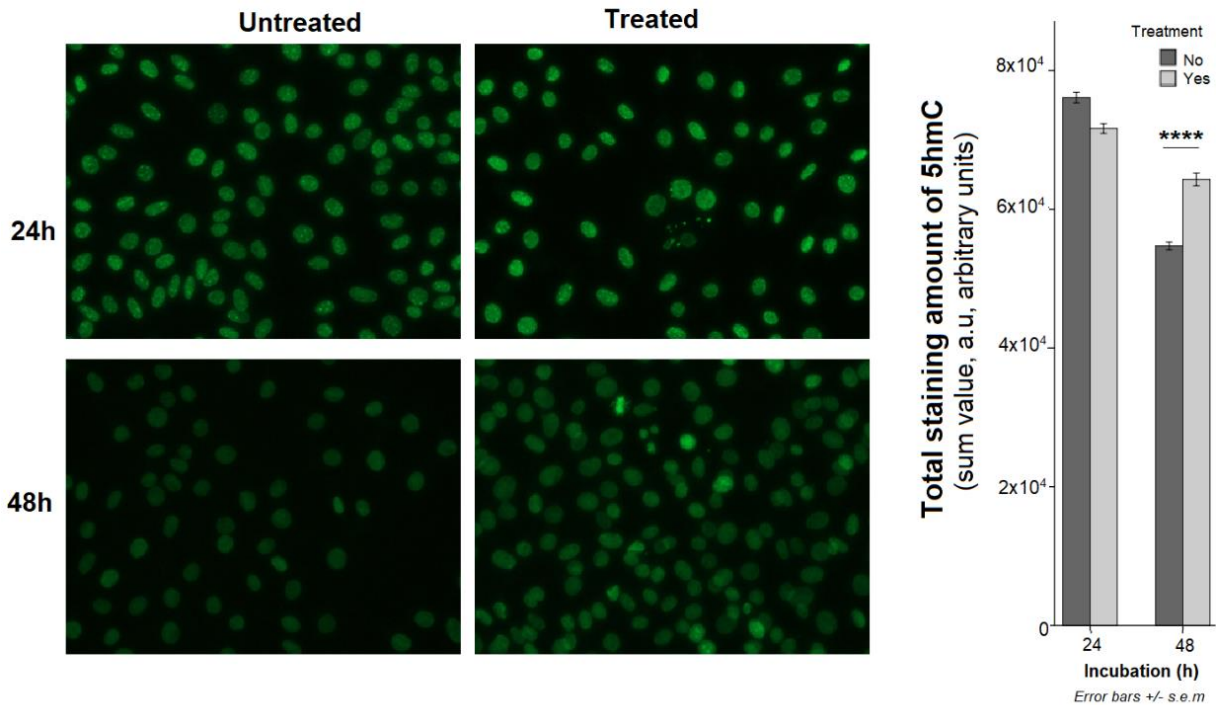


Figure 6. DNA hydroxymethylation profile after inactive split virion influenza vaccine.

4. Conclusion

This study suggests that different type of vaccines can make global epigenetic changes on the individuals who are vaccinated. However, this study only was performed in vitro and using muscle cells. Comprehensive in vitro studies and further in vivo studies are required to make a broader conclusion.

Acknowledgement

This study was not funded by any institutions.

Author's Contributions

Selcen Çelik Uzuner: Hypothesized the study, performed the experiments, and wrote the manuscript.

Ethics


There are no ethical issues after the publication of this manuscript.

References

- [1]. Lauring AS, Tenforde MW, Chappell JD, Gaglani M, Ginde AA, McNeal T, et al. Clinical severity of, and effectiveness of mRNA vaccines against, covid-19 from omicron, delta, and alpha SARS-CoV-2 variants in the United States: prospective observational study. *BMJ* [Internet]. 2022 Mar 9 [cited 2022 Apr 21];376:e069761. Available from: <https://www.bmj.com/content/376/bmj-2021-069761>
- [2]. Rahimi F, Talebi Bezin Abadi A. The Omicron subvariant BA.2: Birth of a new challenge during the COVID-19 pandemic [Internet]. Vol. 99, *International Journal of Surgery*. Elsevier; 2022 [cited 2022 Apr 21]. p. 106261. Available from: [/pmc/articles/PMC8837492/](https://pubmed.ncbi.nlm.nih.gov/35139340/)
- [3]. Fiedler K, Lazzaro S, Lutz J, Rauch S, Heidenreich R. mRNA cancer vaccines. In: *Recent Results in Cancer Research* [Internet]. Springer, Cham; 2016 [cited 2022 Apr 21]. p. 61–85. Available from: https://link.springer.com/chapter/10.1007/978-3-319-42934-2_5
- [4]. Rausch S, Schwentner C, Stenzl A, Bedke J. mRNA vaccine CV9103 and CV9104 for the treatment of prostate cancer. *Hum Vaccines Immunother* [Internet]. 2014 Nov 1 [cited 2022 Apr 21];10(11):3146–52. Available from: <https://www.tandfonline.com/doi/abs/10.4161/hv.29553>
- [5]. Brazzoli M, Magini D, Bonci A, Buccato S, Giovani C, Kratzer R, et al. Induction of Broad-Based Immunity and Protective Efficacy by Self-amplifying mRNA Vaccines Encoding Influenza Virus Hemagglutinin. *J Virol* [Internet]. 2016 Jan 14 [cited 2022 Apr 21];90(1):332–44. Available from: <https://journals.asm.org/doi/full/10.1128/JVI.01786-15>
- [6]. Maruggi G, Chiarot E, Giovani C, Buccato S, Bonacci S, Frigimelica E, et al. Immunogenicity and protective efficacy induced by self-amplifying mRNA vaccines encoding bacterial antigens. *Vaccine*. 2017 Jan 5;35(2):361–8.
- [7]. Liu J, Chandrashekar A, Sellers D, Barrett J, Jacob-Dolan C, Lifton M, et al. Vaccines elicit highly conserved cellular immunity to SARS-CoV-2 Omicron. *Nature* [Internet]. 2022 Mar 17 [cited 2022 Apr 21];603(7901):493–6. Available from: <https://pubmed.ncbi.nlm.nih.gov/35102312/>
- [8]. Tarke A, Coelho CH, Zhang Z, Dan JM, Yu ED, Methot N, et al. SARS-CoV-2 vaccination induces immunological T cell memory able to cross-recognize variants from Alpha to Omicron. *Cell* [Internet]. 2022 Mar 3 [cited 2022 Apr 21];185(5):847–859.e11. Available from: <https://pubmed.ncbi.nlm.nih.gov/35139340/>
- [9]. Ng YL, Salim CK, Chu JJH. Drug repurposing for COVID-19: Approaches, challenges and promising candidates [Internet]. Vol. 228, *Pharmacology and Therapeutics*. Pharmacol Ther; 2021 [cited 2022 Apr 21]. Available from: <https://pubmed.ncbi.nlm.nih.gov/34174275/>
- [10]. Chakraborty C, Sharma AR, Bhattacharya M, Agoramoorthy G, Lee SS. The Drug Repurposing for COVID-19 Clinical Trials Provide Very Effective Therapeutic Combinations: Lessons Learned From Major Clinical Studies. Vol. 12, *Frontiers in Pharmacology*. Frontiers Media S.A.; 2021. p. 2942.
- [11]. Li L, Huang S. Newly synthesized Mpro inhibitors as potential oral anti-SARS-CoV-2 agents. *Signal Transduct Target Ther* [Internet]. 2021 Mar 31 [cited 2022 Apr 21];6(1):1–2. Available from: <https://www.nature.com/articles/s41392-021-00560-0>
- [12]. Yayli N, Kiliç G, Celik G, Kahriman N, Kanbolat S, Bozdeveci A, et al. Synthesis of hydroxy benzoin/benzil analogs and investigation of their antioxidant, antimicrobial, enzyme inhibition, and cytotoxic activities. *Turkish J Chem* [Internet]. 2021 [cited 2022 Apr 21];45(3):788–804. Available from: [/pmc/articles/PMC8326476/](https://pubmed.ncbi.nlm.nih.gov/35139340/)
- [13]. Zimmermann MT, Oberg AL, Grill DE, Ovsyannikova IG, Haralambieva IH, Kennedy RB, et al. System-Wide Associations between DNA-Methylation, Gene Expression, and Humoral Immune Response to Influenza Vaccination. *PLoS One* [Internet]. 2016 Mar 31 [cited 2023 Jun 12];11(3). Available from: <https://pubmed.ncbi.nlm.nih.gov/27031986/>
- [14]. Lu Y, Cheng Y, Yan W, Nardini C. Exploring the molecular causes of hepatitis B virus vaccination response: an approach with epigenomic and transcriptomic data. *BMC Med Genomics* [Internet]. 2014 Mar 11 [cited 2023 Jun 12];7(1). Available from: <https://pubmed.ncbi.nlm.nih.gov/24612962/>
- [15]. Cheng Q, Zhao B, Huang Z, Su Y, Chen B, Yang S, et al. Epigenome-wide study for the offspring exposed to maternal HBV infection during pregnancy, a pilot study. *Gene* [Internet]. 2018 Jun 5 [cited 2023 Jun 12];658:76–85. Available from: <https://pubmed.ncbi.nlm.nih.gov/29526602/>
- [16]. Pfizer Inc., New York N 10017. Pfizer-BioNTech COVID-19 Vaccine | Pfizer [Internet]. 2022 [cited 2022 Apr 5]. Available from: <https://www.pfizer.com/products/product-detail/pfizer-biontech-covid-19-vaccine>
- [17]. Abbott A. Scientists bust myth that our bodies have more bacteria than human cells. *Nature*. 2016 Jan 8;
- [18]. Uzuner SÇ, Birinci E, Tetikoğlu S, Birinci C, Kolaylı S. Distinct Epigenetic Reprogramming, Mitochondrial Patterns, Cellular Morphology, and Cytotoxicity after Bee Venom Treatment. *Recent Pat Anticancer Drug Discov*. 2021;16(3):377–92.
- [19]. Arts RJW, Blok BA, Aaby P, Joosten LAB, de Jong D, van der Meer JWM, et al. Long-term in vitro and in vivo effects of γ -irradiated BCG on innate and adaptive immunity. *J Leukoc Biol* [Internet]. 2015 Dec 1 [cited 2023 Jun 12];98(6):995–1001. Available from: <https://pubmed.ncbi.nlm.nih.gov/26082519/>
- [20]. Strober W, Watanabe T. NOD2, an intracellular innate immune sensor involved in host defense and Crohn's disease. *Mucosal Immunol* 2011 45 [Internet]. 2011 Jul 13 [cited 2023 Jun 12];4(5):484–95. Available from: <https://www.nature.com/articles/mi201129>

- [21]. Gensous N, Franceschi C, Blomberg BB, Pirazzini C, Ravaioli F, Gentilini D, et al. Responders and non-responders to influenza vaccination: A DNA methylation approach on blood cells. *Exp Gerontol* [Internet]. 2018 May 1 [cited 2023 Jun 12];105:94–100. Available from: <https://pubmed.ncbi.nlm.nih.gov/29360511/>
- [22]. Cheong J-G, Ravishankar A, Sharma S, Parkhurst CN, Nehar-Belaid D, Ma S, et al. Epigenetic Memory of COVID-19 in Innate Immune Cells and Their Progenitors. *bioRxiv* [Internet]. 2022 Feb 10 [cited 2022 Apr 21];2022.02.09.479588. Available from: <https://www.biorxiv.org/content/10.1101/2022.02.09.479588v1>
- [23]. Zimmermann MT, Oberg AL, Grill DE, Ovsyannikova IG, Haralambieva IH, Kennedy RB, et al. System-wide associations between DNA-methylation, gene expression, and humoral immune response to influenza vaccination. *PLoS One* [Internet]. 2016 Mar 31 [cited 2022 Apr 21];11(3). Available from: [/pmc/articles/PMC4816338/](https://pubmed.ncbi.nlm.nih.gov/27145553/)
- [24]. Kaufman J, Graf BA, Leung EC, Pollock SJ, Koumas TM, Reddy SY, et al. Fibroblasts as sentinel cells: Role of the CD40-CD40 ligand system in fibroblast activation and lung inflammation and fibrosis. *Chest*. 2001;120(1):53S-55S.
- [25]. Bustos-Arriaga J, García-Machorro J, León-Juárez M, García-Cordero J, Santos-Argumedo L, Flores-Romo L, et al. Activation of the innate immune response against dengue in normal non-transformed human fibroblasts. *PLoS Negl Trop Dis* [Internet]. 2011;5(12). Available from: <https://pubmed.ncbi.nlm.nih.gov/22206025/>
- [26]. Hamada A, Torre C, Drancourt M, Ghigo E. Trained immunity carried by non-immune cells. Vol. 10, *Frontiers in Microbiology*. Frontiers; 2019. p. 3225.
- [27]. Pillon NJ, Bilan PJ, Fink LN, Klip A. Cross-talk between skeletal muscle and immune cells: Muscle-derived mediators and metabolic implications [Internet]. Vol. 304, *American Journal of Physiology - Endocrinology and Metabolism*. American Physiological Society Bethesda, MD; 2013 [cited 2022 Apr 21]. p. 453–65. Available from: <https://journals.physiology.org/doi/full/10.1152/ajpendo.00553.2012>
- [28]. Liu Q, Yang L, Gong C, Tao G, Huang H, Liu J, et al. Effects of long-term low-dose formaldehyde exposure on global genomic hypomethylation in 16HBE cells. *Toxicol Lett* [Internet]. 2011 Sep 10 [cited 2022 Apr 17];205(3):235–40. Available from: <https://pubmed.ncbi.nlm.nih.gov/21745553/>
- [29]. Johnson W. Final Report on the Safety Assessment of Octoxynol-1,-3,-5,-6,-7,-8,-9, -10,-11,-12,-13,-16,-20,-25,-30,-33,-40,-70,-9 Carboxylic Acid, Octoxynol-20 Carboxylic Acid, Potassium Octoxynol-12 Phosphate, Sodium Octoxynol-2 Ethane Sulfonate, Sodium Octoxynol-2 [Internet]. Vol. 23, *International Journal of Toxicology*. Int J Toxicol; 2004 [cited 2022 Apr 17]. p. 59–111. Available from: <https://pubmed.ncbi.nlm.nih.gov/15162838/>
- [30]. Chen J, Wang J, Zhang J, Ly H. Advances in Development and Application of Influenza Vaccines. Vol. 12, *Frontiers in Immunology*. Frontiers Media S.A.; 2021. p. 2740.

Study of *Anemone coronaria* L. (Manisa Tulip) Species, Symbol Plant of Manisa Province, for Biomonitor and Phytoremediation Purposes

Feyza Candan ^{1*} 

¹Manisa Celal Bayar University, Science and Letters Faculty, Biology Department, Manisa, Türkiye

* fezacandan2002@yahoo.com

* Orcid No: 0000-0001-7338-5931

Received: 23 October 2022

Accepted: 2 March 2023

DOI: 10.18466/cbayarfbe.1193450

Abstract

Today, the use of plants in the cleaning (phytoremediation) of soils polluted with heavy metals and the detection of plants with accumulator properties are gaining importance day by day. However, due to the tolerance of plants against heavy metal toxicity, their ability to be bioindicators varies depending on the plant species, element type, duration of exposure to stress, and the structure of the tissue or organ exposed to stress. To date, many plants have been used in remediation, but there are few reports on the use of ornamental plants for remediation of polluted soils or as bioindicators.

In this study, based on this idea, accumulation of heavy metals of Cu, Cd, Pb, Zn were detected comparatively in 3 varieties (var. *alba*, var. *cyanea*, var. *coccinea*) of the *Anemone coronaria* species with atomic absorption spectrometry in the months of germination (March) and flowering (April) and in the soil they grow. As a result, it has been established that this species can be planted in Manisa to determine the soil pollution in the spring period, as a bioindicator, and to beautify the environment and it has been revealed that this species is a very important plant in terms of phytoremediation and as the symbol plant of Manisa.

Keywords: *Anemone coronaria*, Manisa, biomonitor, phytoremediation.

1. Introduction

Industry and technology negatively affect the ecological balance and harm nature and living things in various ways. Heavy metal pollution is one of the important harmful pollutants. Precautions should be taken to prevent living things from being damaged by heavy metal pollution in soils (1). Many methods and techniques are used to reveal the existing polluting elements in the areas to be studied for pollution. Today, the determination and monitoring of flora elements and environmental quality have become a very common and reliable method (2-4). Pollutants affecting the biotic and abiotic components of the ecosystem are accumulated by plants (sea creatures, lichens, fungi, bark, leaves, etc.) which are good indicators, in their bodies and it is reported that they provide information about environmental quality (2-5). It is known that heavy metal accumulation varies depending on the type of plant, the structure of the soil where it grows, climatic conditions, and especially the type and density of the pollutant (6, 7). Although some plant species disappear in the presence of very few pollutants, some plant species can survive at high concentrations. By examining the responses of plants to

environmental factors from morphological, anatomical, and physiological aspects, the extent of pollution can be measured much more economically than physical and chemical measurements (2, 6, 8, 9).

Studies conducted in recent years show that heavy metal pollution, which increases depending on the density of fossil fuels and industry etc, has an ecotoxicological effect. In addition to these, it is stated that it has effects such as growth problems in plants, negative effects on quality factors, decrease in yield, acute and chronic poisoning in humans and animals such as the decrease in the biological activities of microorganisms in the soil (7, 8, 10).

Heavy metals spread easily to the environment through many activities especially as nuclear and thermal power plants, factories, flue gases, domestic waste, mining operations, traffic, pesticides, excessive fertilization, etc. In addition, outside of the respiratory tract, heavy metals are transmitted to humans by consumption of foods of plant and animal origin. Therefore, it is important to understand the soil-plant-animal relationships (11, 12).

Members of the *Anemone* species, which belongs to the Ranunculaceae family, are found in the Northern Hemisphere and grow in temperate climates, and are found in high areas in the tropics (13, 14). *Anemone coronaria* L. species is of Mediterranean origin and is known as 'Manisa Tulip' or 'mountain tulip' in our country (15, 16). Morphological, anatomical, and palynological studies have been performed on *A. coronaria* species (17-22).

Members of the *A. coronaria* species are perennial plants that bloom in March and April (May) in Manisa as a harbinger of spring and are also used for decorative purposes. In this study, 3 varieties of *A. coronaria* species that spread on the Kırkağaç-Soma highway of Manisa were studied comparatively and were used as a bioindicator for the first time to monitor heavy metal accumulation. However, varieties of *Anemone coronaria* species, which attract attention with their trading feature in the Netherlands, have been proposed for the first time for phytoremediation and bioindicator-based use in this study.

This study will constitute a basis for future research on similar topics. However, it was carried out as the first stage of more comprehensive research on the same and different species planned to be carried out in other regions of Manisa.

2. Materials and Methods

3 varieties belonging to the *A. coronaria* species; Kırkağaç-Soma highway of Manisa province is a region that is packed with heavy vehicles due to the lignite coal transportation performed in the direction of İzmir and İstanbul. It is of particular importance that the Soma Thermal Power Plant is located 4-5 km from the area where the plants are collected. This locality was especially chosen because the pollution caused by the heavy traffic and the thermal power plant bears great importance for the people, plants, animals, and soil in the region.

The taxa used as examples and belonging to the Ranunculaceae family are *A. coronaria* var. *coccinea* (Hanry) Batt (red-flowered), *A. coronaria* var. *cyanea* (purple-flowered), and *A. coronaria* var. *alba* Goaty&Pens (white-flowered) (14). The plants were collected in the last week of March (24.03.2017), when they were non-flowering, and in the last week of April (24.04.2017) when they were flowering. On both dates, soil samples were taken from the same 10 different points of the area where all 3 taxa spread together and they were mixed. Soil sampling depth was determined as 0-15 cm since the tubers were very close to the surface of the soil. In March, tubers and leaves of taxa, in April, tuber, leaves, scapus, flowers, and in both months, soil samples were divided into groups to determine heavy metal (Cu, Cd, Pb, Zn) levels.

Plant specimens placed in paper envelopes were dried at 105 °C for 24 hours. 1 gr was taken from the plant samples that lost their moisture completely, acid was added in the ratio of HNO₃: HClO₄ (4:1), and they were decomposed in the CEM MARS-5 ESP 1500 PLUS microwave sample preparation device. Soil samples were passed through a 2 mm sieve and dried at 105 °C for 2-4 hours. Soil samples taken in 2 gr were decomposed in CEM Mars -5ESP 1500 PLUS microwave sample preparation device in HNO₃ : HClO₄ (3:1). All metal analyses were performed on the VARIAN 220 atomic absorption spectrometer (23).

3. Results and Discussion

When the heavy metal Cu, Cd, Pb, and Zn (ppm) accumulation levels measured in the varieties of *A. coronaria* species and in the soil samples of the area where these samples were collected are examined, the values of April were found to be higher than the values in March in both groups (except for Cu leaf and var. *cyanea* Pb leaf) (Tables 1, 2, 3).

Table 1. Heavy metal distribution by months in soil samples

Month	Cu (ppm)	Cd (ppm)	Pb (ppm)	Zn (ppm)
March	2,71	could not be measured	18,96	5,89
April	3,81	1,01	27,10	11,14

Since March is not the flowering period of the plant and the plant cannot be determined in terms of varieties, tuber and leaf were evaluated. In April, the plant was divided into varieties and spectrometric measurements were made on tubers, stems, leaves, and flowers. The results obtained with the study are given in Tables 2 and 3.

Table 2. Heavy metal measurements of March (24.03.2017) in *A. coronaria* species

Parts of plants	Cu (ppm)	Cd (ppm)	Pb (ppm)	Zn (ppm)
Tuber	1,91 ±0,42	could not be measured	7,84 ±0,96	4,86 ±1,14
Leaf	9,57 ±1,25	could not be measured	9,51 ±1,88	3,46 ±0,78

When the heavy metal distributions in March and April are evaluated in soil samples, it is seen that the amount of Cu and Pb goes up in April, and the amount of Zn increases about 3 times. However, it is noteworthy that Cd was immeasurably low in March and it increased at a value that could be measured in a spectrometer in April (Table 1).

According to the heavy metal measurements made with only leaves and tubers of *A. coronaria* species since the plant is flowerless in March, it is noteworthy that while Cu and Pb accumulation is higher in the leaf than in the tuber, Zn accumulation is higher in the tuber than in the leaf. However, the fact that Cd is too low to be measured in leaves and tubers is another important data for March. Since there were no flowers in the plant during this period, scapus could not be evaluated (Table 2).

Table 3. Heavy metal measurements of April (24.04.2017) in *A. coronaria* species varieties

<i>Anemone coronaria</i> varieties	Parts of plants	Cu (ppm)	Cd (ppm)	Pb (ppm)	Zn (ppm)
<i>Anemone coronaria</i> var. <i>alba</i>	Tuber	2,16 ±0,39	0,52 ±0,18	10,70 ±2,44	7,15 ±1,61
	Scapus	1,12 ±0,22	0,38 ±0,07	11,10 ±2,98	6,40 ±1,15
	Leaf	1,08 ±0,37	0,49 0,10	10,20 ±1,95	11,12 ±3,36
	Flower	2,24 ±0,78	0,39 ±0,14	9,80 ±3,04	6,54 ±1,47
<i>Anemone coronaria</i> var. <i>cyanea</i>	Tuber	5,43 ±0,98	0,64 ±0,21	14,70 ±4,86	9,28 ±2,11
	Scapus	0,95 ±0,34	0,40 ±0,09	8,80 ±1,96	4,32 ±0,80
	Leaf	0,98 ±0,21	0,53 ±0,11	8,80 ±2,23	11,29 ±2,86
	Flower	2,31 ±0,37	0,41 ±0,08	10,20 ±1,87	8,79 ±2,16
<i>Anemone coronaria</i> var. <i>coccinea</i>	Tuber	4,39 ±0,77	0,69 ±0,23	9,80 ±2,55	9,83 ±1,62
	Scapus	1,21 ±0,41	0,57 ±0,12	10,15 ±3,16	5,31 ±1,03
	Leaf	1,14 ±0,31	0,73 ±0,22	12,35 ±3,81	11,84 ±2,98
	Flower	2,76 ±0,63	0,53 ±0,09	9,50 ±1,11	9,22 ±1,52

When Table 2 and Table 3 are compared, although it will be noticed that there is a tendency towards an increase between two months in general, it is interesting that the amount of Cu measured in the leaf of the *A. coronaria* plant in March is 9,57 ppm, it shows a significant decrease in April in var. *coccinea* (1.18 ppm) > var. *alba* (1.08) > var. *cyanea* (0.98 ppm) and while other heavy metals increased in the other parts, Pb decreased in April in var. *cyanea* (8.80 ppm) compared to March (9.51 ppm) in the leaf. It can be indicated that the reason for this is that heavy metals are very effective and accumulate excessively in March when the leaf is in the sprouted state. Pb, on the other hand, can be stated to be less effective on the leaf in var. *cyanea* taxon. (Tables 2, 3). In the April evaluations, *A. coronaria* species could be studied comparatively with its 3 varieties: var. *alba*, var. *cyanea* and var. *coccinea*.

If all three taxa of tuber are compared, var. *cyanea* has distinctively higher values for Cu and Pb than the other 2 taxa. However, when var. *alba* (except for Pb value) is evaluated, it contains the lowest amounts of heavy metals in tuber (Table 3).

var. *cyanea*-tuber (Cu) > var. *coccinea* (Cu) > var. *alba* (Cu)

var. *cyanea*-tuber (Pb) > var. *alba* (Pb) > var. *coccinea* (Pb)

var. *coccinea*-tuber (Cd, Zn) > var. *cyanea* (Cd, Zn) > var. *alba* (Cd, Zn)

When scapus is evaluated in general, var. *coccinea* has the highest values in terms of Cu and Cd and var. *alba* has the highest values in terms of Pb and Zn. In addition, var. *cyanea* contains the lowest values for all heavy metals (Table 3).

var. *coccinea*-scapus (Cu, Cd) > var. *alba* (Cu, Cd) > var. *cyanea* (Cu, Cd)

var. *alba*-scapus (Pb, Zn) > var. *coccinea* (Pb, Zn) > var. *cyanea* (Pb, Zn)

When a comparison is made in terms of leaves, var. *coccinea* taxon was observed to accumulate in higher amounts than all other taxa in terms of all heavy metals. Also, when var. *alba* is compared to var. *cyanea*, it will be seen that Cu and Pb are present in higher amounts in var. *alba* while Cd and Zn are in higher amounts in var. *cyanea* (Table 3).

var. *coccinea*-leaf (Cu, Pb) > var. *alba* (Cu, Pb) > var. *cyanea* (Cu, Pb)

var. *coccinea*-leaf (Cd, Zn) > var. *cyanea* (Cd, Zn) var. *alba* (Cd, Zn)

When flowers are evaluated, in terms of Cu, Cd, and Zn var. *coccinea* accumulated in the highest amount, which was followed by var. *cyanea* and var. *alba* accumulated in the lowest amount. In terms of Pb, it is seen that var. *cyanea* flower contains the highest amount of heavy metal (Table 3).

var. *coccinea*-flower (Cu, Cd, Zn) > var. *cyanea* (Cu, Cd, Zn) > var. *alba* (Cu, Cd, Zn)

var. *cyanea*-flower (Pb) > var. *alba* (Pb) > var. *coccinea* (Pb)

4. Discussion

Nerium indicum Mill, *Phragmites australis* Cav., *Zephyranthes candida* (Lindl.) Herb., *Cynodon dactylon* (L.) Pers., *Alternanthera philoxeroides* (Mart.) Griseb., *Chenopodium rubrum* L., *Aster subulatus* Michx, and *Brassica chinensis* L. species were used in a study conducted in polluted areas to reveal plants that may be suitable for bioindicator and/or phytoremediation studies. Given the fact that they are from different families, successful results have been obtained (24). The *A. coronaria* species used in our study is a plant suitable for being a phytoremediation and bioindicator plant, representing the Ranunculaceae family, with its capacity to absorb Cu, Cd, Pb, Zn heavy metals from the soil according to the months and organs.

The study conducted on industrial pollution and urban pollution using *Acer negundo* L. and *Platanus orientalis* L. in Antakya and ours are similar studies. As a result of the research conducted in Antakya, it was seen that the plants with high Cu and Al content were located on the city street, while the plants with high Cd, Pb, and Zn content were found to be on the industrially developed side of the city (12). Since the location chosen in our study is on a very busy road and is close to the Soma Thermal Power Plant, it also has the characteristics of the two locations selected in the study conducted in Antakya. However, Cu, Cd, Pb, and Zn heavy metals examined in our study were grouped among themselves according to plant parts, soil and months, and a detailed study specific to the spring season of Manisa province that could be repeated every year was created.

A study was conducted on the root length inhibitory effect of Cu, Cd, Pb, Zn, and Fe heavy metals, photosynthetic pigment content, and the effect of metal accumulation in roots and sprouts in *Sinapis alba* L. species. The study revealed that all heavy metals except Fe accumulated more in plant roots than in plant sprouts (25). Within the scope of this study, if the heavy metal accumulations in *A. coronaria* tubers and other parts are examined comparatively (Table 3), it is concluded that there was a remarkable amount of heavy metal accumulation in other parts of the plant as well, prominently in tubers. These results clearly show that the plant is an accumulator with every organ and is suitable for use in phytoremediation.

Cu, Cd, Pb, Zn, Ni, and Fe heavy metal levels on *Rosmarinus officinalis* L. samples and soils taken from various locations in Jordan were evaluated by atomic spectrometry. The plant was examined in three groups as leaves, flowers, and stems. Spinach leaves and ryegrass were used as reference materials and as a result, a high level of remediation was achieved (26). The plant *A. coronaria*, which we recommend as a phytoremediation and biomonitor plant used in this study, can also be used as a reference plant for other plants grown in Manisa in the spring season.

Salix phylicifolia L., *Salix borealis* Fr., *Carex rostrata* Stokes, *Eriophorum angustifolium* Roth, and *Phragmites australis* Cav. taxa were analyzed for the collection and transport of Cu, Cd, Pb, Zn, and As heavy metals from the soil. Among these species, only *Salix* species with Cd and Zn accumulator in their sprouts and *Eriophorum angustifolium* with Pb accumulator were found to be toxic species for animal grazing (27). The *A. coronaria* species suggested as a bioindicator in this study is a plant suitable to be used to easily determine toxic species in Manisa, where the lands begin to green up in the spring period especially to determine toxic species for animal grazing, as given in the study above, in accordance with the comparison at the organ level.

According to a study on the transfer of some heavy metals from soil to vegetables (transfer factor) using 20 different vegetables in China in 2007, the rate of transfer from soil to plant was found in the direction of Cd > Zn > Cu > Pb > Hg (28). In *A. coronaria* taxa, the transfer rate of heavy metals varies. In this regard, interpretation can be performed, and the transfer direction of heavy metals in the organs in taxa can be put in order as follows (Table 3): var. *coccinea*, Cu > Cd > Zn > Pb, var. *cyanea*, Pb > Cu > Cd=Zn, var. *alba* Pb > Cu > Zn > Cd. As can be seen, when compared with the study of Zheng et al. (2007), *A. coronaria* taxa did not comply with this study and therefore, it is a study that can be evaluated for different purposes.

Harvey (1971) stated that there are anthocyan-type substances in *A. coronaria* species, which are cyanidin, delphinidin, and pelargonidin (29). In this case, pelargonidin is found in red, delphinidin in blue, and cyanidin in the pink-purple variety. It can be indicated that Cu, Cd, and Zn accumulation in the flower exists in var. *coccinea*>var. *cyanea*>var. *alba* direction in the flower due to the effect of anthocyan-type substances found in *A. coronaria* taxa. It can be stated that it is in the var. *alba* direction. However, it is seen that the effect of anthocyanin substances on Pb accumulation is different from that of other heavy metals (Table 3).

In a review study on the toxic effects of Cu, Cd, Pb, and Zn heavy metals on vascular plants, it has been revealed that Zn is the least toxic heavy metal. However, no amount has been given in the literature in terms of toxic concentration for Cu, Cd, Pb, and Zn heavy metals in the soil (30). For this reason, although it is avoided to make any comments about the toxic concentration of our study area, we think that these evaluations should be updated with the increase in environmental pollution resulting from the developments such as today's increasing population, developing technology, and factories built, etc.

Table 4. Soma Station air quality index

Sample collecting days	PM ₁₀ µg/m ³	SO ₂ µg/m ³	CO µg/m ³	NO ₂ µg/m ³	NOX µg/m ³
24.03.2017	118,75	77,75	352,90	-	-
24.04.2017	48,02	13,47	10,69	13,27	32,56

It is a known fact that the most important sources of pollution in Soma-Kırkağaç are the emissions from Soma Thermal Power Plant, heating activities in residences, construction, and traffic based on heavy coal transportation. There are 2 stations in Manisa, one in the center and the other in Soma that measure air quality and collect daily data. The air quality data of the Ministry of Environment, Urbanization and Climate Change Soma Station for the study location and the days the samples were collected are given below (31).

In addition to PM₁₀ (particulate matter) pollution, SO₂ (sulfur dioxide) values in Soma reach levels that threaten public health, especially in winter, and they always create pollution (32). As it is understood from this research, it is a known fact that the air pollution in Soma district is intense and Kırkağaç district, which is a district 10 km away, is adversely affected by the air pollution caused by the Soma Thermal Power Plant. However, as can be seen in Table 4, it is clear that the differences between the pollution levels in March and April in Soma district are high. In addition, although there are varying data on air pollution in Table 4, there is no information on heavy metals with carcinogenic effects, which pass through to the soil and from there to the plants, and thus to humans, with pollution-related emissions from traffic, etc. For this reason, *A. coronaria* species is a plant that should be brought to Manisa from a biological point of view due to its positive results in terms of its usability in phytoremediation due to its locality, perennial nature, and the fact that it is a bioindicator plant. As air quality indices are created, monthly herbal and soil-specific heavy metal indices can be created and shared with the public thanks to selected bioindicator plants.

5. Conclusion

The increasing traffic density of the Soma-Kırkağaç highway, coal activities, the development of residential areas, and the thermal power plant are the factors that increase pollution in the region. In this study, the selected plant was especially chosen because it is easy to understand in a short time whether it is easily affected by environmental pollution due to its short ground surface life span, its relationship with the soil, the relationship between soil pollution and the intake of this by the plant. However, in the study conducted, it is seen that there is a remarkable difference in terms of pollution between the spring period in March and April. Considering the increasing population, traffic, and the activity of the Soma Thermal Power Plant, it can be stated that this will change every year and that comparisons can be made easily with the bioindicator plant for these months. In addition, by taking into account this issue, local governments should take the necessary precautions.

This study, which was conducted to examine self-sown plants in nature and those also used as ornaments in the cleaning of environmental pollution, will constitute an important basis for the three-purpose-effective use of *A. coronaria* species for Manisa, which has economic and cultural importance, by demonstrating its ability to beautify the environment while being used for phytoremediation and biomonitor purposes.

Presentation of air quality indexes of regions and heavy metal accumulation data of selected seasonal plants with bioindicator properties on a half-monthly/monthly basis in addition to meteorological data in weather bulletins in mass media in big cities such as Manisa will enable

working together in the solution of air and environmental pollution, in terms of right orientations regarding healthy nutrition and allow for healthy solutions to be put forward at the outset.

Funding

The author has not received any financial support for the research, authorship, or publication of this study.

Author's Contributions

FeYZa Candan: Drafted and wrote the manuscript, performed the experiment and result analysis.

Ethics

There are no ethical issues after the publication of this manuscript.

References

- [1] Yaçın, MG. 2007. Toprak Örneklerinde Ağır Metal Birikimlerinin Analizi ve Değerlendirilmesinde Kullanılan Bazı Teknikler. *Toksikoloji Dergisi*; Sayı:5, 39-47.
- [2] Candan, F. 2020. Plant Phenology and An Assessment of the Effects Regarding Heavy Metals, Nanoparticles, and Nanotubes on Plant Development: Runner Bean, Artichoke and Chickpea Seedlings]. In: Oliveira MT, Candan F, Fernandes-Silva A. Eds. *Plant Communities and Their Environment*. UK: InTech – Open Press, 3-25.
- [3] Banfalvi, G. 2011. *Cellular Effects of Heavy Metals*. Dordrecht: Springer, p.348.
- [4] Türk Çulha, S, Koçbaş, F, Gündoğdu, A, Baki, B, Çulha, M, Topçuoğlu, S. 2011. The seasonal distribution of heavy metals in Mussel sample from Yalova in the Marmara Sea, 2008–2009. *Environmental Monitoring and Assessment*; Vol:183, 525–529.
- [5] Gündoğdu, A, Türk Çulha S, Koçbaş, F. 2020.Trace Elements Concentrations and Human Health Risk Evaluation for Four Common Fish Species in Sinop Coasts (Black Sea). *Turkish Journal of Agriculture-Food Science and Technology*; Vol:8, No:9.
- [6] Athar, R, Ahmad, M. 2002. Heavy metal toxicity: effect on plant growth and metal uptake by wheat, and on free living azotobacter]. *Water Air Soil Pollution*. 2002; 138:165–180.
- [7].Batır, MB, Candan, F, Büyük, İ, Aras, S. 2015. The determination of physiological and DNA changes in seedlings of maize (*Zea mays* L.) seeds exposed to the waters of the Gediz River and copper heavy metal stress. *Environmental Monitoring and Assessment*; 187(4):169.
- [8] Batır, MB, Candan, F, Büyük, İ. 2016. Determination of the DNA changes in the artichoke seedlings (*Cynara scolymus* L.) subjected to lead and copper stresses. *Plant Soil Environment*; 62, No.3, 143-149.
- [9] Zengin, FK, Munzuroğlu, O. 2004. Effect of lead and copper (Cu) on the growth of root, shoot and leaf of bean (*Phaseolus vulgaris* L.) seedlings. *Journal of Science*; 17:1-10.
- [10] Çobanoğlu, O. 2019. Mavi Ladin (*Picea pungens* Engelm) İbrelere Yakın Geçmişteki Ağır Metal Birikiminde Biyomonitör Olarak Kullanılabilir Olanakları. Kastamonu Üniversitesi, Fen Bilimleri Enstitüsü.

- [11] Yıldırım, C, Karavin, N, Cansaran, A. 2012. Amasya İli Şehir Merkezinde Bulunan *Elaeagnus angustifolia* L. ve *Pinus brutia* Ten. Türlerinde Bazı Ağır Metallerin İçeriklerinin Belirlenmesi. *Biyolojik Bilimleri Araştırma Dergisi*; 5 (2): 7-11.
- [12] Doğanlar, ZB, Atmaca, M. 2011. Influence of Airborne Pollution on Cd, Zn, Pb, Cu, and Al Accumulation and Physiological Parameters of Plant Leaves in Antakya (Turkey). *Water, Air, & Soil Pollution*; Vol:214; 509-523.
- [13] Good, R. 1964. The Geography of the Flowering Plants, XIV-518, Longmans Green and Co. Ltd, London.
- [14] Davis, P.H. 1965. Flora of Turkey and East Aegean Islands. Univ Press Edinburgh, U.K, Vol. I.
- [15] Demiriz, H. 1965. Türkiye Florası'ndan Örnekler, *Anemone coronaria* L., *Türk Biyoloji Dergisi İlavesi*, 1/Acta Biol. Turc. Suppl.; 1/14(2), İstanbul.
- [16] Seçmen, Ö, Gemici, Y, Görk, G, Bekat, L, Leblebici, E. 1995. Tohumlu Bitkiler Sistematığı. Ege Üniv. Fen Fak. Kitaplar Serisi, No:116, 168-171, İzmir.
- [17] Darlington, CD, Wylie, AP. 1961. Chromosome Atlas of Flowering Plantae. 519, George Allen and Unwin. Ltd, London.
- [18] Zohary, M. 1966. Flora Palaestina The Israel Academy of Sciences and Humanities. 1:364, Jerusalem.
- [19] Karaca, T, Seçmen, Y. 1970. İzmir yöresinde Manisa Lalesi (*Anemone coronaria* L.) ile ilgili araştırmalar. *Ege Üniversitesi Ziraat Fakültesi Dergisi*; 7: 3-23.
- [20] Candan, F. 2001. *Anemone coronaria* L. Türü Üzerinde Biyolojik Bir Araştırma. Yüksek Lisans Tezi. Manisa Celal Bayar Üniversitesi Fen Bilimleri Enstitüsü.
- [21] Candan, F, Şık, L. 2006. Comparative Morphological Research on *Anemone blanda* Schott & Kotschy and *Anemone coronaria* var. *coccinea* (Jord.) Burn occurring in west Anatolia, Turkey. *JFS, E.U.F.F.* (Ege Üniv. Fen Fak.); Vol. 29, 1-12.
- [22] Candan, F, Şık, L. 2006. Comparative Anatomical Research on *Anemone blanda* Schott & Kotschy and *Anemone coronaria* var. *coccinea* (Jord.) Burn occurring in west Anatolia, Turkey. *JFS, E.U.F.F.* (Ege Üniv. Fen Fak.); Vol. 29, 99-112.
- [23] ASTM. 1985. Preparation ve Biological Samples for inorganic chemical analyses. 1. Annual Book of ASTM Standards. 740-747.
- [24] Yuan, Y, Yu, S, Bañuelos, G. 2016. Accumulation of Cr, Cd, Pb, Cu, and Zn by plants in tanning sludge storage sites: opportunities for contamination bioindication and phytoremediation. *Environ Sci Pollut Res.*; 23, 22477-22487.
- [25] Fargašová, A. 2001. Phytotoxic Effects of Cd, Zn, Pb, Cu and Fe on *Sinapis alba* L. Seedlings and their Accumulation in Roots and Shoots. *Biologia Plantarum*; 44, 471-473.
- [26] El-Rjoob, AWO, Massadeh, AM, Omari, MN. 2008. Evaluation of Pb, Cu, Zn, Cd, Ni and Fe levels in *Rosmarinus officinalis* labiatae (Rosemary) medicinal plant and soils in selected zones in Jordan. *Environ Monit Assess*; 140, 61-68.
- [27] Stoltz, E, Greger, M. 2002. Accumulation properties of As, Cd, Cu, Pb and Zn by four wetland plant species growing on submerged mine tailings. *Environmental and Experimental Botany*; Vol. 47, Issue 3, 271-280.
- [28] Zheng, N, Wang, Q, Zheng, D. 2007. Health risk of Hg, Pb, Cd, Zn, and Cu to the inhabitants around Huludao Zinc Plant in China via consumption of vegetables. *Science of The Total Environment*; Vol. 383, Issues 1-3, 81-89.
- [29] Harvey, DM. 1971. Phenotypic Variation in Flower Colour within the *Anemone coronaria* Cultivars. *Annals of Botany*; Vol. 35, Issue 1, January, 1-8.
- [30] Pålsson, AMB. 1989. Toxicity of heavy metals (Zn, Cu, Cd, Pb) to vascular plants. *Water Air Soil Pollution*; 47, 287-319.
- [31] www.csb.gov.tr (accessed at 04.07.2022).

Boric Acid Treatment Strengthens the Cytotoxic Effect of Sorafenib on Triple Negative Breast Cancer Cell Lines

Erkan Kahraman^{1*} , Erdem Göker² 

¹Ege University, Atatürk Health Care Vocational School, Bornova, İzmir, Türkiye

²Ege University, Faculty of Medicine Department of Internal Medicine, Bornova, İzmir, Türkiye

*erkan.kahraman@ege.edu.tr

* Orcid No: 0000-0003-0051-416X

Received: 8 November 2022

Accepted: 12 June 2023

DOI: 10.18466/cbayarfbe.1201068

Abstract

In recent years, it has been demonstrated that combinational therapies have shown promising results in the treatment of triple negative breast cancer. However, the effect of the sequential combination of sorafenib with boric acid on cell viability in triple negative breast cancer cell lines is unknown. Thus, the present study aims to investigate the effects of sequential treatment of boric acid and sorafenib on cell viability in triple negative breast cancer cell lines. MDA-MB-231 cells were used in our study. Sorafenib was treated to the cells at a dose range of 0.5-16 μ M, and boric acid at 1-160mM. Changes in cell viability were determined using by MTT analysis at 24,48 and 72 hours. Cell viability decreased statistically significantly at 4 μ M and above doses of sorafenib, and 5mM and above doses of boric acid ($p < 0.05$). IC50 values of boric acid were calculated as 34mM, 26mM and 1mM at hours 24,48 and 72, respectively. Alone treatment of sorafenib at 8 μ M and 16 μ M doses reduced cell viability up to 80% and 61%, respectively. On the other hand, 15mM boric acid treatment followed by sorafenib treatment at 8 μ M and 16 μ M doses decreased cell viability up to 64% and 44%, respectively ($p < 0.05$). Also, it was observed that boric acid treatment followed by sorafenib treatment caused MDA-MB-231 cells to diverge from their ancestral morphology, resulting in an unhealthier appearance. Our results suggest that a sequential treatment of boric acid followed by sorafenib strengthens the cytotoxic effect of sorafenib on triple negative breast cancer cell lines.

Keywords: Boric Acid, Boron, Sorafenib, Triple negative breast cancer

1. Introduction

Breast cancer ranks as the first most common cancer in worldwide [1]. The disease can occur in different sites of the breast, including the lobules, canals and connective tissues. Breast cancer exhibits various physiological characteristics specific to the tissue in which it originates, and the different clinical outcomes that can occur have led to the creation of various subgroups [2]. Triple-negative breast cancer (TNBC) is more aggressive and is more prone to recurrence than other subtypes [3]. Among the breast cancer subtypes, TNBC cancer has limited therapeutic options due to the lack of well-established molecular targets for targeted therapy. Accordingly, the development of new treatment strategies is of critical importance [4]. While classic chemotherapeutic approaches are still valid, studies have identified various combination regimens as potentially effective strategies [5].

Sorafenib, an orally administered multi-kinase inhibitor, has been used effectively for the treatment of unresectable hepatocellular carcinoma (HCC) since 2008 [6]. Sorafenib is able to block cellular proliferation by inhibiting the activity of kinases involved in the extracellular signal-regulated kinase Raf-1, B-Raf and Ras/Raf/MEK/ERK signaling pathway, and also suppresses angiogenesis by inhibiting the hepatocyte factor receptor (c-Kit), Fmes-like tyrosine kinase (FLT-3), VEGFR-2 and VEGFR-3, PDGFR- β and other kinases [7]. Since its initial introduction into practice, it has been included as part of effective therapeutic approaches to the treatment of HCC [8], and has also been reported to inhibit the pathogenesis of breast cancer [9]. The growth-inhibiting effects and favorable toxicity profile of sorafenib in preclinical models have revealed potential benefits in breast cancer [10].

Boron is placed in group 13 of the periodic table, and it is only non-metal element in this group. It is not present

in its elemental form in nature. Boron is found in nature as a component of boric acid (BA), kernite, borax, ulexite and colemanite in nature [11]. In the human body, inorganic borate compounds are found in the BA form.[12]. It has been suggested that BA can play a beneficial role in anti-cancer processes in specific cancer types, and has shown promise in this regard [13]. Epidemiological studies have also shown that the addition of BA to the diet decreases the risk of the development of various cancers, including those of the prostate and the lung [14]. A number of *in vitro* studies have also reported its possible anti-cancer properties in various cancer cell lines, and it has been demonstrated that BA induces apoptosis and suppresses cellular proliferation in breast cancer cells [15-17].

The present study, performed in light of the above data, investigates to effect of sequential treatment of the FDA-approved drug sorafenib and BA, which is reported to possess anti-cancer properties, on cell viability in TNBC cells lines.

2. Materials and Methods

2.1. Cell Culture

All procedures in this study were performed *in vitro* in commercially purchased human Triple Negative (ER-/PR-/HER-) MDA-MB-231 cell lines. TNBC cell lines were cultured in MEM medium (Capricorn, Cat. No:MEM-A) supplemented with 10% Fetal Bovine Serum (Biol. Ind. Cat. No:01-121-1A), 100 µg/ml Penicillin / Streptomycin (Biol. Ind. Cat. No:03-031-1B), 1% MEM non-essential amino acid solution (Biol. Ind. Cat. No:01-340-1B) at 37 °C with 5% CO₂ in a humidified atmosphere.

2.2. Cell viability assay

A MTT assay was carried out for the determination of cell viability of TNBC cells. Briefly, cells were seeded to 96 well plates at 5000 cell / well concentrations and incubated for 24 hours. After the incubation period, the cell culture media were discarded. Sorafenib (0.5, 1, 2, 4, 8, 16 µM) and BA (1, 5, 10, 15, 20, 30, 40, 80, 160 mM) contained fresh media was treated to cells. End of the treatment time, 15µl MTT (5mg/ml, Sigma, Cat. No: M5655) solution was added to each well and incubated 4 hours. Mediums were removed and 100µl DMSO (Merck, Cat. No:116743) added to wells. Plates were read at 570nm wavelength using by a microplate reader. Viability of TNBC cells were calculated according to the formula below.

Viability (%) = (OD, treated group- blank)-(OD, untreated group- blank)x100

2.3. Sequential treatment of BA and sorafenib

For sequential treatment, BA was used at 15 mM dose, and sorafenib 8 and 16 mM doses. Cells were seeded to 96 well plates at 5000 cells/well concentration and cultured for 24 hours. Cell culture mediums were changed with fresh medium containing BA at 15mM dose. After 24 hours, mediums were replaced with fresh medium containing sorafenib at 8 and 16 µM doses and cells were incubated for 72 hours. Effect of sequential treatment on cell viability were determined using by a MTT analysis. Also, cellular morphological changes were examined under light microscope.

2.4. Statistical analysis

All statistical analyses were performed using by Graph Pad Prism 8.4 statistical software. One-way ANOVA was used for comparison of multiple groups and post hoc Tukey's test was used between groups. To determine the significance level of the difference between the means of the two groups, independent sample t-test was performed. Dose response inhibition analysis was carried out for calculation of IC₅₀ values. All assays were made at least three times with three replicates. A p-value of <0.05 was taken as statistically significant.

3. Results

3.1. Effect of Sorafenib on Cell Viability

The study investigated the effects of sorafenib up to a dose of 16 µM on the viability of cells at 24,48 and 72 hours after treatment, and found it to have no effect on cell viability in doses up to 2 µM, while doses of 4 µM or greater significantly reduced cell viability. Also, it was founded that sorafenib reduced the viability of cells in a dose- and time-dependent manner at other doses and time points. (Figure 1). According to the results of cell viability analysis, sorafenib doses of 8 and 16 µM were determined as appropriate for use in sequential treatment.

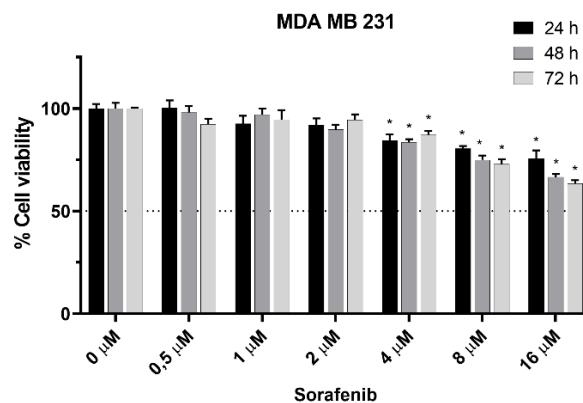


Figure 1. Effect of sorafenib on cell viability. Error bars shows ± SD (n=3). * Asterisk shows p<0.05.

3.2. Effect of BA on Cell Viability

The effects of BA up to doses of 160 μM were investigated on the viability of cells at 24, 48 and 72 hours, and it was observed that BA at doses of 5 mM and greater significantly reduced cell viability (Figure 2). The IC₅₀ values of BA at 24, 48 and 72 hours were calculated as 34, 26 and 15 mM, respectively (Figure 3). A boric dose of 15 mM was determined for use in sequential treatment, and was found to reduce the viability of cells in a dose and time dependent manner.

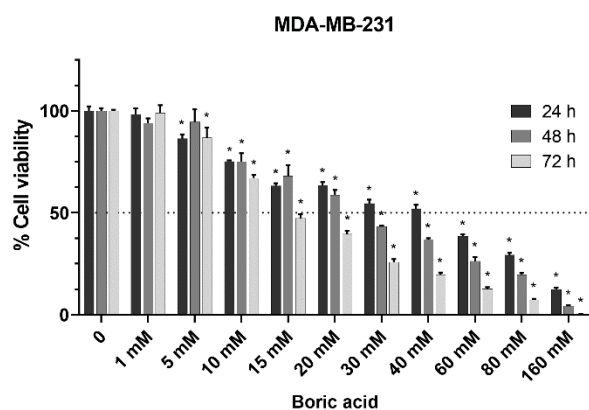


Figure 2. Effect of BA on cell viability. Error bars shows \pm SD (n=3). * Asterisk shows $p < 0.05$.

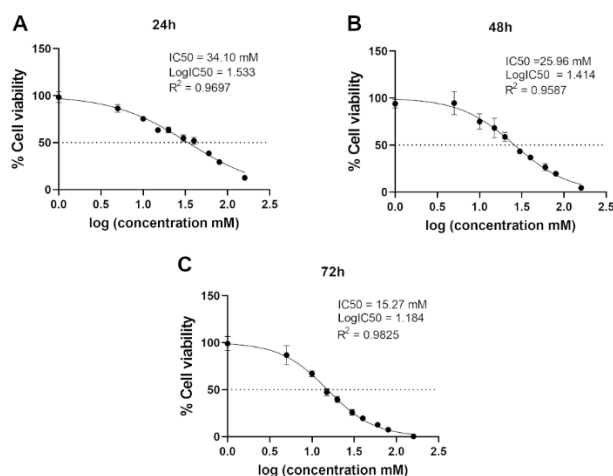


Figure 3. IC₅₀ values of BA. Changes in viability were determined by MTT analysis. IC₅₀ values of BA were calculated at 24 (A), 48 (B) and 72 (C) hours. Error bars shows \pm SD (n=3). * Asterisk shows $p < 0.05$.

3.3. Effect of sequential treatment of BA and sorafenib on cell viability.

The treatment of BA alone reduced cell viability by 88%, and the treatment of sorafenib alone at doses of 8 μM and 16 μM reduced cell viability by 80% and 61%, respectively.

The treatment of sorafenib at doses of 8 μM and 16 μM after treatment with BA for 24 hours reduced cell viability by 64% and 44%, respectively. The reduction in cell viability following both sequential treatment was statistically significant when compared to the single treatment of either BA or sorafenib ($p < 0.05$) (Figure 4). On the other hand, no changes were observed in cell morphology after the BA treatment at the specified doses. In cell lines treated only with sorafenib, the cellular morphology changed, cells lost their cell-to-cell connections, the cytoplasm decreased, and the cell morphology transformed from the ancestral morphology and took on an unhealthy appearance. This effect was even more prominent in combinational doses (Figure 5). In conclusion, sorafenib treatment for 72 hours following BA treatment for 24 hours was noted to strengthen the anti-cancer effect of sorafenib in TNBC cell lines.

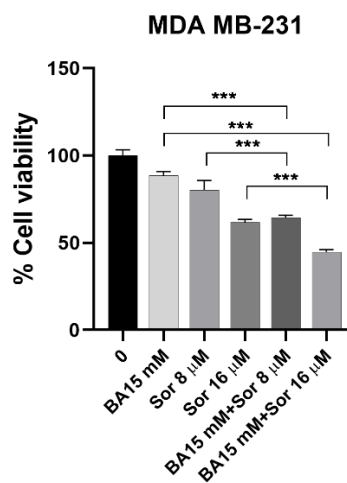


Figure 4. Effect of sequential treatment of BA and sorafenib on cell viability. Following 24 hours BA treatment, sorafenib was treated to cells for 72 hours. Error bars shows \pm SD (n=3). * Asterisk shows $p < 0.05$.

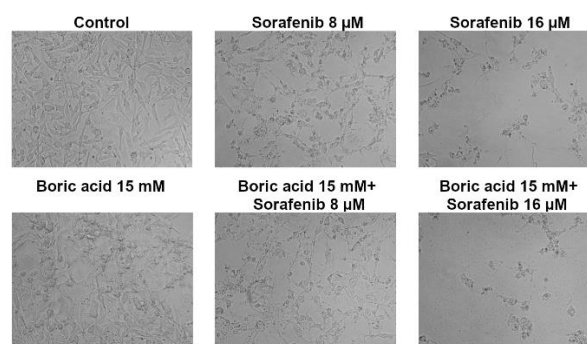


Figure 5. Effect of sequential treatment of BA and sorafenib on cellular morphology. Following 24 hours BA treatment, sorafenib was treated to MDA-MB-231 cell lines for 72 hours. Cellular morphological changes were examined under light microscope.

4. Discussion

TNBC is a heterogeneous malignancy that exhibits distinct characteristics in terms of its natural course and response to therapy. Patients do not benefit from hormonal therapies due to the loss of such target receptors as the ER, PR and HER-2. For this reason, chemotherapy still remains the optimum treatment [18], despite the potential poor response, increased toxicity and drug resistance, which may lead to poor outcomes [19]. Although surgery and chemotherapy, alone or in combination, may seem to be the sole treatment modalities available, recent studies have reported promising effects of combination therapies in the treatment of TNBC, suggesting them as a good therapeutic option [20]. The efficacy of sorafenib has been investigated when used in combination with other drugs for the treatment of breast cancer [10].

Sorafenib has been investigated in numerous clinical trials involving patients with breast cancer, and has often been reported to be well-tolerated in patients with metastatic disease and in those with earlier-stage breast cancer [21]. The possible mechanisms underlying its anti-cancer properties have been linked to its inhibition of tumor progression and growth, inhibition of angiogenesis and metastasis. However, aside from in clinical trials, sorafenib is not currently part of routine treatment approaches to breast cancer [22]

Sorafenib has been shown to reduce cell viability at doses of 1 μM in Mahlavu cell lines [15], at doses of 4 μM in HepG2 and HuH-7 cell lines [23], at doses of 1 μM in LNCAP cell lines, and at doses of 0.5 μM and greater in PC3 cell lines [24]. Cytotoxic effects have been shown to occur at doses of 10 μM and greater in ER positive / PR positive breast cancer cell lines [25]. In the present study, sorafenib reduced cell viability in TNBC cell lines, at doses of 4 μM and greater at 24, 48 and 72 hours. Consequently, the present study found that sorafenib reduced the viability of TNBC cells in a dose and time dependent manner.

There have been many experimental studies reporting the anti-cancer properties of BA and its promise as a cancer treatment. Studies of cultured cancer cells have reported an IC50 value at 24 hours of 30 mM in Mahlavu cell lines, 20 mM in HuH-7 cell lines [15], 17 mM in U87-MG cell lines [26] and 10.7 mM in DU-145 cell lines [27]. In the present study, the IC50 value at 24 hours was 34 mM in TNBC cells, while the IC50 values at 48 and 72 hours were 26 mM and 15 mM, respectively. It was observed, however, that the dose-reducing cell viability was 5 mM and greater, it was determined that the dose that reducing cell viability was 5 mM and greater. Consequently, it was concluded that BA reduces the viability of TNBC cell lines in a dose and time dependent manner.

Although single-agent treatment regimens have shown favorable results on cell morphology and in preclinical models, clinical studies have failed to produce promising results in aggressive TNBC due to its heterogeneous nature and the development of drug resistance [28]. For this reason, combined drug therapies are gaining popularity and have proven to be effective in clinical trials in improving complete pathologic response (PCR), progression-free survival (PFS) and overall survival (OS). Almost 80% of the currently ongoing clinical trials investigating new therapeutic strategies for the treatment of TNBC are exploring the efficacy of various drug combinations [5]. Sorafenib is one such drug being investigated, for use in combination with such agents as paclitaxel and capecitabine, all of which have produced promising results in the treatment of TNBC [29, 30]. The present study demonstrates that sorafenib used in combination with BA significantly reduces cell viability when compared to the treatment of sorafenib alone or the treatment of BA alone. The study found that the combined regimen also affects cell morphology more profoundly than the single treatment of the agents, resulting in an unhealthy appearance in the cells.

5. Conclusion

The sequential treatment of BA and sorafenib as a combinational regimen strengthens the anti-cancer efficacy of sorafenib in TNBC cell lines. The elucidation of the molecular mechanisms underlying the effect of sorafenib and BA combination would aid in the establishment of the optimal doses and sequential administration of each agent, and may provide to significant strides in the management of this difficult-to-treat condition.

Acknowledgement

This work was supported by AKOD (Academic Oncology Association from Türkiye)

Author's Contributions

Erkan Kahraman:
Erdem Göker:

Ethics

There are no ethical issues after the publication of this manuscript.

References

- [1]. Bray F, Ferlay J, Soerjomataram I, et al. 2018. Global cancer statistics 2018: GLOBOCAN estimates of incidence and mortality worldwide for 36 cancers in 185 countries. *CA: a cancer journal for clinicians*; 68: 394-424.
- [2]. Weigelt B, Geyer FC, Reis-Filho JS. 2010. Histological types of breast cancer: How special are they? *Molecular Oncology*; 4: 192-208.
- [3]. Garrido-Castro AC, Lin NU, Polyak K. 2019. Insights into Molecular Classifications of Triple-Negative Breast Cancer: Improving Patient Selection for Treatment Heterogeneity of Triple-Negative Breast Cancer. *Cancer discovery*; 9: 176-198.
- [4]. Yin L, Duan J-J, Bian X-W, et al. 2020. Triple-negative breast cancer molecular subtyping and treatment progress. *Breast Cancer Research*; 22: 61.
- [5]. Chalakur-Ramireddy Naveen KR, Pakala Suresh B. 2018. Combined drug therapeutic strategies for the effective treatment of Triple Negative Breast Cancer. *Bioscience Reports*; 38: BSR20171357.
- [6]. Llovet JM, Ricci S, Mazzaferro V, et al. 2008. Sorafenib in advanced hepatocellular carcinoma. *N Engl J Med*; 359: 378-390.
- [7]. Wilhelm SM, Carter C, Tang L, et al. 2004. BAY 43-9006 exhibits broad spectrum oral antitumor activity and targets the RAF/MEK/ERK pathway and receptor tyrosine kinases involved in tumor progression and angiogenesis. *Cancer Res*; 64: 7099-7109.
- [8]. Marisi G, Cucchetti A, Ulivi P, et al. 2018. Ten years of sorafenib in hepatocellular carcinoma: Are there any predictive and/or prognostic markers? *World J Gastroenterol*; 24: 4152-4163.
- [9]. Moreno-Aspitia A. 2010. Clinical overview of sorafenib in breast cancer. *Future Oncology*; 6: 655-663.
- [10]. Bianchi G, Loibl S, Zamagni C, et al. 2009. Phase II multicenter, uncontrolled trial of sorafenib in patients with metastatic breast cancer. *Anti-Cancer Drugs*; 20: 616-624.
- [11]. Kot FS. 2009. Boron sources, speciation and its potential impact on health. *Reviews in Environmental Science and Bio/Technology*; 8: 3-28.
- [12]. Smallwood C. International Programme on Chemical Safety Environmental Health Criteria 204 Boron; WHO: Geneva, 1998;
- [13]. Barranco W, Eckhart C. 2006. Cellular changes in boric acid-treated DU-145 prostate cancer cells. *British journal of cancer*; 94: 884-890.
- [14]. Cui Y, Winton MI, Zhang Z-F, et al. 2004. Dietary boron intake and prostate cancer risk. *Oncol Rep*; 11: 887-892.
- [15]. Kahraman E, Göker E. 2022. Boric acid exert anti-cancer effect in poorly differentiated hepatocellular carcinoma cells via inhibition of AKT signaling pathway. *Journal of Trace Elements in Medicine and Biology*; 73: 127043.
- [16]. Kahraman E, Gürhan İD, Korkmaz M. 2013. Investigation of possible genotoxic and cytotoxic effects of differential boron compounds in ccl 62 (hela contaminant) human amniotic epithelial cell line. *Medicine Science*; 2: 454-468.
- [17]. Meacham SL, Hall C, Tharkar S, et al. Boric acid induces apoptosis in some breast cancer cell lines. In.: Wiley Online Library; 2006.
- [18]. Lebert JM, Lester R, Powell E, et al. 2018. Advances in the Systemic Treatment of Triple-Negative Breast Cancer. *Current Oncology*; 25: 142-150.
- [19]. Nedeljković M, Damjanović A. 2019. Mechanisms of Chemotherapy Resistance in Triple-Negative Breast Cancer—How We Can Rise to the Challenge. *Cells*; 8: 957.
- [20]. Wahba HA, El-Hadaad HA. 2015. Current approaches in treatment of triple-negative breast cancer. *Cancer Biol Med*; 12: 106-116.
- [21]. Zafrakas M, Papisozomenou P, Emmanouilides C. 2016. Sorafenib in breast cancer treatment: A systematic review and overview of clinical trials. *World J Clin Oncol*; 7: 331-336.
- [22]. Bronte G, Andreis D, Bravaccini S, et al. 2017. Sorafenib for the treatment of breast cancer. *Expert Opinion on Pharmacotherapy*; 18: 621-630.
- [23]. Wei J-c, Meng F-d, Qu K, et al. 2015. Sorafenib inhibits proliferation and invasion of human hepatocellular carcinoma cells via up-regulation of p53 and suppressing FoxM1. *Acta Pharmacologica Sinica*; 36: 241-251.
- [24]. Oh SJ, Erb HH, Hobisch A, et al. 2012. Sorafenib decreases proliferation and induces apoptosis of prostate cancer cells by inhibition of the androgen receptor and Akt signaling pathways. *Endocr Relat Cancer*; 19: 305-319.
- [25]. Dattachoudhury S, Sharma R, Kumar A, et al. 2020. Sorafenib inhibits proliferation, migration and invasion of breast cancer cells. *Oncology*; 98: 478-486.
- [26]. Aydin HE, Koldemir-Gündüz M, Kizmazoglu C, et al. 2021. Cytotoxic effect of boron application on glioblastoma cells. *Turk Neurosurg*; 31: 206-210.
- [27]. Hacıoğlu C, Kar F, Kacar S, et al. 2020. High Concentrations of Boric Acid Trigger Concentration-Dependent Oxidative Stress, Apoptotic Pathways and Morphological Alterations in DU-145 Human Prostate Cancer Cell Line. *Biological Trace Element Research*; 193: 400-409.
- [28]. Lee A, Djamgoz MBA. 2018. Triple negative breast cancer: Emerging therapeutic modalities and novel combination therapies. *Cancer Treatment Reviews*; 62: 110-122.
- [29]. Gradishar WJ, Kaklamani V, Sahoo TP, et al. 2013. A double-blind, randomised, placebo-controlled, phase 2b study evaluating sorafenib in combination with paclitaxel as a first-line therapy in patients with HER2-negative advanced breast cancer. *European Journal of Cancer*; 49: 312-322.
- [30]. Baselga J, Segalla JGM, Roché H, et al. 2012. Sorafenib in Combination With Capecitabine: An Oral Regimen for Patients With HER2-Negative Locally Advanced or Metastatic Breast Cancer. *Journal of Clinical Oncology*; 30: 1484-1491.

Radiological Properties of Some Chemotherapy Drugs for Electron, Proton and Carbon Ion Interactions in the Energy Region 10 keV – 400 MeV

Mehmet Büyükyıldız¹ , Murat Türemiş^{1*} 

¹ Faculty of Engineering and Natural Sciences, Department of Physics, Bursa Technical University, Bursa, Türkiye

* muratturemis@hotmail.com

* Orcid No: 0000-0001-8849-4364

Received: 4 July 2022

Accepted: 8 June 2023

DOI: 10.18466/cbayarfbe.1140327

Abstract

Radiological properties of some chemotherapy drugs such as Doxorubicin, Vincristine, Teniposide, Azathioprine, Etoposide, Cyclophosphamide, Vinblastine and Bleomycin were investigated according to total electron interaction and some heavy charged particle interactions on behalf of effective atomic numbers (Z_{eff}) and electron densities (N_{eff}) for the first time. Calculations were performed for total electron, proton and C ion interactions, commonly used in therapy, in the energy region 10 keV- 400 MeV. Variation of Z_{eff} s and N_{eff} s of given drugs was studied according to the energy of electron or heavy charged particles and significant variations were observed for all types of interaction in the given energy region. The highest values of Z_{eff} were found in the different regions of energy for different particle interactions remarkably and variation in N_{eff} seems approximately to be same with alteration in Z_{eff} for the investigated drugs. Also, Z_{eff} values of all drugs were plotted together and compared with each other for electron, proton and C ion interactions in the continuous energy region. Maximum and minimum values of Z_{eff} were observed in Azathioprine (6.14) and Vinblastine (2.25) for electron interaction and proton interaction in the continuous energy region, respectively. The obtained results were compared with the Phy-X/ZEXTRA program between 10 keV-15 MeV energy region.

Keywords: Charged particles, chemotherapy drugs, effective atomic number, electron density

1. Introduction

Besides photons, electrons, protons and heavy ions became a commonly used instrument in radiotherapy, cancer and diagnostic applications [1]. On the other hand, the effect of ionizing radiation on human body parts, tissues, biomolecules and drugs is characterized by absorbed dose, energy and type of radiation in terms of radiation response. Thus, studies on the interactions of ionizing radiation with industrial materials, drugs or complex molecules are significant in related fields like cancer therapy. Chemotherapy is known as a cancer treatment using drugs to break down cancer cells or tumors, and radiotherapy uses X-, gamma rays and charged particles to demolish the cancer cells. Whereas chemoradiation is the treatment in which chemotherapy and radiotherapy are used at the same time for certain types of cancer. Chemotherapy drugs are vital for cancer treatment, thus the interaction of radiation with the drugs is significant in terms of radiation response or distinguishable especially in chemoradiation.

Mass attenuation coefficient and stopping power are diverse parameters characterizing the materials in terms of radiation response for photons and charged particles such as electrons, protons and heavy ions. Also, Z_{eff} and N_{eff} are useful physical properties both photons and others in health, biophysics, dosimetric applications, medical and particle physics. A multi-element material can be characterized via a term Z_{eff} to obey equivalence since a single number cannot characterize the multi-element material for the energy of a photon as revealed by Hine [2]. It also relies on photon energy. In addition, it is significant for calculating other properties like absorbed dose in health. Because the dose in medical physics is being utilized for radiological aims such as diagnosis and therapy. N_{eff} designates the number of electrons per unit mass of a material. Because Z_{eff} and N_{eff} are exclusive properties utilized to characterize different types of materials, this makes them distinguished properly and, thus drugs are better distinguished from each other in the continuous energy region.

In addition, if it is estimated how the radiation response of the material is, the damage to healthful tissues or drugs will be minimized due to the fact that these drugs can have various physiological effects on life regimes [3].

There are some studies about drugs with regard to Z_{eff} and N_{eff} in literature. Mass attenuation coefficient, effective atomic numbers and electron densities of some narcotic drugs were investigated for total and partial photon interactions in the energy range 1 keV - 100 GeV [4]. The mass attenuation coefficient and effective atomic number of the active pharmaceutical ingredients were calculated for total and partial photon interactions in the energy range from 1 keV to 100 GeV and some significant variations were observed in the effective atomic numbers of drugs [5]. Effective atomic numbers, electron densities, energy absorption and exposure buildup factors of some anti-inflammatory drugs were computed in a 0.015–15 MeV energy region up to a penetration depth of 40 mfp (mean free path) and variations of these parameters of drugs were evaluated in the continuous energy region [6]. Effective atomic numbers, electron densities and photon buildup factors of some chemotherapy drugs, used simultaneously with radiation therapy for cancer treatments, were calculated in a 0.015–15 MeV energy region [7-9].

Charged particles such as electrons and heavy ions are often utilized in medical physics for radiotherapy or diagnosis. So these particles are significant for health in applications [10]. But there is no article showing Z_{eff} and N_{eff} of the drugs for the charged particle interaction. This motivated us to carry out this work. Electrons and heavy ions were used to study the radiological quantities viz. Z_{eff} and N_{eff} of some chemotherapy drugs in the present work for the first time. Z_{eff} s and N_{eff} s of the drugs were calculated for total electron interaction, proton and C ion interactions in the energy region 10 keV-400 MeV. The investigated drugs are shown in Table 1.

Table 1. The chemical formula of chemotherapy drugs.

1	Doxorubicin	$C_{27}H_{29}NO_{11}$
2	Vincristine	$C_{46}H_{56}N_4O_{10}$
3	Teniposide	$C_{32}H_{32}O_{13}S$
4	Azathioprine	$C_9H_7N_7O_2S$
5	Etoposide	$C_{29}H_{32}O_{13}$
6	Cyclophosphamide	$C_7H_{15}Cl_2N_2O_2P$
7	Vinblastine	$C_{46}H_{58}N_4O_9$
8	Bleomycin	$C_{55}H_{84}N_{17}O_{21}S_3$

2. Method

The used method work was adopted for the computation of Z_{eff} s and N_{eff} s for electrons, protons and heavy ions in our last study [11] and some other studies [12-15]. Mass stopping powers of the drugs were firstly determined by the NIST database [16] and the SRIM [17] code for particles. Then, this data was established spanning the

lowest and the highest elements present in the investigated materials between 10 keV-10 MeV. And the Z_{eff} has been computed by the logarithmic interpolation procedure:

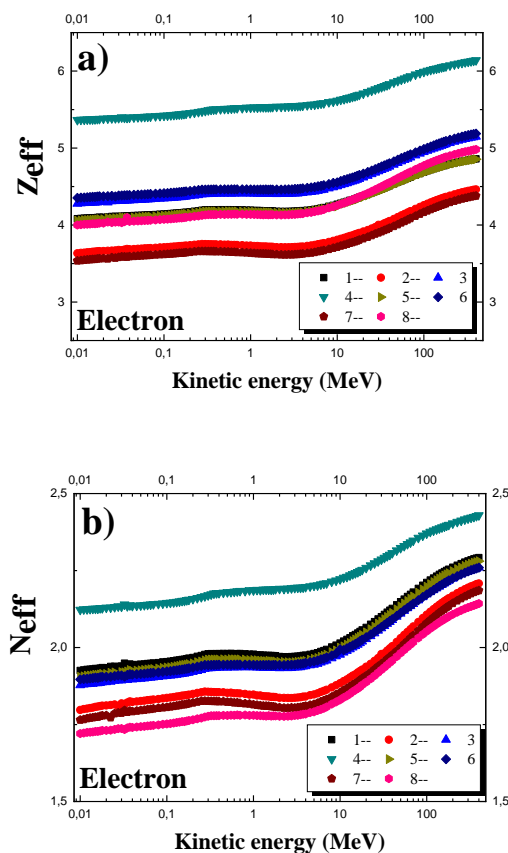
$$Z_{eff} = \frac{Z_1(\log \sigma_2 - \log \sigma) + Z_2(\log \sigma - \log \sigma_1)}{\log \sigma_2 - \log \sigma_1} \quad (1)$$

where σ_1 and σ_2 are the stopping cross section (cm^{-1} , expressed per atom) of Z_1 and Z_2 atoms. σ is the stopping cross section of the material that lies between Z_1 and Z_2 elements. This method was utilized to compute the Z_{eff} of the drugs for used particles by replacing the stopping cross section in Eq. 1. After that electron densities (N_{eff}) of the drugs for charged particles have been calculated through the below formula with the mean atomic mass of drugs:

$$N_{eff} = N_A \frac{nZ_{eff}}{\sum_i n_i A_i} = N_A \frac{Z_{eff}}{\langle A \rangle} \left(\frac{electrons}{g} \right) \quad (2)$$

3. Results and Discussion

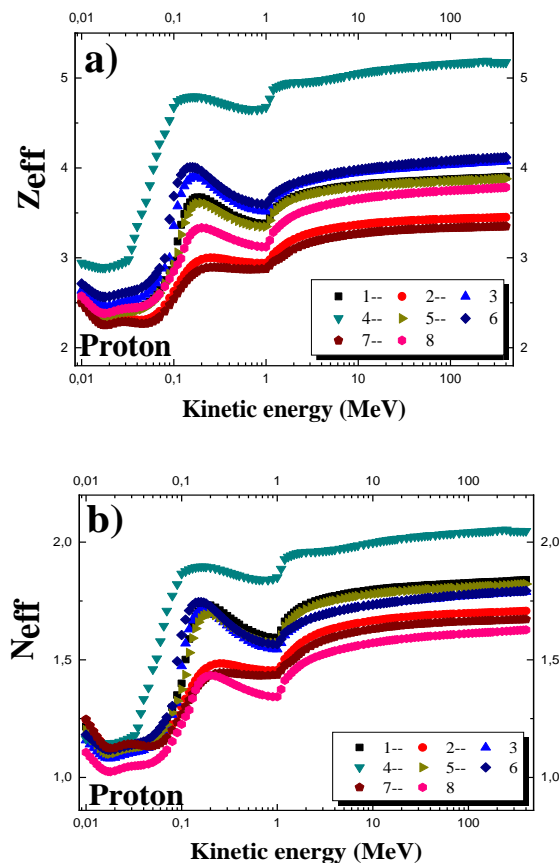
Effective atomic numbers of the selected chemotherapy drugs were determined utilizing the mass stopping powers obtained via the NIST and SRIM code in the energy region 10 keV- 400 MeV.



Figures 1. Effective atomic numbers and electron densities of the selected chemotherapy drugs for electron interaction.

The drugs have different chemical formulas, mass stopping powers and elemental cross section. Mass stopping power is used to calculate Z_{eff} especially, therefore changes in Z_{eff} are in accordance with mass stopping power. Figs. 1 show the change in Z_{eff} s and N_{eff} s of the selected chemotherapy drugs for electrons in the continuous energy region (10 keV- 400 MeV).

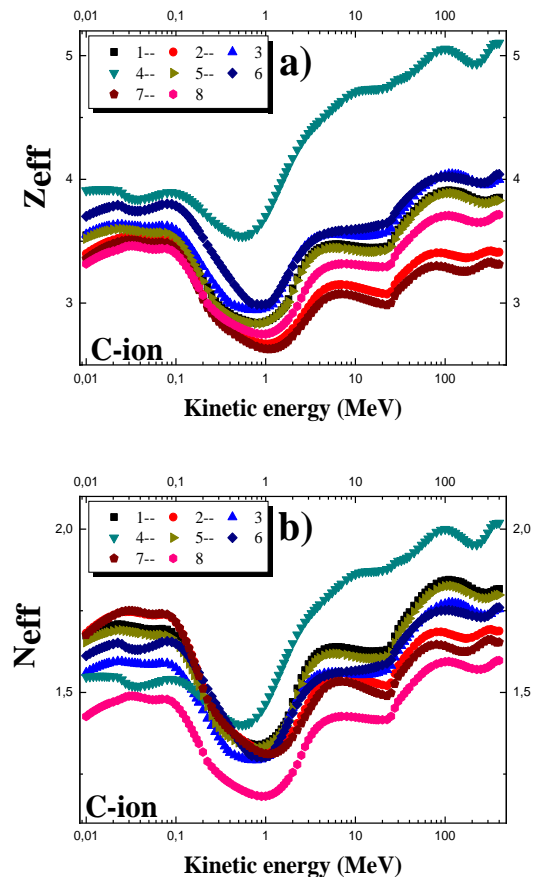
As shown in this Figure 1, the lowest values of Z_{eff} are observed at lower energy values and the highest values are observed at higher energies for all the chemotherapy drugs. On the other hand, the variation of N_{eff} s shows the same energy habituation expectedly as Z_{eff} because N_{eff} is nearly concerned with the effective atomic number as shown in Fig. 1(b) for electron interaction. Effective atomic numbers and electron densities of the selected chemotherapy drugs for proton interaction were shown in graphical form in the energy region 10 keV-400 MeV (Figs. 2).



Figures 2. Effective atomic numbers and electron densities of the selected chemotherapy drugs for proton interaction.

It can be clearly seen from Fig. 2(a), Z_{eff} makes a peak between 0.1-0.2 MeV and it decreases up to around 1 MeV, then it increases up to around 400 MeV for the drugs.

Also, Z_{eff} has the lowest values at lower energy values and has the highest values at higher energies for the chemotherapy drugs generally. N_{eff} of the chemotherapy drugs show the same variations as Z_{eff} in the entire energy region as expected for proton interaction (Fig. 2b). As shown in Fig. 3(a), Z_{eff} does not show large variations up to around 0.1 MeV for C ion interaction. After it decreases around 0.7-1 MeV and makes a minimum, then it increases and has the maximum values at higher ion energies (after around 100 MeV). Naturally, N_{eff} shows the same qualitative energy dependence in the studied region for C ion interaction from Fig. 3(b).



Figures 3. Effective atomic numbers and electron densities of the selected chemotherapy drugs for C ion interaction.

Table 2. Mean, minimum and maximum values of Z_{eff} of the given materials for electron, proton and C ion.

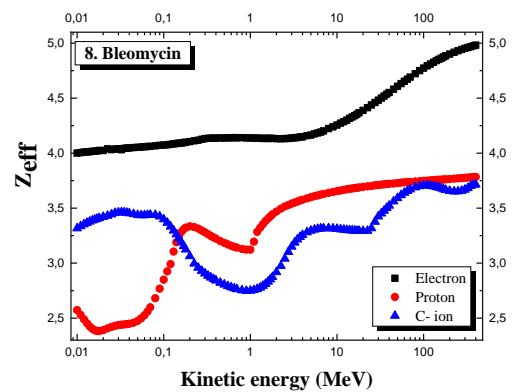
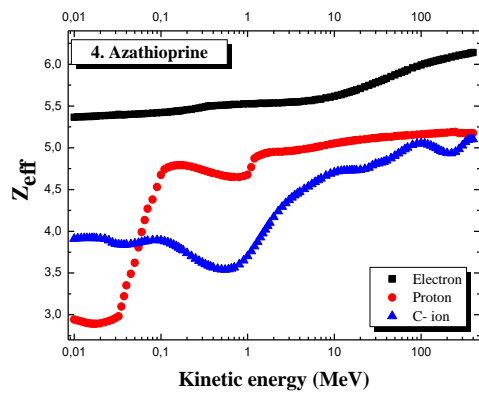
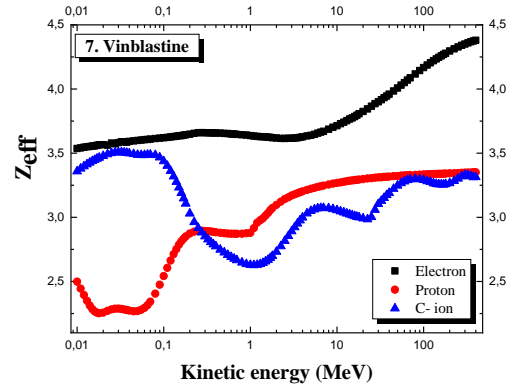
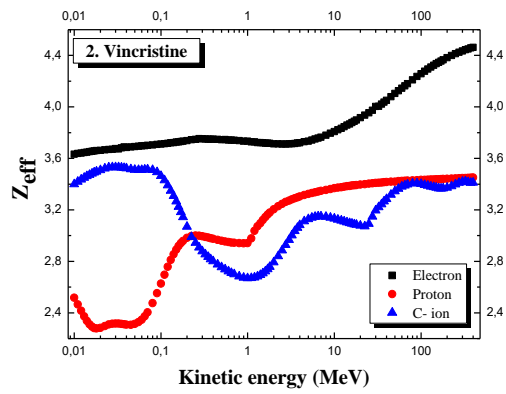
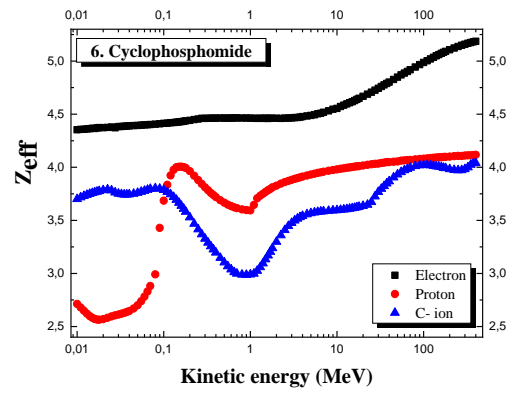
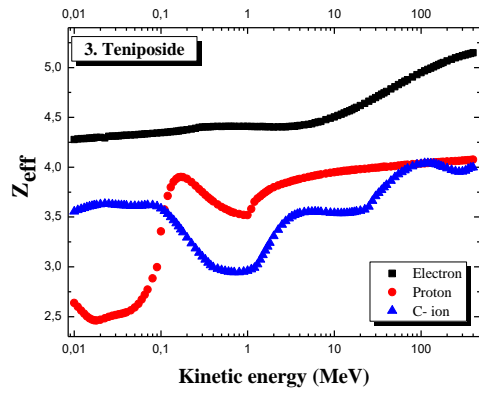
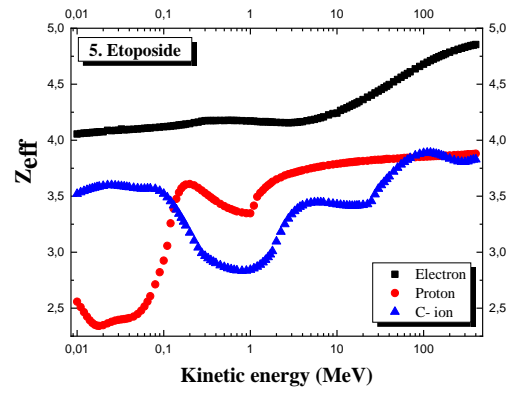
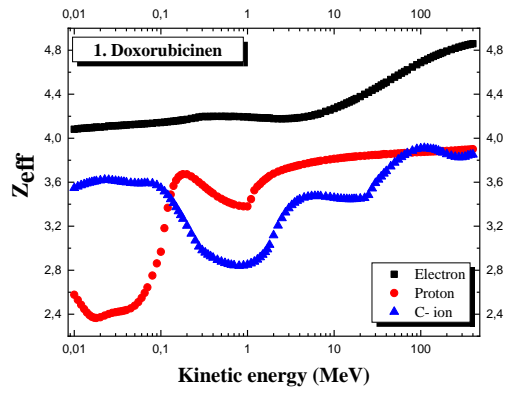
Z_{eff}	Mean	Min	Max	Mean	Min	Max
	Electron			Proton		
Doxorubicin	4.32	4.08	4.86	3.45	2.37	3.90
Vincristine	3.96	3.65	4.46	3.04	2.28	3.45
Teniposide	4.54	4.28	5.15	3.60	2.46	4.08
Azathioprine	5.63	5.37	6.14	4.62	2.89	5.19
Etoposide	4.30	4.00	4.85	3.42	2.34	3.88
Cyclophosphamide	4.60	4.00	5.19	3.67	2.56	4.12
Vinblastine	3.78	3.54	4.38	2.96	2.25	3.35
Bleomycin	4.30	4.00	4.98	3.30	2.38	3.78
	C-ion					
Doxorubicin	3.46	2.84	3.91			
Vincristine	3.19	2.67	3.53			
Teniposide	3.55	2.94	4.04			
Azathioprine	4.29	3.54	5.10			
Etoposide	3.43	2.83	3.89			
Cyclophosphamide	3.63	2.99	4.04			
Vinblastine	3.13	2.63	3.51			
Bleomycin	3.30	2.75	3.72			

Table 3. Mean, minimum and maximum values of N_{eff} of the given materials for electron, proton and C ion.

N_{eff}	Mean	Min	Max	Mean	Min	Max
	Electron			Proton		
Doxorubicin	2.04	1.93	2.29	1.63	1.12	1.84
Vincristine	2.97	1.82	2.21	1.51	1.13	1.71
Teniposide	2.00	1.88	2.26	1.58	1.08	1.79
Azathioprine	2.23	2.12	2.43	1.83	1.14	2.05
Etoposide	2.02	1.88	2.28	1.61	1.10	1.82
Cyclophosphamide	2.00	1.74	2.26	1.60	1.12	1.79
Vinblastine	1.89	1.76	2.19	1.48	1.12	1.67
Bleomycin	1.85	1.72	2.14	1.42	1.02	1.63
	C-ion					
Doxorubicin	1.63	1.34	1.84			
Vincristine	1.58	1.32	1.75			
Teniposide	1.56	1.29	1.77			
Azathioprine	1.70	1.40	2.02			
Etoposide	1.61	1.33	1.83			
Cyclophosphamide	1.58	1.30	1.76			
Vinblastine	1.56	1.31	1.75			
Bleomycin	1.42	1.18	1.60			

The basic statistical information for effective atomic numbers and electron densities of the chemotherapy drugs for the different particle interactions are seen in Table 2 and Table 3, respectively. Azathioprine has the maximum Z_{eff} (6.14, 5.19, 5.10) for electron, proton and C ion interactions respectively (Table 2) due to the heavier elements contributions. But Vinblastine has the minimum Z_{eff} (3.54, 2.25, 2.63) for electron, proton and C ion interactions respectively (Table 2).

In addition, maximum values of Z_{eff} decrease as the weight of particles increases (electron, proton, C respectively). It can be seen that N_{eff} of the chemotherapy drugs have the same variations for Azathioprine (max: 2.43, 2.05 and 2.02) for electron, proton and C ion interactions respectively (Table 3). Variations in Z_{eff} of the drugs were plotted for all interaction types in Fig. 4.



Figures 4. Variations in Z_{eff} for electron, proton and C ion interactions.

It can be obviously seen from the figures, electron interaction has higher values than proton and C ion interaction in Z_{eff} s of the drugs. In addition, differences between proton and C ion interactions are larger at lower energies and the drugs have the same Z_{eff} value between 0.05-0.3 MeV energies for the ions. The differences decrease as ion energy increases and after 50 MeV they get the same Z_{eff} again.

The obtained results were compared with the Phy-X/ZeXTRa program between 10 keV-15 MeV energy region. Phy-X/ZeXTRa program calculates the effective atomic number of different types of materials for photon, electron, proton and C ion between 10 keV – 15 MeV energy region [18]. For comparison differences (%) between the obtained and Phy-X/ZeXTRa results in Z_{eff} were calculated as $diff. (\%) = \left(\frac{Z_{eff.ZeXTRa} - Z_{eff.calc}}{Z_{eff.ZeXTRa}} \right) \cdot 100$ in the energy region 10 keV -15 MeV. A minimum difference (0.97%) was observed for electron interaction in the energy region. But a maximum difference (20.30%) was observed for C ion interaction for Vinblastine in the energy region as shown in Fig. 5.

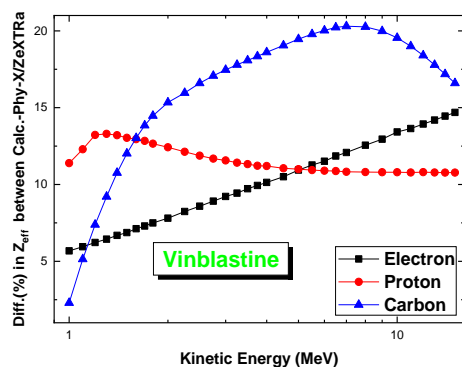


Figure 5. Differences (%) between calculated and ZeXTRa values in Z_{eff} for electron, proton and C ion interactions.

4. Conclusion

Chemotherapy drugs are important for cancer treatment. Therefore, it is very important the drugs are distinguished from each other according to Z_{eff} and N_{eff} in the energy region in irradiated application. Some chemotherapy drugs were studied according to Z_{eff} and N_{eff} for the first time in energy region 10 keV-400 MeV for total electron, proton and C ions interaction. Variations of Z_{eff} and N_{eff} have been studied for charged particle interactions with particle energy. The highest and lowest values of Z_{eff} were observed in Azathioprine (6.14) for electron interaction and in Vinblastine (2.25) for proton interaction in the continuous energy region respectively. Z_{eff} s for electron, proton and C interactions have not the same value, but for proton and C ions, it

has the same value two or three times in the continuous energy region interestingly.

It can be said that N_{eff} s of the drugs have the same intersections because of the mathematical relation between Z_{eff} and N_{eff} . It can be also concluded that Z_{eff} and N_{eff} depend on ion energy like photon interaction. The obtained results were also compared with the Phy-X/ZeXTRa program, and the maximum difference (%) was observed for Vinblastine as 20.30%. The obtained data should be helpful in developing software programs and chemoradiation when charged particles into these materials as they represent the interaction of particles with these drugs in the continuous energy region.

Author's Contributions

Mehmet Büyükyıldız: Made literature search and experiments, writing - review & editing.

Murat Türemiş: Data curation, investigation, helped in manuscript preparation & editing.

Ethics

There are no ethical issues after the publication of this manuscript.

References

- [1] Barth, W., Dahl, L., Glatz, J., Groening, L., Richter, S. and Yaramishev, S. Proceedings of the European Workshop on Beam Diagnostics and Instrumentation for Particle Accelerators, Mainz, Germany, 2003, pp 161-163.
- [2] Hine, G.J. 1952. The effective atomic numbers of materials for various gamma interactions. *Physical Review*; 85: 725-728.
- [3] Kurudirek, M. and Onaran, T. 2015. Calculation of effective atomic number and electron density of essential biomolecules for electron, proton, alpha particle and multi-energetic photon interactions. *Radiation Physics and Chemistry*; 112: 125-138.
- [4] Gounhalli, S.G., Shantappa, A. and Hanagodimath, S.M. 2012. Studies on mass attenuation coefficient, effective atomic numbers and electron densities of some narcotic drugs in the energy range 1 keV - 100 GeV. *Journal of Applied Physics*; 2: 40-48.
- [5] Manjunath, A. and Kerur, B.R. 2015. Studies of pharmaceutical active ingredients in drugs through radiological parameters. *Physical Science International Journal*; 7: 186-191.
- [6] Ekinci, N., Kavaz, E. and Özdemir, Y. 2014. A study of the energy absorption and exposure buildup factors of some anti-inflammatory drugs. *Applied Radiation and Isotopes*; 90: 265-273.
- [7] Kavaz, E., Ahmedishadbad, N. and Özdemir Y. 2015. Photon buildup factors of some chemotherapy drugs. *Biomed Pharmacother*; 69: 34-41.
- [8] Akman, F. and Kaçal, M. R. 2018. Investigation of radiation attenuation parameters of some drugs used in Chemotherapy in Wide Energy Region. *Journal of Radiology and Oncology*; 2: 047-052.
- [9] Tuğrul, T. 2020. Investigation of mass attenuation coefficients, effective atomic numbers, and effective electron density for some

molecules: study on chemotherapy drugs. *Journal of Radiation Research and Applied Sciences*; 13(1): 758-764.

[10] Newhauser, W. D. and Zhang, R. 2015. The physics of proton therapy. *Physics in Medicine & Biology*; 60: R155-R209

[11] Büyükyıldız, M. 2017. Investigation of radiological properties of some shielding materials on charged and uncharged radiation interaction for neutron generator. *Radiation Effects and Defects in Solids*; 172 (1-2): 1-19.

[12] Kurudirek, M. 2014. Radiation shielding and effective atomic number studies in different types of shielding concretes, lead base and non-lead base glass systems for total electron interaction: A comparative study. *Nuclear Engineering and Design*; 280: 440-448.

[13] Kurudirek, M. 2014. Effective atomic numbers of different types of materials for proton interaction in the energy region 1 keV–10 GeV. *Nuclear Instruments and Methods in Physics Research, Section B*; 336: 130-134.

[14] Kurudirek, M. 2015. Studies on heavy charged particle interaction, water equivalence and Monte Carlo simulation in some gel dosimeters, water, human tissues and water phantoms. *Nuclear Instruments and Methods in Physics Research, Section A*; 795: 239-252.


[15] Kurudirek, M. 2016. Effective atomic number, energy loss and radiation damage studies in some materials commonly used in nuclear applications for heavy charged particles such as H, C, Mg, Fe, Te, Pb and U. *Radiation Physics and Chemistry*; 122: 15-23.

[16] Berger, M.J., Coursey, J.S., Zucker, M.A. and Chang, J. 2005. "ESTAR, PSTAR and ASTAR: Computer program for calculating stopping power and range tables for Electron, Proton and Helium ions (version 1.2.3)", <https://dx.doi.org/10.18434/T4NC7P> (Online) available: <http://physics.nist.gov/Star>. (accessed at 20.03.2022) National Institute of Standards and Technology, Gaithersburg, MD. Originally published as: Berger MJ, NISTIR 4999, National Institute of Standards and Technology, Gaithersburg, MD (1993).

[17] Ziegler, J.F., Ziegler, M.D. and Biersack, J.P. 2010. SRIM – The Stopping and Range of Ions in Matter. *Nuclear Instruments and Methods in Physics Research, Section B*; 268: 1818–1823.

[18] Özpolat, Ö.F., Alım, B., Şakar, E., Büyükyıldız, M., Kurudirek, M. 2020. Phy-X/ZEXTRA: a software for robust calculation of effective atomic numbers for photon, electron, proton, alpha particle, and carbon ion interactions. *Radiation and Environmental Biophysics*; 59(2): 321-329.

On the Continuity Properties of the Set of Trajectories of the Control System with Limited Control Resources

Anar Huseyin^{1*} 

¹ Sivas Cumhuriyet University, Faculty of Science, Department of Statistics and Computer Sciences, Sivas, Türkiye

*ahuseyin@cumhuriyet.edu.tr

*Orcid No: 0000-0002-3911-2304

Received: 2 November 2022

Accepted: 30 May 2023

DOI: 10.18466/cbayarfbe.1198603

Abstract

In this paper the control system with integral constraint on the control functions is studied where the behavior of the system by the Urysohn type integral equation is described. The admissible control functions are chosen from the closed ball of the space $L_p([a, b]; R^m)$ ($p > 1$) centered at the origin with radius r . Dependence of the set of trajectories on r and p is investigated. It is proved that the set of trajectories is Lipschitz continuous with respect to r and is continuous with respect to p . The robustness of the trajectory with respect to the fast consumption of the remaining control resource is established.

Keywords: control system, Hausdorff distance, integral constraint, robustness, Urysohn integral equation.

1. Introduction

The control systems arise in different areas of physics, mechanics, airspace navigation, economics, sociology, etc. and depending on character of control efforts are classified as control systems with geometric constraints, integral constraints and mixed constraints on the control functions. The theory of control systems with geometric constraints on the control functions is enough well investigated chapter of the control systems theory (see, e.g. [4], [13], [16], [20] and references therein). But integral constraints on the control functions arise in the cases when the control resource is exhausted by consumption such as energy, fuel, finance, etc. (see, e.g. [3], [6], [12], [15], [18], [21], [22], [23]). Note that integral boundedness of the control function does not imply its geometric boundedness. This situation causes additional difficulties and therefore studying the control systems with integral constraints on the control functions requires special methods.

Integral equations are very adequate tool to describe the behaviors of various processes arising in the theory and applications (see, e.g. [2], [7], [17], [19], [24]). In this paper the control system described by Urysohn type integral equation is considered. The control functions are chosen from the closed ball of the space $L_p([a, b]; R^m)$ ($p > 1$) centered at the origin with radius r . Note that the different topological properties and approximate

constructions methods of the set of trajectories of the control systems described by various type integral equations and integral constraints on the control functions are studied in papers [8-11].

The paper is organized as follows. In Section 2 the basic conditions and propositions are formulated which are used in following arguments. In Section 3 it is proved that the set of trajectories is Lipschitz continuous with respect to r (Theorem 3.1). In Section 4 it is shown that the set of trajectories depends on p continuously (Theorem 4.1). In Section 5 it is proved that system's trajectory is robust with respect to the fast consumption of the remaining control resource (Theorem 5.1) and it is shown that every trajectory can be approximated by trajectory obtained by the full consumption of the available control resource (Theorem 5.2).

2. The System's Description

Consider control system the behavior of which is described by Urysohn type integral equation

$$x(t) = f(t, x(t)) + \lambda \int_a^b K(t, s, x(s), u(s)) ds \quad (2.1)$$

where $t \in [a, b]$, $x(t) \in R^n$ is the state vector, $u(s) \in R^m$ is the control vector, $\lambda \geq 0$.

For given $p > 1$ and $r \geq 0$ we denote

$$U_{p,r} = \{u(\cdot) \in L_p([a, b]; R^m) : \|u(\cdot)\|_p \leq r\}$$

which is called the set of admissible control functions and every $u(\cdot) \in U_{p,r}$ is said to be an admissible control function, where $L_p([a, b]; R^m)$ is the space of Lebesgue measurable functions $u(\cdot): [a, b] \rightarrow R^m$ such that $\|u(\cdot)\|_p < \infty$, $\|u(\cdot)\|_p = \left(\int_a^b \|u(s)\|^p ds\right)^{\frac{1}{p}}$, $\|\cdot\|$ denotes the Euclidean norm.

It is obvious that the set of admissible control functions $U_{p,r}$ is the closed ball with radius r and centered at the origin in the space $L_p([a, b]; R^m)$.

It is assumed that the functions and a number λ given in system (2.1) satisfy the following conditions:

2.A. the functions $f(\cdot, \cdot): [a, b] \times R^n \rightarrow R^n$ and $K(\cdot, \cdot, \cdot, \cdot): [a, b] \times [a, b] \times R^n \times R^m \rightarrow R^n$ are continuous;

2.B. there exist $l_0 \in [0, 1)$, $l_1 \geq 0$, $\gamma_1 \geq 0$, $l_2 \geq 0$, $\gamma_2 \geq 0$, $l_3 \geq 0$, $\gamma_3 \geq 0$ such that

$$\|f(t, x_1) - f(t, x_2)\| \leq l_0 \|x_1 - x_2\|$$

for every $(t, x_1) \in [a, b] \times R^n$, $(t, x_2) \in [a, b] \times R^n$ and

$$\begin{aligned} & \|K(t_1, s, x_1, u_1) - K(t_2, s, x_2, u_2)\| \\ & \leq [l_1 + \gamma_1 (\|u_1\| + \|u_2\|)] \|t_1 - t_2\| \\ & \quad + [l_2 + \gamma_2 (\|u_1\| + \|u_2\|)] \|x_1 - x_2\| \\ & \quad + [l_3 + \gamma_3 (\|x_1\| + \|x_2\|)] \|u_1 - u_2\| \end{aligned}$$

for every $(t_1, s, x_1, u_1) \in [a, b] \times [a, b] \times R^n \times R^m$, $(t_2, s, x_2, u_2) \in [a, b] \times [a, b] \times R^n \times R^m$;

2.C. there exist $p_* > 1$ and $r_* > 0$ such that the inequality

$$\lambda \left(l_2(b-a) + 2\gamma_* r_* (b-a)^{\frac{p_*-1}{p_*}} \right) < 1 - l_0$$

is satisfied where $\gamma_* = \max \{\gamma_1, \gamma_2, \gamma_3\}$.

If the function $(t, s, x, u) \rightarrow K(t, s, x, u)$, $(t, s, x, u) \in [a, b] \times [a, b] \times R^n \times R^m$, is Lipschitz continuous with respect to (t, x, u) , then it satisfies the condition 2.B.

We set

$$L(\lambda; p, r) = l_0 + \lambda \left(l_2(b-a) + 2\gamma_* r (b-a)^{\frac{p-1}{p}} \right) \quad (2.2)$$

From Condition 2.C it follows that

$$0 \leq L(\lambda; p_*, r_*) < 1. \quad (2.3)$$

Then there exist $\beta_1 > 0$, $\beta_2 > 0$ such that $L(\lambda; p, r) < 1$ for every $p \in [p_* - \beta_1, p_* + \beta_1]$ and $r \in [0, r_* + \beta_2]$.

Denote

$$L_*(\lambda) = \max \{L(\lambda; p, r) : p \in [p_* - \beta_1, p_* + \beta_1], r \in [0, r_* + \beta_2]\}. \quad (2.4)$$

From (2.2), (2.3) and (2.4) it follows that

$$0 \leq L_*(\lambda) < 1, \quad L_*(\lambda) - l_0 \geq 0 \quad (2.5)$$

From now on, it will be assumed that $p \in [p_* - \beta_1, p_* + \beta_1]$ and $r \in [0, r_* + \beta_2]$.

Now, let us define a trajectory of the system (2.1) generated by given admissible control function $u(\cdot) \in U_{p,r}$. A continuous function $x(\cdot): [a, b] \rightarrow R^n$ satisfying the integral equation (2.1) for every $t \in [a, b]$, is said to be a trajectory of the system (2.1) generated by the admissible control function $u(\cdot) \in U_{p,r}$. The set of trajectories of the system (2.1) generated by all admissible control functions $u(\cdot) \in U_{p,r}$ is denoted by symbol $X_{p,r}$ and is called the set of trajectories of the system (2.1).

The conditions 2.A-2.C guarantee that every admissible control function $u(\cdot) \in U_{p,r}$ generates a unique trajectory $x(\cdot) \in C([a, b]; R^n)$ of the system (2.1) (see, Theorem 3.1 of [8]), where $C([a, b]; R^n)$ is the space of continuous functions $x(\cdot): [a, b] \rightarrow R^n$ with norm $\|x(\cdot)\|_C = \max\{\|x(t)\| : t \in [a, b]\}$. Analogously to the Theorem 4.1 of [8] it is possible to show that there exists $\beta_* > 0$ such that

$$\|x(\cdot)\|_C \leq \beta_* \quad (2.6)$$

for every $x(\cdot) \in X_{p,r}$, $p \in [p_* - \beta_1, p_* + \beta_1]$ and $r \in [0, r_* + \beta_2]$. Moreover, by virtue of Theorem 5.1 of [8] we have that the set of trajectories $X_{p,r}$ is a precompact subset of the space $C([a, b]; R^n)$.

Let us give an auxiliary proposition which will be used in following arguments.

Proposition 2.1. Let $u_1(\cdot) \in U_{p,r_1}$, $u_2(\cdot) \in U_{p,r_2}$ where $p \in [p_* - \beta_1, p_* + \beta_1]$, and $r_1 \in [0, r_* + \beta_2]$, $r_2 \in [0, r_* + \beta_2]$. Then

$$\lambda \int_a^b (l_2 + \gamma_2 [\|u_1(s)\| + \|u_2(s)\|]) ds \leq L_*(\lambda) - l_0$$

where $L_*(\lambda)$ is defined by (2.4).

The proof of the proposition follows from Hölder's inequality.

For given metric space $(Z, d_Z(\cdot, \cdot))$ the Hausdorff distance between the sets $F \subset Z$ and $E \subset Z$ is denoted by $h_Z(F, E)$ and defined as

$$h_Z(F, E) = \max \{ \sup_{x \in F} d_Z(x, E), \sup_{y \in E} d_Z(y, F) \}$$

where $d_Z(x, E) = \inf \{ d_Z(x, y) : y \in E \}$.

Now let $(Z, d_Z(\cdot, \cdot))$ be a metric space and $b(Z)$ be a family of all nonempty bounded subsets of Z . Then $(b(Z), h_Z(\cdot, \cdot))$ is a pseudometric space where $h_Z(\cdot, \cdot)$ stands for Hausdorff distance between subsets of the space $(Z, d_Z(\cdot, \cdot))$ (see, e.g. [1], [14]).

Let $(Y, d_Y(\cdot, \cdot))$ and $(Z, d_Z(\cdot, \cdot))$ be metric spaces, $\Phi(\cdot) : Y \rightarrow b(Z)$ be a given set valued map, and $y_* \in Y$. If $h_Z(\Phi(y), \Phi(y_*)) \rightarrow 0$ as $y \rightarrow y_*$, then the map $\Phi(\cdot)$ is called continuous at y_* .

If there exists $M_0 > 0$ such that

$$h_Z(\Phi(y_1), \Phi(y_2)) \leq M_0 \cdot d_Y(y_1, y_2)$$

for every $y_1 \in Y$ and $y_2 \in Y$, then the map $\Phi(\cdot)$ is called Lipschitz continuous with Lipschitz constant M_0 .

The Hausdorff distance between the sets $U \subset R^n$ and $V \subset R^n$ is denoted by $h_n(U, V)$ and the Hausdorff distance between the sets $G \subset C([a, b]; R^n)$ and $W \subset C([a, b]; R^n)$ is denoted by $h_C(G, W)$.

For $t \in [a, b]$ we set

$$X_{p,r}(t) = \{x(t) \in R^n : x(\cdot) \in X_{p,r}\}. \quad (2.7)$$

The set $X_{p,r}(t)$ is close to the attainable set notion used in control and dynamical systems theory and consists of points to which arrive the trajectories of the system at the instant of t (see, e.g. [4], [5], [6]).

It follows from Proposition 5.2 of [8] that $h_n(X_{p,r}(t), X_{p,r}(t_*)) \rightarrow 0$ as $t \rightarrow t_*$ for every fixed $t_* \in [a, b]$.

3. Lipschitz Continuity of the Set of Trajectories with Respect to r

In this section for each fixed $p \in [p_* - \beta_1, p_* + \beta_1]$ the Lipschitz continuity of the set valued map $r \rightarrow X_{p,r}$, $r \in [0, r_* + \beta_2]$, is proved. Denote

$$B_C(1) = \{x(\cdot) \in C([a, b]; R^n) : \|x(\cdot)\|_C \leq 1\} \quad (3.1)$$

$$l_* = \max \{(b-a)^{\frac{p-1}{p}} : p \in [p_* - \beta_1, p_* + \beta_1]\} \quad (3.2)$$

$$R_* = \frac{\lambda(l_3 + 2\beta_*\gamma_3)l_*}{1 - L_*(\lambda)} \quad (3.3)$$

where $L_*(\lambda)$ is defined by (2.4), β_* is given in (2.6).

Theorem 3.1. Let $p \in [p_* - \beta_1, p_* + \beta_1]$ be fixed. Then

$$h_C(X_{p,r_1}, X_{p,r_2}) \leq R_* |r_1 - r_2|$$

for every $r_1 \in [0, r_* + \beta_2]$, $r_2 \in [0, r_* + \beta_2]$ where R_* is defined by (3.3).

Proof. Let $r_1 < r_2$ and $x_*(\cdot) \in X_{p,r_2}$ be an arbitrarily chosen trajectory generated by the control function $u_*(\cdot) \in U_{p,r_2}$. Define a control function $\tilde{u}(\cdot) : [a, b] \rightarrow R^m$, setting

$$\tilde{u}(t) = \frac{r_1}{r_2} u_*(t), \quad t \in [a, b]. \quad (3.4)$$

Since $u_*(\cdot) \in U_{p,r_2}$, then from (3.4) it follows that $\tilde{u}(\cdot) \in U_{p,r_1}$. Let $\tilde{x}(\cdot) : [a, b] \rightarrow R^n$ be the trajectory of the system (2.1) generated by the control function $\tilde{u}(\cdot) \in U_{p,r_1}$. Then $\tilde{x}(\cdot) \in X_{p,r_1}$ and from condition 2.B and (2.1) we obtain

$$\begin{aligned} \|\tilde{x}(t) - x_*(t)\| &\leq l_0 \|\tilde{x}(t) - x_*(t)\| \\ &+ \lambda \int_a^b [l_2 + \gamma_2(\|\tilde{u}(s)\| + \|u_*(s)\|)] \\ &\quad \cdot \|\tilde{x}(s) - x_*(s)\| ds \\ &+ \lambda \int_a^b [l_3 + \gamma_3(\|\tilde{x}(s)\| + \|x_*(s)\|)] \\ &\quad \cdot \|\tilde{u}(s) - u_*(s)\| ds. \end{aligned} \quad (3.5)$$

From (2.6), (3.2), (3.4), Proposition 2.1 and Hölder's inequality it follows

$$\begin{aligned} &\lambda \int_a^b [l_2 + \gamma_2(\|\tilde{u}(s)\| + \|u_*(s)\|)] \\ &\quad \cdot \|\tilde{x}(s) - x_*(s)\| ds \\ &\leq \lambda \int_a^b [l_2 + \gamma_2(\|\tilde{u}(s)\| + \|u_*(s)\|)] ds \\ &\quad \cdot \|\tilde{x}(\cdot) - x_*(\cdot)\|_C \\ &\leq [L_*(\lambda) - l_0] \cdot \|\tilde{x}(\cdot) - x_*(\cdot)\|_C, \end{aligned} \quad (3.6)$$

$$\begin{aligned} &\lambda \int_a^b [l_3 + \gamma_3(\|\tilde{x}(s)\| + \|x_*(s)\|)] \\ &\quad \cdot \|\tilde{u}(s) - u_*(s)\| ds \end{aligned}$$

$$\begin{aligned} &\leq \lambda[l_3 + 2\beta_*\gamma_3] \int_a^b \left\| \frac{r_1}{r_2} u_*(s) - u_*(s) \right\| ds \\ &\leq \lambda[l_3 + 2\beta_*\gamma_3] \frac{|r_1 - r_2|}{r_2} r_2 (b - a)^{\frac{p-1}{p}} \\ &\leq \lambda[l_3 + 2\beta_*\gamma_3] L_* |r_1 - r_2|. \end{aligned} \quad (3.7)$$

(3.5), (3.6) and (3.7) imply that

$$\begin{aligned} \|\tilde{x}(t) - x_*(t)\| &\leq l_0 \|\tilde{x}(\cdot) - x_*(\cdot)\|_C \\ &\quad + [L_*(\lambda) - l_0] \cdot \|\tilde{x}(\cdot) - x_*(\cdot)\|_C \\ &\quad + \lambda[l_3 + 2\beta_*\gamma_3] L_* |r_1 - r_2| \end{aligned}$$

for every $t \in [a, b]$. The last inequality, (2.5) and (3.3) yield

$$\begin{aligned} \|\tilde{x}(\cdot) - x_*(\cdot)\|_C &\leq \frac{\lambda[l_3 + 2\beta_*\gamma_3] L_*}{1 - L_*(\lambda)} |r_1 - r_2| \\ &= R_* |r_1 - r_2|. \end{aligned} \quad (3.8)$$

So, by virtue of the inequality (3.8), for each $x_*(\cdot) \in X_{p,r_2}$ there exists $\tilde{x}(\cdot) \in X_{p,r_1}$ such that the inequality

$$\|\tilde{x}(\cdot) - x_*(\cdot)\|_C \leq R_* |r_1 - r_2|$$

is satisfied. This means that

$$X_{p,r_2} \subset X_{p,r_1} + R_* |r_1 - r_2| \cdot B_C(1) \quad (3.9)$$

where $B_C(1)$ is defined by (3.1). Keeping in mind that $X_{p,r_1} \subset X_{p,r_2}$, we have from (3.9) the proof of the theorem.

From Theorem 3.1 it follows that for each fixed $p \in [p_* - \beta_1, p_* + \beta_1]$ the set valued map $r \rightarrow X_{p,r}$, $r \in [0, r_* + \beta_2]$, is Lipschitz continuous with Lipschitz constant R_* .

From Theorem 3.1 we also obtain the validity of the following corollary.

Corollary 3.1. Let $p \in [p_* - \beta_1, p_* + \beta_1]$ be fixed. Then

$$h_C(X_{p,r_1}(t), X_{p,r_2}(t)) \leq R_* |r_1 - r_2|$$

for every $r_1 \in [0, r_* + \beta_2]$, $r_2 \in [0, r_* + \beta_2]$ and $t \in [a, b]$ where R_* is defined by (3.3), $X_{p,r}(t) \subset R^n$ is defined by (2.7).

4. Continuity of the Set of Trajectories with Respect to p

In this section the dependence of the set of trajectories on p will be investigated. At first let us define a distance

between the subsets of the spaces $L_{p_1}([a, b]; R^m)$ and $L_{p_2}([a, b]; R^m)$ where $p_1 \in [1, +\infty)$, $p_2 \in [1, +\infty)$.

The Hausdorff distance between the sets $Q \subset L_{p_1}([a, b]; R^m)$ and $D \subset L_{p_2}([a, b]; R^m)$ where $1 \leq p_1 < +\infty$, $1 \leq p_2 < +\infty$ is denoted by $H_1(Q, D)$ and is defined by

$$\begin{aligned} H_1(Q, D) &= \max \{ \sup_{x(\cdot) \in Q} d_{L_1}(x(\cdot), D), \\ &\quad \sup_{y(\cdot) \in D} d_{L_1}(y(\cdot), Q) \}. \end{aligned}$$

Here

$$d_{L_1}(x(\cdot), D) = \inf \{ \|x(\cdot) - y(\cdot)\|_1 : y(\cdot) \in D \},$$

$$\|x(\cdot) - y(\cdot)\|_1 = \int_a^b \|x(s) - y(s)\| ds.$$

We denote

$$q_* = \frac{\lambda(l_3 + 2\beta_*\gamma_3)}{1 - L_*(\lambda)} \quad (4.1)$$

where $L_*(\lambda)$ is defined by (2.4), β_* is given in (2.6).

Theorem 4.1. Let $r \in [0, r_* + \beta_2]$ and $p_0 \in (p_* - \beta_1, p_* + \beta_1)$ be fixed. Then for every $\varepsilon > 0$ there exists $\delta = \delta(\varepsilon, p_0, r) > 0$ such that for every $p \in (p_0 - \delta, p_0 + \delta)$ the inequality

$$h_C(X_{p,r}, X_{p_0,r}) \leq \varepsilon$$

holds.

Proof. By virtue of Theorem 3.6 from [5] we have that for fixed $r \in [0, r_* + \beta_2]$, $p_0 \in (p_* - \beta_1, p_* + \beta_1)$ and for given $\frac{\varepsilon}{q_*}$ there exists $\delta = \delta(\varepsilon, p_0, r) \in (0, p_0 - 1)$ such that

$$H_1(U_{p,r}, U_{p_0,r}) \leq \frac{\varepsilon}{q_*} \quad (4.2)$$

for every $p \in (p_0 - \delta, p_0 + \delta)$. Without loss of generality let us assume that

$$\delta = \delta(\varepsilon, p_0, r) < \min\{p_0 - p_* + \beta_1, p_* - p_0 + \beta_1\}$$

which implies that

$$(p_0 - \delta, p_0 + \delta) \subset (p_* - \beta_1, p_* + \beta_1). \quad (4.3)$$

Now, let us choose arbitrary $p \in (p_0 - \delta, p_0 + \delta)$ and $x(\cdot) \in X_{p,r}$, generated by admissible control function $u(\cdot) \in U_{p,r}$. According to (4.2) we have that for $u(\cdot) \in U_{p,r}$ there exists $v(\cdot) \in U_{p_0,r}$ such that

$$\|u(\cdot) - v(\cdot)\|_1 \leq \frac{\varepsilon}{q_*} \quad (4.4)$$

where $q_* > 0$ is defined by (4.1). Let $z(\cdot): [a, b] \rightarrow R^n$ be the trajectory of the system (2.1) generated by the admissible control function $v(\cdot) \in U_{p_0, r}$. Then $z(\cdot) \in X_{p_0, r}$ and from condition 2.B it follows that

$$\begin{aligned} \|x(t) - z(t)\| &\leq l_0 \|x(t) - z(t)\| \\ &+ \lambda \int_a^b [l_2 + \gamma_2(\|u(s)\| + \|v(s)\|)] \\ &\quad \cdot \|x(s) - z(s)\| ds \\ &+ \lambda \int_a^b [l_3 + \gamma_3(\|x(s)\| + \|z(s)\|)] \\ &\quad \cdot \|u(s) - v(s)\| ds \end{aligned} \quad (4.5)$$

From (2.6), (4.4) and Proposition 2.1 we have

$$\begin{aligned} &\lambda \int_a^b [l_2 + \gamma_2(\|u(s)\| + \|v(s)\|)] \\ &\quad \cdot \|x(s) - z(s)\| ds \\ &\leq \lambda \int_a^b [l_2 + \gamma_2(\|u(s)\| + \|v(s)\|)] ds \\ &\quad \cdot \|x(\cdot) - z(\cdot)\|_C \\ &\leq [L_*(\lambda) - l_0] \cdot \|x(\cdot) - z(\cdot)\|_C, \end{aligned} \quad (4.6)$$

$$\begin{aligned} &\lambda \int_a^b [l_3 + \gamma_3(\|x(s)\| + \|z(s)\|)] \\ &\quad \cdot \|u(s) - v(s)\| ds \\ &\leq \lambda [l_3 + 2\beta_*\gamma_3] \int_a^b \|u(s) - v(s)\| ds \\ &\leq \lambda [l_3 + 2\beta_*\gamma_3] \cdot \frac{\varepsilon}{q_*} \end{aligned} \quad (4.7)$$

From (4.5), (4.6) and (4.7) we obtain that

$$\begin{aligned} \|x(t) - z(t)\| &\leq l_0 \|x(\cdot) - z(\cdot)\|_C \\ &+ [L_*(\lambda) - l_0] \cdot \|x(\cdot) - z(\cdot)\|_C \\ &+ \lambda [l_3 + 2\beta_*\gamma_3] \cdot \frac{\varepsilon}{q_*} \\ &= L_*(\lambda) \cdot \|x(\cdot) - z(\cdot)\|_C + \lambda [l_3 + 2\beta_*\gamma_3] \cdot \frac{\varepsilon}{q_*} \end{aligned}$$

for every $t \in [a, b]$. The last inequality, (2.5) and (4.1) imply that

$$\|x(\cdot) - z(\cdot)\|_C \leq \frac{\lambda(l_3 + 2\beta_*\gamma_3)}{1 - L_*(\lambda)} \cdot \frac{\varepsilon}{q_*} = \varepsilon.$$

Thus, we get that for each $x(\cdot) \in X_{p, r}$ there exists $z(\cdot) \in X_{p_0, r}$ such that the inequality

$$\|x(\cdot) - z(\cdot)\|_C \leq \varepsilon$$

holds. This yields that

$$X_{p, r} \subset X_{p_0, r} + \varepsilon \cdot B_C(1) \quad (4.8)$$

Analogously, it is possible to show that

$$X_{p_0, r} \subset X_{p, r} + \varepsilon \cdot B_C(1) \quad (4.9)$$

(4.8) and (4.9) complete the proof.

From Theorem 4.1 it follows that for each fixed $r \in [0, r_* + \beta_2]$ the set valued map $p \rightarrow X_{p, r}$, $p \in (p_* - \beta_1, p_* + \beta_1)$, is continuous.

Theorem 4.1 implies the validity of the following corollary.

Corollary 4.1. Let $r \in [0, r_* + \beta_2]$ and $p_0 \in (p_* - \beta_1, p_* + \beta_1)$ be fixed. Then for every $\varepsilon > 0$ there exists $\delta = \delta(\varepsilon, p_0, r) > 0$ such that for every $p \in (p_0 - \delta, p_0 + \delta)$ the inequality

$$h_C(X_{p, r}(t), X_{p_0, r}(t)) \leq \varepsilon$$

is verified for every $t \in [a, b]$ where the set $X_{p, r}(t)$ is defined by (2.7).

5. Robustness of the Trajectories with Respect to the Remaining Control Resource

In this section we study the robustness of a trajectory with respect to the remaining control resource consumption.

Theorem 5.1 Let $\varepsilon > 0$ be a given number, $x(\cdot) \in X_{p, r}$ be a trajectory of the system (2.1) generated by the control function $u(\cdot) \in U_{p, r}$ such that $\|u(\cdot)\|_p = r_0 < r$, $\Omega_* \subset [a, b]$ be a Lebesgue measurable set, the control function $u_0(\cdot): [a, b] \rightarrow R^m$ be defined

$$u_0(s) = \begin{cases} u(s) & \text{if } s \in [a, b] \setminus \Omega_*, \\ v(s) & \text{if } s \in \Omega_*. \end{cases} \quad (5.1)$$

such that $\|u_0(\cdot)\|_p = r$ and let $x_0(\cdot) \in X_{p, r}$ be a trajectory of the system (2.1) generated by the control function $u_0(\cdot) \in U_{p, r}$. If

$$\mu(\Omega_*) \leq \left[\frac{1 - L_*(\lambda)}{2\lambda r(l_3 + 2\beta_*\gamma_3)} \cdot \varepsilon \right]^{\frac{p}{p-1}}, \quad (5.2)$$

then the inequality

$$\|x(\cdot) - x_0(\cdot)\|_C \leq \varepsilon$$

is held where $L_*(\lambda)$ and $\beta_* > 0$ are defined by (2.4) and (2.6) respectively, $\mu(\Omega_*)$ denotes the Lebesgue measure of the set Ω_* .

Proof. (2.1), (2.4), (2.6), (5.1), Proposition 2.1, condition 2.B, the inclusions $u(\cdot) \in U_{p,r}$, $u_0(\cdot) \in U_{p,r}$ and Hölder's inequality imply that

$$\begin{aligned} & \|x(t) - x_0(t)\| \leq l_0 \|x(t) - x_0(t)\| \\ & + \lambda \int_a^b [l_2 + \gamma_2(\|u(s)\| + \|u_0(s)\|)] \\ & \quad \cdot \|x(s) - x_0(s)\| ds \\ & + \lambda \int_a^b [l_3 + \gamma_3(\|x(s)\| + \|x_0(s)\|)] \\ & \quad \cdot \|u(s) - u_0(s)\| ds \\ & \leq l_0 \|x(\cdot) - x_0(\cdot)\|_C \\ & + \lambda \int_a^b [l_2 + \gamma_2(\|u(s)\| + \|u_0(s)\|)] ds \\ & \quad \cdot \|x(\cdot) - x_0(\cdot)\|_C \\ & + \lambda(l_3 + 2\beta_*\gamma_3) \int_{\Omega_*} \|u(s) - u_0(s)\| ds \\ & \leq l_0 \|x(\cdot) - x_0(\cdot)\|_C + (L_*(\lambda) - l_0) \|x(\cdot) - x_0(\cdot)\|_C \\ & + 2\lambda r(l_3 + 2\beta_*\gamma_3) [\mu(\Omega_*)]^{\frac{p-1}{p}} \\ & = L_*(\lambda) \cdot \|x(\cdot) - x_0(\cdot)\|_C \\ & + 2\lambda r(l_3 + 2\beta_*\gamma_3) [\mu(\Omega_*)]^{\frac{p-1}{p}} \end{aligned}$$

for every $t \in [a, b]$. The last inequality, (2.5) and (5.2) imply

$$\|x(\cdot) - x_0(\cdot)\|_C \leq \frac{2\lambda r(l_3 + 2\beta_*\gamma_3)}{1 - L_*(\lambda)} [\mu(\Omega_*)]^{\frac{p-1}{p}} \leq \varepsilon.$$

The proof of the theorem is completed.

Theorem 5.1 shows that full consumption of the remaining control resource on the domain with sufficiently small measure causes small deviation of the trajectory.

Denote

$$U_{p,r}^* = \{u(\cdot) \in L_p([a, b]; R^m) : \|u(\cdot)\|_p = r\}$$

and let $X_{p,r}^*$ be the set of trajectories of the system (2.1) generated by the control functions $u(\cdot) \in U_{p,r}^*$.

For fixed $t \in [a, b]$ we set

$$X_{p,r}^*(t) = \{x(t) \in R^n : x(\cdot) \in X_{p,r}^*\}. \quad (5.3)$$

Theorem 5.2. The equality $cl(X_{p,r}) = cl(X_{p,r}^*)$ is satisfied where cl denotes the closure of a set.

Proof. Since $X_{p,r}^* \subset X_{p,r}$, then we have

$$cl(X_{p,r}^*) \subset cl(X_{p,r}). \quad (5.4)$$

Let $x_*(\cdot) \in X_{p,r}$ be an arbitrarily chosen trajectory of the system (2.1) generated by the control function $u_*(\cdot) \in U_{p,r}$ where $\|u_*(\cdot)\|_p = r_* < r$. Now we choose an arbitrary $\delta > 0$ and the Lebesgue measurable set $V_* \subset [a, b]$ such that

$$\mu(V_*) \leq \left[\frac{1 - L_*(\lambda)}{2\lambda r(l_3 + 2\beta_*\gamma_3)} \delta \right]^{\frac{p}{p-1}} \quad (5.5)$$

where $L_*(\lambda)$ is defined by (2.4), β_* is defined by (2.6). Assume that $\int_{[a,b] \setminus V_*} \|u_*(s)\|^p ds = r_1^p$. Define new control function $w_*(\cdot) : [a, b] \rightarrow R^m$ setting

$$w_*(s) = \begin{cases} u_*(s) & \text{if } s \in [a, b] \setminus V_* \\ \left[\frac{r^p - r_1^p}{\mu(V_*)} \right]^{\frac{1}{p}} \cdot b_* & \text{if } s \in V_* \end{cases}$$

where $b_* \in R^m$ is an arbitrary vector such that $\|b_*\| = 1$. It is obvious that $\|w_*(\cdot)\|_p = r$, i.e. $w_*(\cdot) \in U_{p,r}^*$. Let $y_*(\cdot)$ be the trajectory of the system (2.1) generated by the control function $w_*(\cdot)$. Then $y_*(\cdot) \in X_{p,r}^*$, and keeping in mind (5.5) we obtain from Theorem 5.1 that $\|x_*(\cdot) - y_*(\cdot)\|_C \leq \delta$. Since $\delta > 0$ is arbitrarily chosen, we have that $x_*(\cdot) \in cl(X_{p,r}^*)$ which implies that $X_{p,r} \subset cl(X_{p,r}^*)$, and hence

$$cl(X_{p,r}) \subset cl(X_{p,r}^*) \quad (5.6)$$

From (5.4) and (5.6) we obtain the proof of the theorem.

The Theorem 5.1 means that every trajectory $x(\cdot) \in X_{p,r}$ can be approximated by the trajectory obtained by full consumption of the control resource.

From Theorem 5.2 it follows the validity of the following corollary.

Corollary 5.1. The equality

$$cl \left(X_{p,r}(t) \right) = cl \left(X_{p,r}^*(t) \right)$$

is satisfied for every $t \in [a, b]$ where the set $X_{p,r}(t)$ is defined by (2.7), the set $X_{p,r}^*(t)$ is defined by (5.3).

Author's Contributions

Anar Huseyin: Drafted and wrote the manuscript, performed the proofs and result analysis.

Ethics

There are no ethical issues after the publication of this manuscript.

References

- [1]. Aubin, J-P, Frankowska, H. Set Valued Analysis. Birkhauser: Boston, USA, 1990, pp 461.
- [2]. Brauer, F. 1975. On a nonlinear integral equation for population growth problems. *SIAM J. Math. Anal.*; 69: 312-317.
- [3]. Conti, R. Problemi di Controllo e di Controllo Ottimale. UTET: Torino, Italy, 1974, pp 239.
- [4]. Deimling, K. Multivalued Differential Equations. Walter de Gruyter: Berlin, Germany, 1992, pp 260.
- [5]. Guseinov, KG, Nazlipinar AS. 2007. On the continuity property of L_p balls and an application. *J. Math. Anal. Appl.*; 335: 1347-1359.
- [6]. Gusev, MI, Zykov, IV. 2017. On extremal properties of the boundary points of reachable sets for control systems with integral constraints. *Tr. Inst. Math. Mekh. UrO RAN*; 23: 103-115.
- [7]. Heisenberg, W. Physics and Philosophy. The Revolution in Modern Science. George Allen & Unwin: London, Great Britain, 1958, pp 176.
- [8]. Huseyin, A. 2017. On the existence of ε -optimal trajectories of the control systems with constrained control resources. *Commun. Fac. Sci. Univ. Ank. Ser. A1 Math. Stat.*; 66: 75-84.
- [9]. Huseyin, N, Guseinov, KG, Ushakov, VN. 2015. Approximate construction of the set of trajectories of the control system described by a Volterra integral equation. *Math. Nachr.*; 288(16): 1891-1899.
- [10]. Huseyin, N, Huseyin, A, Guseinov KG. 2018. Approximation of the set of trajectories of the nonlinear control system with limited control resources. *Math. Model. Anal.*; 23(1): 152-166.
- [11]. Huseyin, N. 2020. On the properties of the set of p-integrable trajectories of the control system with limited control resources. *Internat. J. Control*; 93(8): 1810-1816.
- [12]. Ibragimov, G, Alias, IA, Waziri, U, Jafaaru, AB. 2019. Differential game of optimal pursuit for an infinite system of differential equations. *Bull. Malaysian Math. Sci. Soc.*; 42(1): 391-403.
- [13]. Kalman, RE. 1963. Mathematical description of linear dynamical systems. *J. SIAM Control Ser. A*; 1: 152-192.
- [14]. Kelley, JL. General Topology. Springer: New York, USA, 1975, pp 298.
- [15]. Krasovskii, NN. Theory of Control of Motion. Linear Systems. Nauka: Moscow, USSR, 1968, pp 475.
- [16]. Krasovskii, NN, Subbotin, AI. Game-Theoretical Control Problems. Springer-Verlag: New York, USA, 1988, pp 517.
- [17]. Krasnoselskii, MA, Krein, SG. 1955. On the principle of averaging in nonlinear mechanics. *Uspekhi Mat. Nauk*; 10: 147-153.
- [18]. Kostousova, EK. 2020. On the polyhedral estimation of reachable sets in the "extended" space for multistage systems with uncertain matrices and integral constraints. *Tr. Inst. Mat. Mekh*; 26(1), 141-155.
- [19]. Polyanin, AD, Manzhirov, AV. Handbook of Integral Equation. CRC Press: Boca Raton, FL, USA, 1998, pp 1108.
- [20]. Pontryagin, LS, Boltyanskii, VG, Gamkrelidze, RV, Mishchenko, EF. The Mathematical Theory of Optimal Processes. John Wiley & Sons: New York, USA, 1962, pp 360.
- [21]. Subbotin, AI, Ushakov, VN. 1975. Alternative for an encounter-evasion differential game with integral constraints on the players' controls. *J. Appl. Math. Mech.*; 39(3): 367-375.
- [22]. Subbotina, NN, Subbotin, AI. 1975. Alternative for the encounter-evasion differential game with constraints on the momenta of the players controls. *J. Appl. Math. Mech.*; 39(3): 376-385.
- [23]. Ukhobotov, VI, Izmetev, IV. 2018. Impulse differential game with a mixed constraint on the choice of the control of the first player. *Tr. Inst. Math. Mekh. UrO RAN*; 24(1): 209-222.
- [24]. Urysohn, PS. 1923. On a type of nonlinear integral equation. *Mat. Sb*; 31: 236-255.

An Occupational Safety Fuzzy Risk Analysis: An Application in a Building Construction Sites

Orhan Engin^{1*} , Raife Canlar Durmaz¹ 

¹ Konya Technical University, Industrial Engineering Department, Selçuklu, Konya, Türkiye

*orhanengin@yahoo.com

* Orcid: 0000-0002-7250-0317

Received: 1 December 2022

Accepted: 6 June 2023

DOI: 10.18466/cbayarfbe.1213357

Abstract

Employers should be creating a safe workplace environment in working life. A safe working environment is one where risks are eliminated or at an acceptable level. Building works is one of the areas where occupational accidents are most intense today. In this study, fuzzy logic is proposed to determine the risk levels with linguistic words in risk analysis, which is the most important step of the occupational health management system in the building works. In the fuzzy risk assessment, the fuzzy model was first proposed and then the risk numbers were calculated. In the research, a risk assessment was carried out using fuzzy logic method in a construction site consisting of ten blocks and twelve-storey apartments belonging to a building company. In the fuzzy risk assessment, the fuzzification of the input data, the creation of the member functions of the input and output values, and the fuzzification processes were done with the help of the fuzzy logic toolbox of the MATLAB software program. The results showed that fuzzy risk analysis is effective and credible for creating a safe building site.

Keywords: Fuzzy Logic, Occupational Safety, Risk Analysis, Building sector.

1. Introduction

At the construction site, there are a lot of occupational safety risks. The metric methods are used to assess the risks of the workers but at the construction sites, there are a lot of uncertain conditions for workers. Occupational safety is a serious problem at construction sites such as industrial areas. For these uncertainties conditions, fuzzy sets are used to define the risk to workers.

There are a few studies on fuzzy risk analysis in the literature. These are given below; Güranlı and Müngen[1] proposed a fuzzy risk assessment for the construction site. They made a case study on a tunnel project. Morote and Vila [2] presented a risk assessment methodology based on the fuzzy sets theory and the analytic hierarchy process. They applied the proposed method to the rehabilitation project of a building. Liu et al.[3] presented a comprehensive overview of currently known applications of computing with words in risk assessment. They suggested five categories for risk assessment. These are risk assessment based on fuzzy numbers; fuzzy rule-based risk assessment; fuzzy extension of typical probabilistic risk assessment; sequential linguistic approach to risk assessment.

Lin et al.[4] proposed an integrated quantitative risk assessment method. They employed this method of influence diagram and fuzzy theory to estimate accident probability and to deal with the imprecision inherent to the process of subjective judgment. They made a case study on the construction industry. Shiliang et al.[5] proposed an analytic hierarchy process-fuzzy comprehensive evaluation method for as risk of falling from height for the research object. Zhou et al.[6] used quality function deployment, fuzzy analytic network process, fuzzy failure modes, and effect analysis to identify the types and causes of hazards in the construction industry providing risk assessment values of hazard causes and relevant improvement strategies. They made a case study on a hydroelectric project. Ardeshir et al. [7], in water conveyance tunnels, they applied an analytical hierarchy process to estimate the importance of each criterion and calculate the significance of the overall impact of the risk. Debnath et al.[8] developed a Takagi-Sugeno type fuzzy inference system for assessing occupational risks in construction sites. They used an analytical hierarchy process for evaluating the safety levels of each type of injury-prone body part. Seker and Zavadskas [9] used the Fuzzy Decision Making Trial and Evaluation Laboratory (DEMATEL) method by a cause-effect diagram on

construction sites for analyzing occupational risks. Also, they made a sensitivity analysis. Amiri et al. [10] proposed a fuzzy probability model based on fuzzy risk-based statistical data mining analyzes of accident databases, together with a detailed literature review. They tested the model on four construction case studies. Biswas and Zaman [11] proposed a methodology for construction project risk assessment under epistemic uncertainty. Their methodology used a triangular fuzzy numbering system to compute risk value by combining expert's opinions and insufficient historical data. Also, they used VIKOR method for risk ranking. They applied their proposed a project of a building and a rehabilitation project of a building. Sadeghi et al.[12] developed an Ensemble Predictive Safety Risk Assessment Model based on the integration of neural networks with fuzzy inference systems. Then, they applied this model which they developed to several Malaysian construction case projects. Topal et al.[13] applied the risk assessment model for small-scale construction sites. In their work, they used the insights of safety experts, checklists for the likelihood of accidents, defining safety levels, severity of risk, and safety barriers.

According to the 2020 work accidents and occupational diseases statistics in Turkey, the numbers of deaths due to work accident for all sectors are 1231 persons. Moreover, the numbers of death at building construction sites are 297 persons. Also, the number of death at building construction sites rate is 24.12 % in all sectors in 2020[14]. At present, building construction sites are the most dangerous sector after mining in our country. In this study, a fuzzy risk analysis has been made which has twelve story apartment houses with ten blocks of a building site. The results showed that the fuzzy risk analysis is effective and believable.

The rest of the paper is organized as follows; an occupational safety risk analysis is explained in section 2. In Section 3, the fuzzy risk analysis is defined. The case study is given in Section 4. The results are discussed in Section 5-Conclusion.

2. An Occupational Safety Risk Analysis

Organizations should implement the occupational health and safety system. They should protect their employees, subcontractors, and all persons in the organization against work accidents and occupational diseases. In our and other many countries in the world, implementing this system is a principle in the law. The occupational risks are estimated and the workers should be protected from these risks. Hazard and risk are often used interchangeably but these terms are different from each other. Hazard is defined as a potential source of damage, harm or adverse health effect on something or a person in the work environment under certain conditions. Risk means, the likelihood of a hazard. Risk

assessment is the process of identifying hazards, analyzing the risk associated with those hazards, and determining appropriate ways to control the hazard and reduce the risk.

The risk analyses are classified into three categories. These are defined as qualitative, quantitative, and hybrid techniques. In quantitative techniques, the risks are estimated by statistical, simulations, and other mathematical methods. The risks are defined by numerical results but in qualitative techniques, the risks are estimated through judgment, ranking options, and other descriptive analyses. Also, the hybrid technique mixes both quantitative and qualitative [15]. The fuzzy risk analysis is a qualitative method. Some of the methodologies available in the literature for risk analysis are given as follows;

- Failure mode and effects analysis,
- Safety audit,
- Cause-Consequence diagrams,
- Preliminary hazard analysis,
- Kinney method,
- Machine risk assessment,
- Safety function analysis,
- Fault-tree analysis,
- Event-tree analysis,
- Bow-tie,
- Hazard and operability study,
- Job safety analysis,
- Preliminary risk analysis,
- Human error identification,
- Human reliability assessment,
- Deviation analysis,
- Management oversight and risk tree,
- Barrier diagram,
- Risk assessment decision matrix.

The failure mode and effect analysis (FMEA) is a method that is commonly used in occupational safety management. FMEA is a method developed to identify all potential failures in a product or service step by step. The steps of the FMEA are given below;

- Step 1.* The process is reviewed,
- Step 2.* The potential effects of failure are listed,
- Step 3.* The severity rankings are assigned,
- Step 4.* The probability of occurrence ranking is assigned,
- Step 5.* The detection rankings are assigned,
- Step 6.* The risk priority numbers are calculated,
- Step 7.* The action plan is developed.

By using FMEA the risk priority number (RPN) is calculated in multiples of three rankings. These are severity ranking (S), probability of occurrence ranking (O), and detection ranking (D). Each ranking is assigned a value in the range from 1 to 5 and the RPN is calculated which is shown in Equation 2.1.

$$RPN = S \times O \times D \quad (2.1)$$

A few studies on risk analysis in the literature are; Hong et al.[16] analyzed the risks that would arise when using an earth pressure balanced type tunnel boring machine in underwater tunnel excavation. An event tree analysis was applied to quantify the risks during the preliminary design phase of the tunnel. Anbari et al.[17] conducted 30 interviews with safety and health professionals and risk management personnel working in the construction industry in Oman. They analyzed 151 responses.

3. Fuzzy Risk Analysis

The fuzzy theory based on fuzzy sets was first developed by Zadeh [18]. A crisp set is defined to be either one or zero. To represent the intensity, in their study, Zadeh used a membership function [19].

In the occupational safety system, risk assessment techniques are very important. At the construction sites and industrial areas, the risk analysis problems contain quantitative and qualitative data; for qualitative data, the fuzzy method should be used for the risk analysis problems.

The fuzzy theory has been applied to different areas such as occupational safety risk analysis. In this study, risk priority numbers are calculated using linguistic terms. The inputs, severity, probability of occurrence and detection of the failure are described as linguistic variables. To fuzzify these inputs, the membership functions are used. The fuzzy risk analysis method is given in Figure 1 [1].

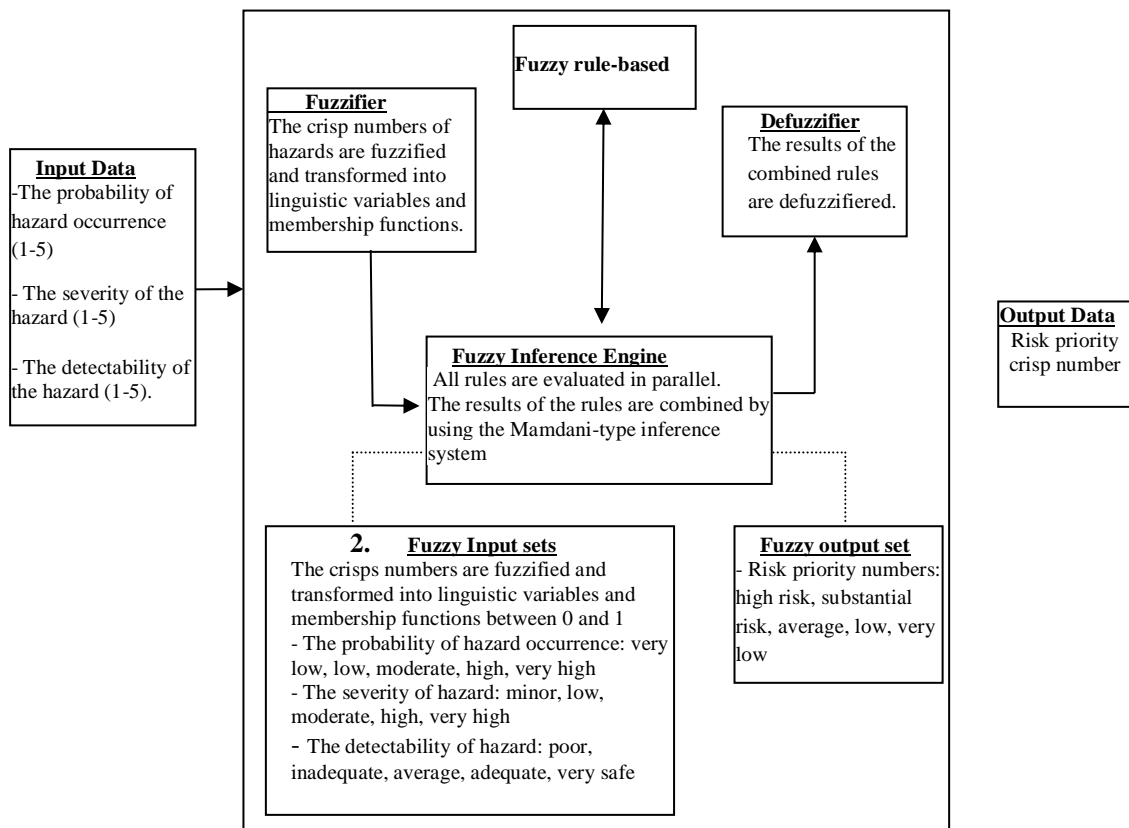


Figure 1. Fuzzy risk analysis model [1].

4. Case Study

At a twelve-story apartment house with ten blocks of building construction sites, risk assessment has been made using fuzzy theory. The activities at the building construction sites are determined by a decision-making group that consists of twenty decision-makers (civil, machine, industrial, electric, and electronic engineers; architecture, chiefs of workers, and workers) from the building construction sites. The twenty-nine activities are determined. Also, the one hundred ninety-eight risks

are determined by the decision-making group. The input and output values are defined in the fuzzy set.

The experts assign these parameters as fuzzy variables. The steps of the fuzzy risk analysis and used method are given in Figure 2. MATLAB is used to obtain the results of fuzzy risk analysis. The first step of the risk assessment is to define the input values. In this study, three input variables are used. These are severity, probability of occurrence, and detectability. Each of the input metrics is defined on a scale of rank. The severity scale of rank is given in Table 1.

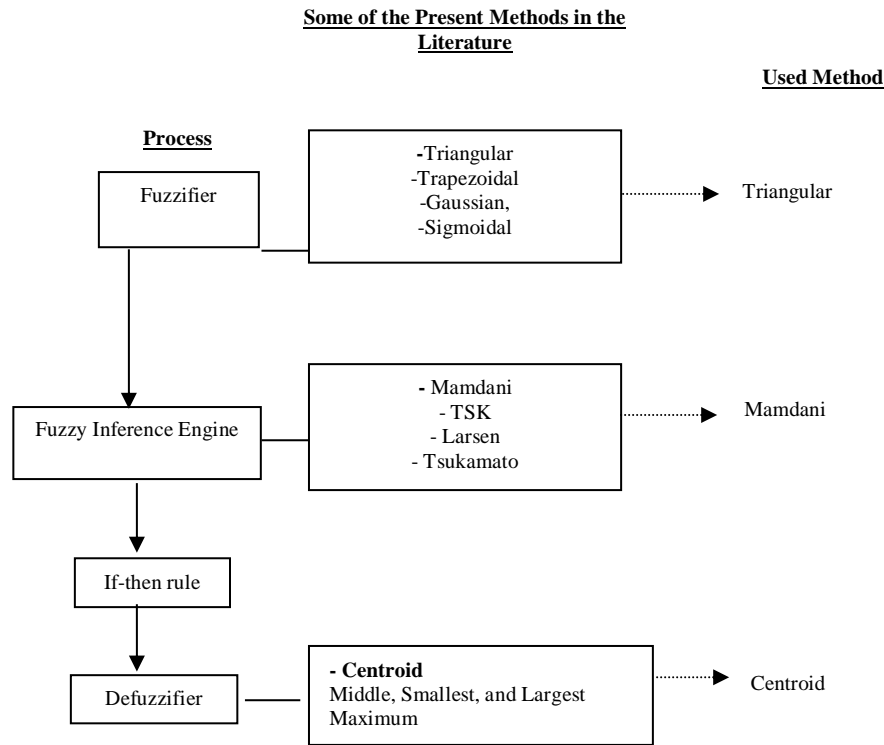


Figure 2. Steps of the Fuzzy risk

The detectability scale of rank is given in Table 3.

Table 1. The severity scale of hazard rank

The severity of the hazard	Linguistic variables	Rank
The danger of death, permanent incapacity	Very High	5
Major injury (Permanent disability, low-loss, occupational disease)	High	4
Requires inpatient treatment, but leaves a lasting impression on accidents that require clinical treatment	Moderate	3
Minor injury (Requiring outpatient)	Low	2
Do not have wounding, a simple accident	Minor	1

Table 3.The detectability scale of hazard rank

The detectability of hazard	Linguistic variables	Rank
The measures taken were unavoidable dangers	Poor	5
It is hard to prevent accidents with measures taken	Inadequate	4
The possibility of accident prevention is low with measures taken	Average	3
The possibility of accident prevention is high with measures taken	Adequate	2
The accident is exactly prevented with measures taken	Very safe	1

The probability of occurrence rank is given in Table 2.

Table 2. The probability of hazard occurrence rank

Probability	Linguistic variables	Rank
Every day (Very high probability)	Very high	5
Once a week (high probability)	High	4
Once a month (moderate probability)	Moderate	3
Once every three months (low probability)	Low	2
Once a year (very low probability)	Very low	1

Then, these three input variables are fuzzified using membership functions provided by experts [20]. The triangular membership function (TMF) is used for the input variables. The fuzzy membership functions (FMF) of the probability of occurrence, severity, and detectability are given in Figure 3-5.

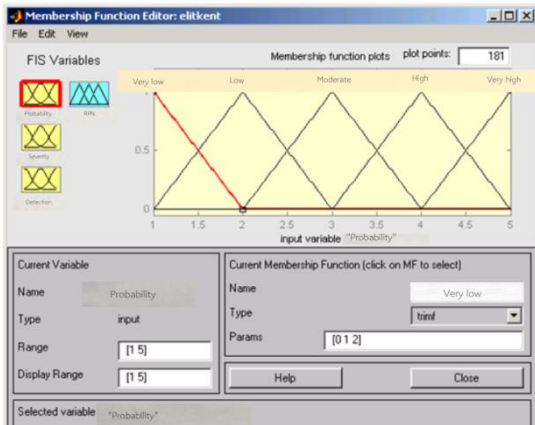


Figure 3. FMF of the probability of occurrence



Figure 4. Fuzzy membership functions of severity

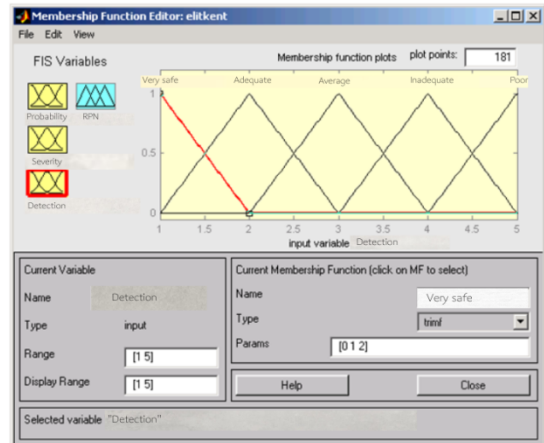


Figure 5. FMF of detectability

Table 4. The fuzzy risk priority number

FRPN	The hazard knowledge	Rank
High Risk	Catastrophic Event: hazard could cause serious injury or death	5
Substantial Risk	Major Event: hazard could cause injury	4
Average Risk	Moderate Event: hazard could cause some problems	3
Low Risk	Minor Event: hazard could cause some minor problem	2
Very Low Risk	Noticeable Event: hazard would not be the noticeable problem.	1

Fuzzy inputs are evaluated using linguistic rule base and fuzzy logic operations. The membership function of the fuzzy risk priority number is given in Figure 6.

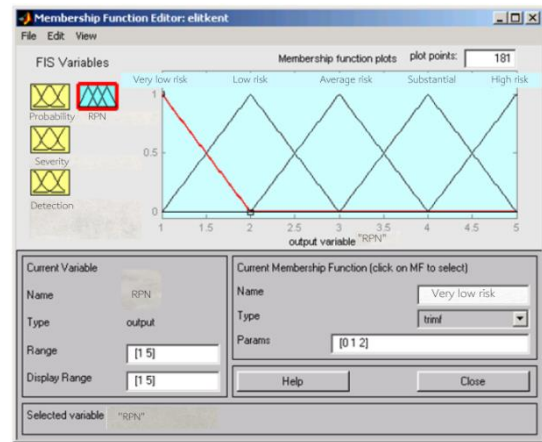


Figure 6. The membership function of the fuzzy risk priority number

In the model, one hundred twenty-five rules were created. The three of these rules are given below as an example.

- If (probability is very low) and (severity is high) and (detectability is very safe) then RPN is substantial risk.
- If (probability is low) and (severity is minor) and (detectability is very safe) then RPN is very low risk.
- If (probability is high) and (severity is minor) and (detectability is very safe) then RPN is very low risk.

The graphical illustrations of these rules are given in Figure 7.

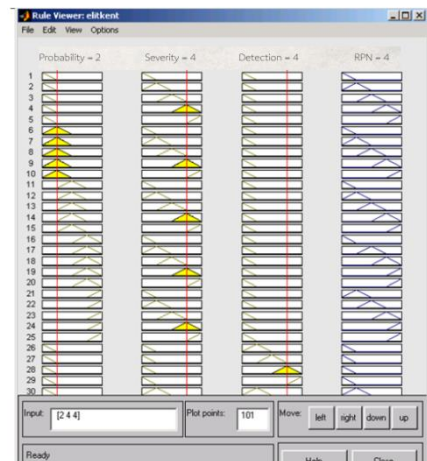


Figure 7. The graphical illustrations of these rules

Figure 7 shows that "Due to the lack of regular loading on the earthmoving truck", The probability 2, severity 4, and detectability 4 for the danger of "overturning the truck" The program output of the RPN value is calculated as 4.

The surface viewer of the output is given in Figure 8.

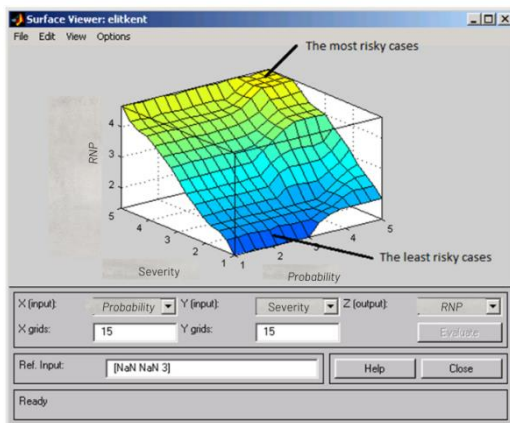


Figure 8. The surface viewer of output

In this study, the RPN determined as a result of fuzzy risk assessment is compared with the data obtained in the FMEA method. For comparing the results, an example is given below.

For example;

During the process of "Preparation of Wooden Mold"

If we make a risk assessment with the FMEA technique for the dangers of "Mold collapse" and "Hand, foot, finger jamming during the mold process", the calculations do as follows.

For the danger of "mold collapse"; the RPN is calculated as follows.

$RPN = 2 \times 5 \times 2 = 20$ (Probability 2, Severity 5, detectability 2).

For the danger of "Hand, foot, finger jamming during the mold process" the RPN is calculated as follows.

$RPN = 3 \times 3 \times 3 = 27$ (Probability 3, Severity 3, detectability 3).

Whereas, the RPN values for the danger of "mold collapse" should be higher score than the RPN values for the danger of "Hand, foot, finger jamming during the mold process" but with the results of the FMEA technique are found exactly the opposite.

However, as a result of the fuzzy risk assessment made in this study, for the danger of "mold collapse"; the RPN was calculated, 4.68 and for the danger of "Hand, foot, finger jamming during the mold process" the RPN was calculated, 3.

5. Conclusion

In this study, a fuzzy risk analysis method is used at building construction sites, with twelve floors and ten blocks twenty main activities. The activities at the building construction sites are determined by a decision-making group. This group determined one hundred ninety-eight risks at the building construction sites. MATLAB software program fuzzy logic toolbox is used to obtain the results of fuzzy risk analysis. The fuzzy risk priority numbers are evaluated using a linguistic rule base. In the model, three inputs, one output and one hundred twenty-five rules were created. Triangular Membership functions, Mamdani inference and centroid rinsing method were used. When the Risk Priority Numbers determined as a result of fuzzy risk assessment are compared with the data obtained in the FMEA method, it is seen that the fuzzy logic method is more appears to give accurate and logical results. According to the fuzzy risk assessment, some of the most important risks that RPN values were found 4.68 are a man in the excavation pit fall, falling of worker over the mold, mold collapse, an employee falling from scaffold, crane overturn, electric shock, and wall overturn.

Occupational safety risks are very high in construction sites and occupational safety in construction sites is a serious problem in Turkey as well as in the world.

The fuzzy risk analysis is an effective and believable method for preventing job accident and occupational diseases at building construction sites.

For further research, several extensions of ordinary fuzzy sets multi-criteria methodology can be used to prevent job accidents and occupational diseases at building construction sites.

Acknowledgement

The authors thank the anonymous reviewers for their contribution to this paper.

Author's Contributions

Orhan Engin: Supervision, Methodology, Validation, Writing-original draft, Investigation

Raife Canlar Durmaz: Methodology, Data curation, Writing original draft, Visualization, Investigation, Software.

Ethics

There are no ethical issues after the publication of this manuscript.

References

- [1].Gürcanlı G. E., Müngen U.2009. An occupational safety risk analysis method at construction sites using fuzzy sets, *International Journal of Industrial Ergonomics*; 39:371–387.
- [2].Morote A. N., Vila F. R. 2011. A fuzzy approach to construction project risk assessment. *International Journal of Project Management*; 29(2) 220- 231.
- [3].Liu J., Martínez L., Wang H., Rodríguez R. M., Novozhilov V. 2010. Computing with Words in Risk Assessment, *International Journal of Computational Intelligence Systems*; 3(4) 396-419.
- [4].Lin Y.H., Lin C.C., Tyan Y.Y. 2011. An Integrated Quantitative Risk Analysis Method for Major Construction Accidents Using Fuzzy Concepts and Influence Diagram, *Journal of Marine Science and Technology*; 19 (4) 383-391.
- [5].Shiliang S., Min J., Yong L., Runqiu L. 2012. Risk assessment on falling from height based on AHP-fuzzy, *Procedia Engineering* 45: 112 – 118.
- [6].Zhou J.L., Hua B. Z., Sun Z.Y. 2013. Safety Assessment of High-Risk Operations in Hydroelectric-Project Based on Accidents Analysis, SEM, and ANP, *Mathematical Problems in Engineering*, Article ID 530198, 12 pages.
- [7].Ardeshir A., Amiri M., Ghasemi Y., Errington M. 2014. Risk assessment of construction projects for water conveyance tunnels using fuzzy fault tree analysis, *International Journal of Civil Engineering*, Transaction A: *Civil Engineering*, 12 (4) 396- 412.
- [8].Debnath, J., Biswas, A. Sivan, P., Sen K. N., Sahu S. 2016. Fuzzy inference model for assessing occupational risks in construction Sites; *International Journal of Industrial Ergonomics* 55, 114- 128.
- [9].Seker S., Zavadskas E. K. 2017. Application of Fuzzy DEMATEL Method for Analyzing Occupational Risks on Construction Sites, *Sustainability*; 9, 2083.
- [10].Amiri, M., Ardeshir, A., Zarandi, M. H. F.2017. Fuzzy probabilistic expert system for occupational hazard assessment in construction, *Safety Science* 93, 16–28.
- [11].Biswas T. K. Zaman K.2019. A Fuzzy-Based Risk Assessment Methodology for Construction Projects Under Epistemic Uncertainty, *Int. J. Fuzzy Syst.* 21(4):1221–1240.
- [12].Sadeghi, H., Mohandes , S. R., Hosseini, M. R., Banihashemi , S. , Mahdiyar A., Abdullah A. 2020. Developing an Ensemble Predictive Safety Risk Assessment Model: Case of Malaysian Construction Projects, *Int. J. Environ. Res. Public Health.* 17, 8395
- [13].Topal, S., Atasoylu, E. 2022. A Fuzzy Risk Assessment Model for Small Scale Construction Work. *Sustainability* 2022, 14, 4442.
- [14].Anonymous, 2022. Social Security Institution, http://eski.sgk.gov.tr/wps/portal/sgk/tr/kurumsal/istatistik/sgk_istatistik_villiklari.
- [15].Marhavilas P., Koulouriotis D., Mitrakas C. 2014, Fault and Event-Tree Techniques in Occupational Health-Safety Systems – Part I: Integrated Risk-Evaluation Scheme, *Environmental Engineering and Management Journal*, 13 (8) 2097-2108.
- [16].Hong E. S., Lee I.M., Shin H.S., Nam S. W., Kong J.S. 2009 Quantitative risk evaluation based on event tree analysis technique: Application to the design of shield TBM, *Tunnelling and Underground Space Technology* 24 : 269–277.
- [17].Anbari S. A., Khalina A., Alnuaimi A., Normariah A.,Yahya A. 2013 Safety and Health Risk Assessment at Oman Building Construction Projects, *IJRET: International Journal of Research in Engineering and Technology*, 02 (02) 571-578.
- [18].Engin, O., Yilmaz, M. K. 2022. A fuzzy logic based methodology for multi-objective hybrid flow shop scheduling with multi-processor tasks problems and solving with an efficient genetic algorithm. *Journal of Intelligent & Fuzzy Systems*; 42: 451- 463.
- [19].Sarucan, A., Baysal, M. E., Engin, O. 2022. A spherical fuzzy TOPSIS method for solving the physician selection problem. *Journal of Intelligent & Fuzzy Systems*; 42: 181- 194.
- [20].Kahraman C. Kaya I., Şenvar Ö. 2013. Healthcare Failure Mode and Effects Analysis Under Fuzziness, *Human and Ecological Risk Assessment* 19, 538- 552.

Noise-Robust Spoofed Speech Detection Using Discriminative Autoencoder

Gökay Dişken^{1*} , Zekeriya Tüfekçi¹ 

¹ Adana Alparslan Türkeş Science and Technology University, Department of Electrical-Electronics Engineering, Adana, Türkiye

² Çukurova University, Department of Computer Engineering, Adana, Türkiye

* gdisken@atu.edu.tr

* Orcid: 0000-0002-8680-0636

Received: 20 June 2022

Accepted: 8 June 2023

DOI: 10.18466/cbayarfbe.1132319

Abstract

Audio spoof detection gained the attention of the researchers recently, as it is vital to detect spoofed speech for automatic speaker recognition systems. Publicly available datasets also accelerated the studies in this area. Many different features and classifiers have been proposed to overcome the spoofed speech detection problem, and some of them achieved considerably high performances. However, under additive noise, the spoof detection performance drops rapidly. On the other hand, the number of studies about robust spoofed speech detection is very limited. The problem becomes more interesting as the conventional speech enhancement methods reportedly performed worse than no enhancement. In this work, i-vectors are used for spoof detection, and discriminative denoising autoencoder (DAE) network is used to obtain enhanced (clean) i-vectors from their noisy counterparts. Once the enhanced i-vectors are obtained, they can be treated as normal i-vectors and can be scored/classified without any modifications in the classifier part. Data from ASVspoof 2015 challenge is used with five different additive noise types, following a similar configuration of previous studies. The DAE is trained in a multicondition manner, using both clean and corrupted i-vectors. Three different noise types at various signal-to-noise ratios are used to create corrupted i-vectors, and two different noise types are used only in the test stage to simulate unknown noise conditions. Experimental results showed that the proposed DAE approach is more effective than the conventional speech enhancement methods.

Keywords: Deep learning, denoising autoencoder, i-vector, spoofing detection

1. Introduction

Vulnerability of automatic speaker detection systems against spoofed speech is an important drawback for practical usage of these systems. Early studies showed that conventional features such as mel-frequency cepstral coefficients (MFCC) are not suitable for detection of synthetic speech signals [1]. Organizations such as the ASVspoof challenges provided a common database to the researches, which accelerates the awareness and number of studies on the spoof detection problem [2–4].

Many different solutions to the aforementioned problem have been proposed. One of the most efficient features against synthetic speech is the constant-Q cepstral coefficients (CQCC) [5], which served as a baseline method with Gaussian Mixture Model (GMM) classifier. Phase-based features, which are usually

neglected in speaker/speech recognition, were found to be beneficial for spoof detection [6], [7]. For modeling/classifying the extracted features traditional methods such as GMMs and i-vectors [3] could be preferred. However, recent studies include deep learning architectures such multilayer perceptron (MLP) [8], convolutional neural networks (CNN) [9], recurrent neural networks (RNN) [10].

Compared to the baseline systems such as MFCC–GMM, most of the mentioned studies achieved superior performances for detecting synthetic and/or replayed speech data. On the other hand, under additive noise, the detection performance drops rapidly as shown in [11] using the ASVspoof 2015 database. Several different feature types were investigated with GMM and i-vector backends, and to reduce the noise effects, conventional speech enhancement methods such as spectral subtraction and Wiener filtering were

employed. However, speech enhancement methods further deteriorate the detection performance. Similar observations were made in [12] for additive noise and reverberation, using MLP classifier, and score level fusion of different features led to an improved performance. Complex deep learning architectures yielded to the most robust systems so far, considering the noisy ASVspoof 2015 database. In [13], a CNN system was examined with different combinations of noise aware training, masking, and RNN. The most robust system was observed with CNN+Mask+RNN combination. In [14], gated recurrent convolutional networks were used with modified group delay features and spectrogram obtained via short-time Fourier Transform. A noise mask was also estimated with a CNN mask estimator, where the purpose is to mask the noise dominant time-frequency bins and use the speech dominant bins in further processes. Identity vectors were observed after stacking the network outputs, and a probabilistic linear discriminant analysis was used for classification.

Despite the various methods proposed so far for spoof detection, studies on robustness against the additive noise are very limited. Conventional speech enhancement methods are ineffective, and the proposed robust deep learning-based systems are computationally demanding. In this work, discriminative denoising autoencoder (DDAE) [15] with i-vector inputs are investigated to verify if it can provide a robust system, or fails as speech enhancement methods did. One of the advantages of the i-vectors is that variable length utterances can be expressed as fixed low dimensional vectors [16]. This property is also important for neural network systems as they require fixed length inputs. For instance, to use the CNN architecture, speech files are truncated or padded to a selected length [9]. Using the i-vectors, the information loss or adding redundant information can be avoided. The DAE networks mainly used for restoring the noisy/corrupted features, and can be found in several speech related studies such as [17], [18]. The original (clean) version of the inputs is given as the DAE targets for training the system. In the discriminative DAE, class labels are also provided so that the network can also learn the differences between classes. Following the previous robustness studies mentioned before, the ASVspoof 2015 database is used in this work with five different noises from NOISEX-92 [19] and QUT-Noise [20] databases. The experimental results proved that the proposed approach is more robust than the conventional speech enhancement methods.

2. Denoising Autoencoders with I-vectors

2.1. I-vector

Text-independent speaker verification enjoyed the advantages of the i-vectors in the last decade. Some of the advantages that i-vector introduced are fixed dimensional representation, modeling both speaker and

channel variabilities in the same space, channel compensation in the i-vector space, opportunity to use support vector machine and linear discriminant analysis based classifiers. The conventional i-vector extraction scheme consists of training a GMM with a high number of mixtures (named as universal background model (UBM)) and a low rank matrix called total variability matrix. Let M be a speaker and channel independent GMM supervector and expressed as,

$$M = m + T\omega \quad (2.1)$$

where m is the mean supervector from the UBM, and ω is a random vector with normal distribution, and T is the total variability matrix (also known as i-vector extractor). For each utterance, maximum a posterior estimate of ω is the i-vector.

Besides their high performances in speaker recognition, i-vectors were also used in spoofed speech detection [21], [22], however their performance is poor under additive noise [11]. Contrary, robust speaker recognition studies can be found in the literature [15], [18], [23]–[27]. The main disadvantages of these methods are the increased computational demand, and poor performance for short duration utterances [27]. The average utterance length for the ASVspoof 2015 data is 3.5 seconds, which is very short even for the clean data. Although the results are not given in this work, preliminary experiments showed that using the MAP denoising methods of [25], [27] do not introduce any robustness to spoof detection system, and the main reason for this result may be the limited amount of training data and their short durations. Therefore, DDAE is used in this work to exploit the nonlinear relation between the noisy and clean i-vectors, and to avoid extreme computational load (as the conventional i-vector extraction framework is followed, and once the DDAE is trained, evaluation is fast as in the typical neural networks). The idea of using i-vectors as the inputs of a neural network was also applied in different speech related areas [17], [28], [29]. Hence, it may be worth exploring a similar approach for synthetic speech detection.

For the classification of the i-vectors, several choices are possible but cosine distance scoring is used in this work due to their higher performances for short durations [16]. Equation 2 shows the cosine distance scoring where the i-vectors of two classes as human (ω_{hum}) and spoof (ω_{spo}) are compared against a test i-vector (ω_{test}), and Equation 3 shows the cosine distance formula.

$$score = \cos(\omega_{hum}, \omega_{test}) - \cos(\omega_{spo}, \omega_{test}) \quad (2.2)$$

$$\cos(\omega_a, \omega_b) = \frac{\langle \omega_a, \omega_b \rangle}{\|\omega_a\| \|\omega_b\|} \quad (2.3)$$

2.2. Discriminative denoising autoencoder

The DDAE used in this work follows the similar architecture of [15]. Different from the DAEs, DDAE network is trained to denoise and classify the inputs at the same time. Therefore, class-specific information will be added to the enhanced features. Another aspect of the DDAE is that there is no assumption on the noise's distribution in the i-vector space [15].

The DDAE consists of two MLPs. The first MLP represents the DAE part, and has two hidden layers with 500 nodes each. Although the details will be given in the experimental setup section, the i-vectors used in this work are 100-dimensional, hence the input of the DDAE. Therefore, the output layer of the first MLP has 100 nodes, as they represent the enhanced i-vectors. Then, those nodes act as the inputs of the second MLP, which also has hidden layer with 500 nodes, and an output layer with two nodes, representing the human and spoof classes. ReLU activation is used after each layer except the last output layer. Similarly, dropout with a 0.5 probability is applied to each layer except the last output.

The first MLP (DAE part) has the mean square error as the cost function as given below,

$$\min MSE = \frac{1}{S} \sum_{i=1}^S \|\omega_i - \hat{\omega}_i\|^2 \quad (2.4)$$

where $\hat{\omega}$ is the enhanced i-vector output, an ω is the target i-vector. S is the total number of training data. It should be noted that the enhanced outputs are taken from the output of the first MLP, before applying dropout or ReLU for the next layer. The cost function of the second MLP is the cross-entropy error between the predicted class and the target class as given in Equation 5,

$$CE = \frac{1}{S} \sum_{i=1}^S \sum_{k=1}^K l_i^k \log(o_i^k) \quad (2.5)$$

where o_i^k is the predicted probability and l_i^k is the ground truth probability of the i th training sample being a member of k th class, respectively. Combining these two cost functions with a suitable weight (i.e. $0 \leq \alpha \leq 1$), a multi-task training can be achieved by minimizing the total cost as shown in Equation 6. The complete architecture is illustrated in Figure 1.

$$\text{Total cost} = \min(1 - \alpha)MSE + \alpha CE \quad (2.6)$$

3. Experiments

3.1. Database description

To examine the robustness of the proposed system, ASVspoof 2015 database is chosen, which consists of synthetic speech attacks. The number of utterances for each partition of the database is given in Table 1.

For the spoofed speech, 10 different attacks are available. Five of those attacks (S1 – S5) are included in every subset, the other five (S6 – S10) are only presented in the evaluation set, hence called unknown attacks. S3, S4, and S10 attacks are based on speech synthesis methods. S3 and S4 share the same underlying algorithm but generated with different amounts of data. S10 is a unit selection-based algorithm and considered the hardest to detect for this database. The other attacks are voice conversion attacks, using different algorithms to enhance diversity. More detailed explanation for each attack type can be found in [4]. The detection performance of unknown attacks (evaluation set) can be related to the generalization capacity of the systems.

For the additive noises, car, babble, and white noises are chosen from NOISEX-92 database, and street and café noises are selected from QUT-NOISE database, following the configurations of the previous robust spoofed speech detection studies [12], [30]. For all of the data, sampling rate is 16 kHz. Also, café and car noise are not included in the training to simulate unseen noise conditions.

Table 1. Partitions of ASVspoof 2015 database

Subset	Number of utterances	
	Human	Spoof
Train	3750	12625
Development	3497	49875
Evaluation	9404	184000

To train the DDAE in a multi-condition manner, a random noise signal (white, babble, or street) is added to the utterances at random SNR levels in the range of 0 dB to 20 dB, with 5 dB steps. While adding the noise, a random starting point is chosen, and a segment equal to the clean signal is extracted. Hence, each clean signal can be considered to be distorted with a unique (to some degree) noise signal. As seen in Table 1, the number of human utterances is less than the spoofed utterances. This may result in an imbalance while training the DDAE. A similar problem is solved by clustering the spoofed i-vectors in [21], where equal error rate (EER) was decreased to 10% from 30.71%. In this work, instead of decreasing the spoof data, human data is corrupted three times while the spoof data is corrupted only one time, following the mentioned process. In the end, a total of 11250 clean-noisy i-vector pairs are created for the human data, and 12625 clean-noisy i-vector pairs are created for the spoof data.

The EER is used as the performance metric, as it is a widely used metric for speaker verification and spoof detection tasks. It defines the operating point where the false acceptance (verifying a spoofed speech) rate and the false rejection (rejecting a genuine speech) rate are equal to each other.

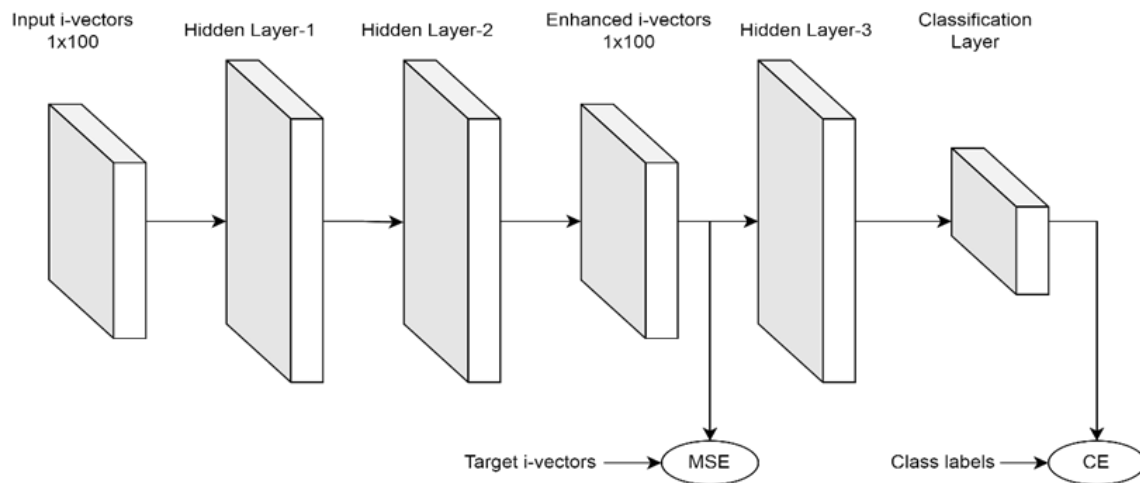


Figure.1: DDAE architecture for denoising the corrupted i-vectors.

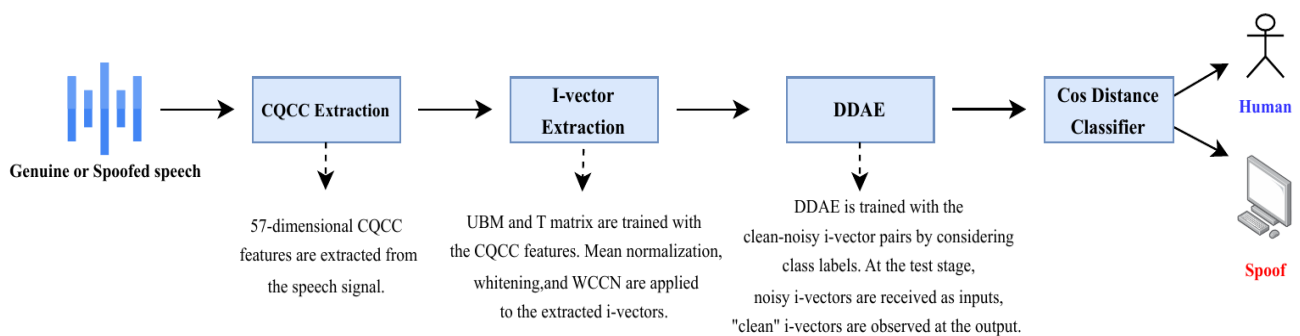


Figure.2: Block diagram of the proposed system.

3.2. CQCC and i-vector extraction

For the feature extraction, the recipe of [3] is followed. 19 -dimensional CQCC features are extracted from utterances, then delta and acceleration coefficients are appended to the static coefficients. A UBM with 64 mixtures is trained using the training partition of ASVspoof 2015 data. Total variability matrix with 100 factors is trained with the same data. After the extraction of the i-vectors, mean normalization, whitening, and within class covariance normalization are applied. To represent human and spoof classes, single i-vectors are obtained by averaging the respective clean i-vectors of each class. Length normalization is also included, which also simplifies the cosine distance scoring to the numerator part of Equation 3.

CQCC extraction is done using the baseline codes provided by the ASVspoof challenge organizers. All i-vector related processes are implemented in MATLAB via MSR Identity Toolbox [31].

3.3. DDAE training

Once the clean-noisy i-vector pairs are obtained, the DDAE can be trained using these pairs and class labels. It is also found that including clean-clean i-vector pairs in the training improved the performance on the clean test data. This may be due to the fact that if the network did not see any clean data while training, it assumes that every input is noisy, hence reduced performance for clean data. Learning rate is chosen as $1e-4$, and Adam optimizer is used. The network is trained for 500 epochs with an early stop option if the training loss does not decrease for 10 epochs. The network related operations (creating the network, training, extracting enhanced i-vectors, testing) are realized with PyTorch. Also, while training the network only two labels (human and spoof) is used, as more labels (indicating different spoof attacks S1 – S5) did not bring any improvements. Python programming language is used for the DDAE training and EER calculations. The DDAE is trained on a GTX 1070 TI GPU.

3.4. Results

Table 2 shows the results for the development set. As expected, the EER increases while the SNR decreases. Besides, the proposed system achieved a good performance for the clean conditions. Similarly, Table 3 shows the results for the evaluation set. Detection performance of the S2 attack was poor compared to the others in both development and evaluation sets. Another interesting result was observed for the S8 attack in clean condition, which produced more EER than the S10 attack. In general S10 attack was considered to be the most detrimental, which is a unit selection-based speech synthesis method [4]. A similar result was also obtained with multi-condition trained CQCC – GMM in [30]. In Table 4, the results of the proposed system are compared with previous studies.

Although it is not possible to make an exact comparison due to the randomness while adding the noise, and also at the training stages, at least a general idea can be developed. Also, instead of analyzing each noise type, SNR level, and spoof attack, only the average values were considered to an excessive table size. Methods selected for the comparison are multi-conditionally trained CQCC – GMM and FBANK – GMM systems of [30]. On average, the results indicated that the proposed DDAE system generally performed better than the multi-conditionally trained GMM systems with a few exceptions such as car noise at 20 dB and 10 dB SNR levels, and street noise at 10 dB and 0 dB SNRs. On the other hand, a more advanced network architecture is necessary to compete with the state-of-the-art system reported in [14].

Table 2. EER (%) results for the development set

Noise Type	SNR (dB)	S1	S2	S3	S4	S5	Average
Clean		0.05	0.36	0.23	0.18	0.28	0.22
Seen Conditions							
Babble	20	11.94	18.82	10.16	10.23	8.67	11.94
	10	24.43	31.55	16.06	16.6	45.64	20.86
	0	37.56	42.66	28.02	28.63	27.39	32.85
White	20	18.68	32.14	16.94	17.34	23.17	21.65
	10	24.26	36.63	21.99	21.64	27.99	26.50
	0	37.12	48.16	26.6	25.95	43.38	36.24
Street	20	12.48	19.54	9.61	9.33	10.41	12.27
	10	23.15	29.57	14.31	14.9	18.58	20.10
	0	35.21	40.4	23.57	23.35	28.01	30.11
Unseen Conditions							
Car	20	0.59	2.42	1.53	1.46	1.03	1.41
	10	2.67	7.11	3.88	3.85	2.44	3.99
	0	8.1	16.06	7.58	7.57	5.83	9.03
Cafe	20	16.88	24.3	14.08	14.31	16.25	17.16
	10	26.35	33.45	21.18	21.56	24.03	25.31
	0	38.24	42.89	34.31	34.11	35.05	36.92

Table 3. EER (%) results for the evaluation set under different noise configurations.

Noise Type	SNR (dB)	S1	S2	S3	S4	S5	S6	S7	S8	S9	S10	Average
Clean		0.09	0.53	0.23	0.18	0.21	0.26	0.13	7.97	0.09	5.12	1.48
Seen Conditions												
Babble	20	13.02	19.99	9.55	9.61	9.12	13.99	9.95	17.27	12.01	23.01	13.75
	10	24.92	31.32	14.48	14.69	15.96	22.42	20.01	20.62	22.89	30.77	21.81
	0	37.45	40.93	26.07	26.19	26.3	32.2	35.37	30.34	36.03	38.45	32.93
White	20	18.26	30.57	15.21	14.93	21.64	27.25	19.81	21.94	19.16	21.74	21.05
	10	24.04	34.38	19.83	19.47	26.21	32.86	24.25	25.89	24.1	25.86	25.67
	0	35.62	44.31	24.7	24.24	40	43.18	37.74	33.63	38.94	31.07	35.34
Street	20	12.84	20.32	9.05	8.77	10.47	14.31	10.46	20.14	14.47	20.63	14.15
	10	23.57	30.12	14.62	14.67	19.12	24.43	18.8	23.53	25.09	27.24	22.12
	0	34.38	39.56	21.48	21.5	27.1	32.88	29.19	28.52	32.82	35.32	30.27
Unseen Conditions												
Car	20	0.57	2.53	1.31	1.18	0.65	0.93	0.33	8.35	0.74	8.01	2.46
	10	2.79	7.79	3.78	3.45	2.08	3.67	2	12.58	3.66	11.94	5.37
	0	9.31	17.72	7.34	7.29	6.08	10.44	7.35	14.99	10.97	19.32	11.08
Cafe	20	16.89	24.63	13.2	13.19	15.72	20.62	13.94	21.96	18.16	24.19	18.25
	10	25.86	32.89	19.9	19.74	23.56	28.76	21.35	25.62	26.4	31.47	25.55
	0	37.68	41.58	32.07	32.46	33.8	37.74	34.12	34.9	36.98	40.45	36.18

Table 4. Comparison of different systems for the evaluation data based on average EER (%) for K=Known, U=Unknown, A=All data.

		Proposed System			CQCC-GMM[30]			FBANK-GMM[30]		
Noise Type	SNR (dB)	K	U	A	K	U	A	K	U	A
Clean		0.24	2.71	1.48	0.1	0.9	0.5	3.2	8.6	5.6
Seen Conditions										
Babble	20	12.25	15.24	13.75	18.2	18.3	18.3	14.5	17.4	16.0
	10	20.27	23.34	21.81	33.9	33.6	33.8	18.1	20.5	19.3
	0	31.38	34.47	32.93	44.6	44.0	44.3	29.6	31.1	30.3
White	20	20.12	21.98	21.05	46.8	44.6	45.7	17.0	19.1	18.0
	10	24.78	26.59	25.67	48.9	48.1	48.5	23.7	24.5	24.1
	0	33.77	36.91	35.34	49.3	48.9	49.1	30.8	31.6	31.2
Street	20	12.29	16.00	14.15	22.7	22.3	22.5	14.5	17.9	16.2
	10	20.42	23.81	22.12	37.5	36.3	36.9	18.7	21.0	19.8
	0	28.80	31.74	30.27	46.1	45.4	45.8	29.1	28.3	28.7
Unseen Conditions										
Car	20	1.24	3.67	2.46	0.9	2.7	1.8	10.2	18.1	14.2
	10	3.97	6.77	5.37	4.3	5.6	4.9	14.3	19.7	17.0
	0	9.54	12.61	11.08	13.0	13.0	13.0	21.6	23.8	22.7
Cafe	20	16.72	19.77	18.25	30.7	30.1	30.4	17.9	20.5	19.2
	10	24.39	26.72	25.55	42.1	41.3	41.7	21.9	23.4	22.6
	0	35.51	36.83	36.18	47.5	47.1	47.3	40.8	38.5	39.6

4. Discussion

The results given in the previous subsection verify that the proposed approach effectively reduced the noise effects. Compared to the multi-conditionally trained systems and conventional speech enhancement methods (which were reported to be even more harmful than no enhancement at all), the DDAE system performed better except for a few cases. On the other hand, a more complex deep learning architecture delivered state-of-the-art performance for the ASVspoof 2015 data and the given noise types.

Analyzing the results, there may be some possible modifications to further increase the performance of the proposed systems. As stated previously, data imbalance can affect the i-vector performance. Although the number of i-vectors for the DDAE training was some sort of balanced due to the augmented human data, the imbalance may have already altered the i-vector extraction process. Therefore, using more balanced data for i-vector extraction could lead to more accurate i-vectors, which may eventually lead to a better trained DDAE system.

Another issue is the short length utterances. As discussed previously, i-vectors are known to be less effective for short durations [18]. Solving this problem may increase the DDAE performance, and also may give the opportunity to use other robust i-vectors frameworks such as [25].

A masking strategy could be developed for the i-vectors. Inspired by the state-of-the-art system, a mask for separating the noise and speech parts may boost the detection performance.

Although the complex gated recurrent convolutional network achieved impressive results, the masking features almost halved the EER [14]. This verifies the importance of masking the noise before the classification occurs. Although the DDAE approach tries to compensate for the corrupted features, including a mask during the training process will likely to increase the performance. Two possible applications of the masking will be investigated in the future works. One of them is using the mask before the i-vector extraction, hence obtaining cleaner i-vectors and use the DDAE for both enhancing and classifying them. The other is applying the mask in the i-vector space, which will require some knowledge or assumption of how the noise signal can be interpreted in the i-vector space (such as the normal distribution assumption in [27]).

As the i-vectors deliver state-of-the-art performances for speaker recognition, using them for spoof detection could be beneficial. Instead of using different systems for spoof detection, speaker recognition, and noise robustness, i-vectors could be used at each stage. At least, i-vectors could be a common part to create a more straight-forward system (combinations of i-vectors – PLDA, i-vectors – DDAE, etc.). As a final note, robust PLDA classifiers can also be achieved with multi-condition training or SNR aware training, whose robustness will be higher than the simple cosine scoring used in this paper. So, investigating those modifications in future studies is expected to be beneficial for both research and practical purposes.

5. Conclusion

In this work, robust synthetic speech detection was achieved with DDAE network and i-vector inputs. The network consists of two MLPs, where the first MLP acts as a DAE. ASVspoof 2015 data were used in the experiments with human and spoof classes. Five different noise types at three different SNR levels were used at the test stage. The experimental results showed that the proposed DDAE system can deliver a better performance than multi-conditionally trained GMMs, with CQCC and filterbank features. Also, for clean test signals, the proposed network achieved sufficient performance (especially for the development set where the average EER was 0.22%). On the other hand, there was a performance gap between the state-of-the-art system and the proposed one. The possible reasons for the limited performance and opportunities for further improvements were discussed. Considering this work and previous literature, robust spoofed speech detection requires more complex systems, and masking noise dominant features are highly effective. Although the conventional speech enhancement methods were found to be ineffective, enhancing the noisy i-vectors with DDAE can offer alternative solutions.

Acknowledgement

This work was supported by TUBITAK under project number 121E057.

Author's Contributions

Gökay Dişken: Organized the datasets and the experiments, wrote the manuscript, analyzed the results.
Zekeriya Tüfekci: Supervised the experiments, assisted in designing the network structure, analyzed the results.

Ethics

There are no ethical issues after the publication of this manuscript.

References

- [1] Z. Wu, E. S. Chng, and H. Li, "Detecting converted speech and natural speech for anti-spoofing attack in speaker recognition," in *13th Annual Conference of the International Speech Communication Association 2012, INTERSPEECH 2012*, 2012, vol. 2, pp. 1698–1701.
- [2] A. Nautsch *et al.*, "ASVspoof 2019: Spoofing Countermeasures for the Detection of Synthesized, Converted and Replayed Speech," *IEEE Trans. Biometrics, Behav. Identity Sci.*, vol. 3, no. 2, pp. 252–265, Apr. 2021.
- [3] H. Delgado *et al.*, "ASVspoof 2017 Version 2.0: meta-data analysis and baseline enhancements," in *Odyssey 2018 The Speaker and Language Recognition Workshop*, 2018, pp. 296–303.
- [4] Z. Wu *et al.*, "ASVspoof: The Automatic Speaker Verification Spoofing and Countermeasures Challenge," *IEEE J. Sel. Top. Signal Process.*, vol. 11, no. 4, pp. 588–604, Jun. 2017.
- [5] M. Todisco, H. Delgado, and N. Evans, "Constant Q cepstral coefficients: A spoofing countermeasure for automatic speaker verification," *Comput. Speech Lang.*, vol. 45, pp. 516–535, Sep. 2017.
- [6] J. Yang and L. Liu, "Playback speech detection based on magnitude-phase spectrum," *Electron. Lett.*, vol. 54, no. 14, pp. 901–903, Jul. 2018.
- [7] A. T. Patil, H. A. Patil, and K. Khorja, "Effectiveness of energy separation-based instantaneous frequency estimation for cochlear cepstral features for synthetic and voice-converted spoofed speech detection," *Comput. Speech Lang.*, vol. 72, no. 1, p. 101301, Mar. 2022.
- [8] J. Yang, R. K. Das, and N. Zhou, "Extraction of Octave Spectra Information for Spoofing Attack Detection," *IEEE/ACM Trans. Audio, Speech, Lang. Process.*, vol. 27, no. 12, pp. 2373–2384, Dec. 2019.
- [9] C. Zhang, C. Yu, and J. H. L. Hansen, "An Investigation of Deep-Learning Frameworks for Speaker Verification Antispoofing," *IEEE J. Sel. Top. Signal Process.*, vol. 11, no. 4, pp. 684–694, Jun. 2017.
- [10] S. Scardapane, L. Stoffl, F. Rohrbain, and A. Uncini, "On the use of deep recurrent neural networks for detecting audio spoofing attacks," *Proc. Int. Jt. Conf. Neural Networks*, vol. 2017-May, pp. 3483–3490, 2017.
- [11] C. Haniçli, T. Kinnunen, M. Sahidullah, and A. Sizov, "Spoofing detection goes noisy: An analysis of synthetic speech detection in the presence of additive noise," *Speech Commun.*, vol. 85, pp. 83–97, Dec. 2016.
- [12] X. Tian, Z. Wu, X. Xiao, E. S. Chng, and H. Li, "An Investigation of Spoofing Speech Detection Under Additive Noise and Reverberant Conditions," in *INTERSPEECH 2016*, 2016, pp. 1715–1719.
- [13] A. Gómez Alanís, A. M. Peinado, J. A. Gonzalez, and A. Gomez, "A Deep Identity Representation for Noise Robust Spoofing Detection," in *Interspeech 2018*, 2018, pp. 676–680.
- [14] A. Gomez-Alanis, A. M. Peinado, J. A. Gonzalez, and A. M. Gomez, "A Gated Recurrent Convolutional Neural Network for Robust Spoofing Detection," *IEEE/ACM Trans. Audio, Speech, Lang. Process.*, vol. 27, no. 12, pp. 1985–1999, Dec. 2019.
- [15] S. Mahto, H. Yamamoto, and T. Koshinaka, "i-Vector Transformation Using a Novel Discriminative Denoising Autoencoder for Noise-Robust Speaker Recognition," in *Interspeech 2017*, 2017, pp. 3722–3726.
- [16] N. Dehak, P. J. Kenny, R. Dehak, P. Dumouchel, and P. Ouellet, "Front-End Factor Analysis for Speaker Verification," *IEEE Trans. Audio, Speech, Lang. Processing*, vol. 19, no. 4, pp. 788–798, May 2011.
- [17] W. Rao *et al.*, "Neural networks based channel compensation for i-vector speaker verification," in *2016 10th International Symposium on Chinese Spoken Language Processing (ISCSLP)*, 2016, pp. 1–5.
- [18] H. Yamamoto and T. Koshinaka, "Denoising autoencoder-based speaker feature restoration for utterances of short duration," in *Interspeech 2015*, 2015, pp. 1052–1056.
- [19] A. Varga and H. J. M. Steeneken, "Assessment for automatic speech recognition: II. NOISEX-92: A database and an experiment to study the effect of additive noise on speech recognition systems," *Speech Commun.*, vol. 12, no. 3, pp. 247–251, Jul. 1993.
- [20] D. Dean, A. Kanagasundaram, H. Ghaemmghami, M. H. Rahman, and S. Sridharan, "The QUT-NOISE-SRE protocol for the evaluation of noisy speaker recognition," in *Interspeech 2015*, 2015, pp. 3456–3460.

- [21] C. Zhang *et al.*, “Joint information from nonlinear and linear features for spoofing detection: An i-vector/DNN based approach,” in *2016 IEEE International Conference on Acoustics, Speech and Signal Processing (ICASSP)*, 2016, pp. 5035–5039.
- [22] A. Sizov, E. Khoury, T. Kinnunen, Z. Wu, and S. Marcel, “Joint Speaker Verification and Antispoofing in the i-Vector Space,” *IEEE Trans. Inf. Forensics Secur.*, vol. 10, no. 4, pp. 821–832, Apr. 2015.
- [23] D. Martinez, L. Burget, T. Stafylakis, Y. Lei, P. Kenny, and E. Lleida, “Unscented transform for ivector-based noisy speaker recognition,” in *2014 IEEE International Conference on Acoustics, Speech and Signal Processing (ICASSP)*, 2014, pp. 4042–4046.
- [24] D. Ribas and E. Vincent, “An Improved Uncertainty Propagation Method for Robust I-Vector Based Speaker Recognition,” in *2019 IEEE International Conference on Acoustics, Speech and Signal Processing (ICASSP)*, 2019, pp. 6331–6335.
- [25] W. Ben Kheder, D. Matrouf, M. Ajili, and J.-F. Bonastre, “A Unified Joint Model to Deal With Nuisance Variabilities in the i-Vector Space,” *IEEE/ACM Trans. Audio, Speech, Lang. Process.*, vol. 26, no. 3, pp. 633–645, Mar. 2018.
- [26] W. Ben Kheder, D. Matrouf, J.-F. Bonastre, M. Ajili, and P.-M. Bousquet, “Additive noise compensation in the i-vector space for speaker recognition,” in *2015 IEEE International Conference on Acoustics, Speech and Signal Processing (ICASSP)*, 2015, pp. 4190–4194.
- [27] W. Ben Kheder, D. Matrouf, P.-M. Bousquet, J.-F. Bonastre, and M. Ajili, “Fast i-vector denoising using MAP estimation and a noise distributions database for robust speaker recognition,” *Comput. Speech Lang.*, vol. 45, pp. 104–122, Sep. 2017.
- [28] G. Saon, H. Soltan, D. Nahamoo, and M. Picheny, “Speaker adaptation of neural network acoustic models using i-vectors,” in *2013 IEEE Workshop on Automatic Speech Recognition and Understanding*, 2013, pp. 55–59.
- [29] W. Wang, W. Song, C. Chen, Z. Zhang, and Y. Xin, “I-vector features and deep neural network modeling for language recognition,” *Procedia Comput. Sci.*, vol. 147, pp. 36–43, 2019.
- [30] Y. Qian, N. Chen, H. Dinkel, and Z. Wu, “Deep Feature Engineering for Noise Robust Spoofing Detection,” *IEEE/ACM Trans. Audio, Speech, Lang. Process.*, vol. 25, no. 10, pp. 1942–1955, Oct. 2017.
- [31] S. O. Sadjadi, M. Slaney, and L. Heck, “MSR Identity Toolbox v1.0: A MATLAB Toolbox for Speaker Recognition Research,” *IEEE Speech Lang. Process. Tech. Comm. Newsl.*, pp. 1–4, 2013.

Evaluation of the Relationship of Surface Roughness with Machining Parameters in Milling of AA 7075 Material with Experimental and Deform 3D Simulation

Ömer Erkan^{1*} 

¹ Düzce University, Faculty of Engineering, Department of Mechanical Engineering, Düzce, Türkiye

*omererkan@duzce.edu.tr

* Orcid No: 0000-0002-9428-4299

Received: 7 January 2023

Accepted: 11 May 2023

DOI: 10.18466/cbayarfbe.1231009

Abstract

AA 7075 T6 material offers important strength values and is easy to machining. In this respect, it is preferred on a wide scale in the industry. This study aimed to investigate the surface quality that occurs in the end milling of AA 7075 T6 material. For this, three different cutting speeds (40, 80, 120 m/min), three different feed rates (0.04, 0.08, 0.12 mm/rev), two different cutting depths (1 and 2 mm) were selected. The selected cutting parameters are combined with 2 and 4-flute end mills. As a result of the experiments, the average surface roughness (Ra) value was measured. The relations of Ra values with the cut parameters were determined. It was determined that Ra increased with increasing feed rate and decreased with increasing cutting speed. No significant effect of depth of cut was detected. Increasing the number of mouths increased Ra. The milling simulation was performed with the 3D cutting module in the Deform 3D software. 2 and 4 flute end mills are modeled, and the workpiece is defined to the software and the cutting parameters. Temperature, damage, stress, and cutting force outputs were estimated through simulations run at different cutting parameters. The predicted outputs and the experimental Ra outputs were interpreted. Experimental outputs were supported by successfully applying milling simulation in Deform 3D software.

Keywords: AA 7075 T6, milling, surface roughness, flute number, Deform 3D, simulation

1. Introduction

7xxx series aluminum alloys are primarily used in structural applications, aerospace, and aerospace industries due to their resistance to fatigue, high strength, ductility, toughness, and low density [1-2]. In order to increase the hardness, tensile and yield strength of aluminum, alloys made with elements such as Cu, Zn, and Mg are used in carrier profiles and constructions where strength is more prominent than other properties [3].

Milling is one of the most widely used processes among manufacturing processes. The surface form defects and the finishing surface determine the quality of the parts produced by the manufacturing operations. Surface quality plays a role in determining functional properties as well as product quality. Good surface quality effectively increases the tribological properties, wear resistance, fatigue strength, heat conduction, and aesthetic appearance of the materials. However, it can also cause an increase in production costs [4]. It has been

reported that the main critical parameters affecting the roughness of the surface in the milling process are cutting speed, feed rate, and depth of cut [5-9]. The effects of feed, cutting speed, and depth of cut on Ra in the end milling of the workpiece were examined in another study. [10].

On the other hand, CNC milling of 6061 Al alloy used genetic programming to estimate Ra in terms of vibrations and machining parameters [11]. Wang and Chang Al investigated the Ra parameter of 2014-T6 end milling [12]. In another study, which presented research on surface roughness estimation in milling, modeling data was collected by a central mixed experiment design. Variable parameters were determined as the depth of cut, cutting speed, and feed. In the modeling process, the authors used regression modeling and Artificial Neural Networks [13,14]. Zaghbani and Songmene developed a mathematical model to predict the cutting force and temperature depending on the material properties and cutting parameters in the milling of Al6061-T6 and Al7075-T6 alloys at high cutting speeds [15]. He

investigated the effects of cutting tool type and cutting parameters on burr formation and surface roughness in the milling process using a minimum coolant and conventional cooling technique. Three different cutting tools (HSS, TIN, and Carbide), speed (260, 780, and 1330 rpm), and feed rate (20, 40, and 80 mm/min) were used in the experiments. It was determined that the surface roughness increased with the feed rate, but the surface roughness decreased as the number of revolutions increased. In addition, it was reported that lower surface roughness values were achieved with carbide tools compared to TIN and HSS tools [16]. In another study, Al-5083 alloy was milled. The effects of milling parameters on the surface quality (Surface roughness and burr height) were investigated experimentally. Experiments were carried out using a carbide end mill with a diameter of 10 mm. Three different spindle speeds (3000-4000-5000 rpm), three different feed rates (0.05-0.075-0.1 mm/tooth), and two different cutting depths (1-1.5-2 mm) were selected as cutting parameters. However, the experimental design was determined according to the Taguchi L9 (33) orthogonal experimental setup. Experiments showed that cutting force and surface roughness decreased with increasing cutting speed, and burr height increased. It has been determined that while the cutting forces increase with the increase in feed rate, the surface roughness and burr height also increase. Using analysis of variance (ANOVA), it was found that the feed rate parameter among the control factors was the predominant factor on burr height, cutting force, and surface roughness. It was determined that this situation was followed by the cutting speed and the depth of the cut, respectively. Optimization studies have been proven to be successful with validation experiments [17]. In the study, the comparison of the surface roughness values obtained during the milling process on aluminum material and the simulated values through FEA is discussed. The cutting parameters used are three different cutting speeds, three different cutting depths, and constant feed. The material specified for the cutting tool is carbide (15% cobalt) with a tensile strength of approximately 400 N/mm². The cutting tool is a solid slab mill. Finite element analysis by using DEFORM 3D software, the milling process was carried out by changing the milling parameters on the workpiece, and roughness values were obtained during each procedure. The error between the experimental study and the simulation made by FEA was found to be in the range of $\pm 50\%$ [19]. The support heads of the fixture system were recommended in a study that suggested using a well-designed fixture with support heads to reduce deformation caused by milling square thin-walled aluminum plates made of high-carbon steel. The milling experiment was performed on a CNC Machining center using the same machining parameters as those used in DEFORM 3D-Simulation. Surface roughness was measured with and without fixtures during the milling process. As a result of using this fixture with a support head to reduce deformation, it was concluded that the surface roughness

values were reduced between a minimum of 3% and a maximum of 19% [20]. Another study investigated the effect of cutting parameters and machining conditions on tool wear. Machining experiments were carried out using two different lubricants, and the resulting tool wear was measured and compared. All experiments were carried out with high-speed steel (HSS) cutting tools. The turning process is simulated using DEFORM-3D. The results showed a significant reduction in tool wear when machining with multi-walled carbon nanotubes, with an average decrease of 14.8% compared to mineral oil. On the other hand, it was determined that reducing the depth of the cut was the most effective machining parameter in terms of minimizing tool wear [21].

In the study, milling experiments were carried out under different cutting tool geometries and cutting parameters using AA 7075 T6 material. In addition, a milling simulation was made with the help of Deform 3D software. As a result of the experimental study, the average surface roughness (Ra) parameter was measured. The results obtained from the simulation were used to interpret the surface quality and Ra.

2. Materials and Methods

The AA 7075 T6 material used in the milling experiments is 275x85x30 mm in size, and its chemical composition is shown in Table 1.

Table 1. Chemical composition of AA 7075 material.

Element	Fe	Si	Cu	Mn	Mg
Rate	0.5	0.5	1.2-2	0.3	2.1-2.9
Element	Zn	Cr	Zi+Ti	Other	Al
Rate	5.1-6.1	0.18-0.28	0.25	0.15	Rem.

AA 7075 material has been subjected to T6 heat treatment; its yield strength is between 460-505 MPa, its tensile strength is between 530-570 MPa, and its hardness value is between 140-160 Brinell. The cutting tools used for end milling have two different numbers of flutes (2 and 4). Uncoated end mills made of HSS material are 8 mm in diameter. In the study, the comparison of the surface roughness values obtained during the milling process on aluminum material and the

The experiments were carried out using DELTA SEIKI CNC vertical machining center with 11 kW engine power and 10000 rpm spindle speed. AA 7075 plates connected to the bench vise were machined with HSS end mills with 2 and 4 flutes. Figure 1 shows the milled AA 7075 plate.

All experiments were carried out under dry machining conditions. The cutting and tool geometry parameters used are shown in Table 2.

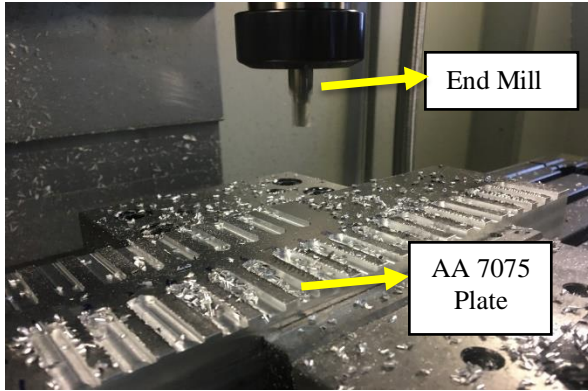


Figure 1. Milling of AA 7075 plate

The workpiece AA 7075 material was selected from the software's library. A triangular mesh is knitted on the selected material. The mesh number is 12000. The cutting tool was also selected from the software library. The number of cutting edges (2 and 4) of the chosen end mill is customized according to the experiment. The mesh of the end mill consists of 12000 triangles. The cutting parameters entered into the software are the parameters that give the largest and smallest average surface roughness values. In the last step before the simulation, the Usui tool wear model shown in Equation 1 is defined.

$$\frac{dw}{dt} = A \sigma_n V_s \exp(-B/T) \quad (1)$$

Table 2. Cutting parameters were used in the experiments

Cutting Tool Material	Flute Number (Z)	Cutting Depth (Ap), mm	Cutting Speed (Vc), m/min	Feed rate (f), mm/rev
HSS	2	1	40	0.04
			80	0.08
	4	2	120	0.12

A total of 36 experiments were carried out with 2 and 4 flute end mills. In addition, milling simulations were made using the cutting parameters that cause the smallest and largest surface roughness to occur with Deform 3D software. Simulation steps with Deform 3D are given in Figure 2.

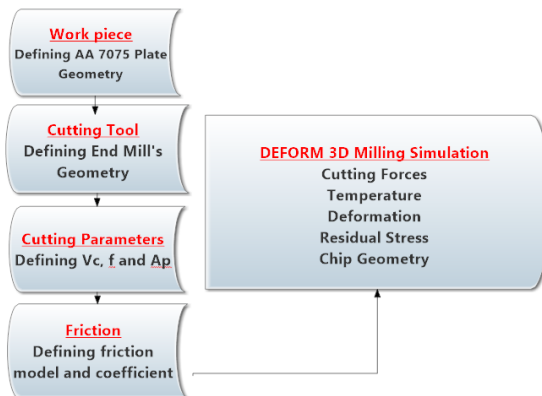


Figure 2. Deform 3D simulation steps.

In Equation 1, T is the shear temperature, σ_n is the normal stress, V_s is the shear rate, and B is the constant. Figure 3 gives a screenshot of the ready-to-run simulation with all definitions.

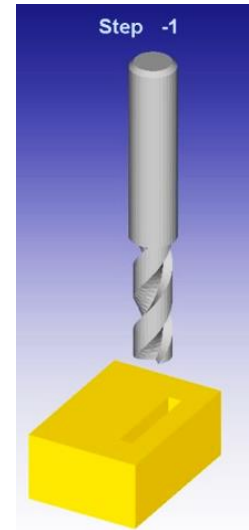


Figure 3. Ready-to-run milling simulation

Actual milling experiments are supported by the results obtained from the milling simulation run. Thus, the behavior of the Ra output made sense.

3. Results and Discussion

As a result of the experiments, the Ra value was measured by a profilometer. The relationship of Ra with the cutting parameters is visualized with the help of 3D graphics. Figure 4 shows the Ra values obtained from the experiments performed with the 2-flute end mill and their relations with the cutting parameters.

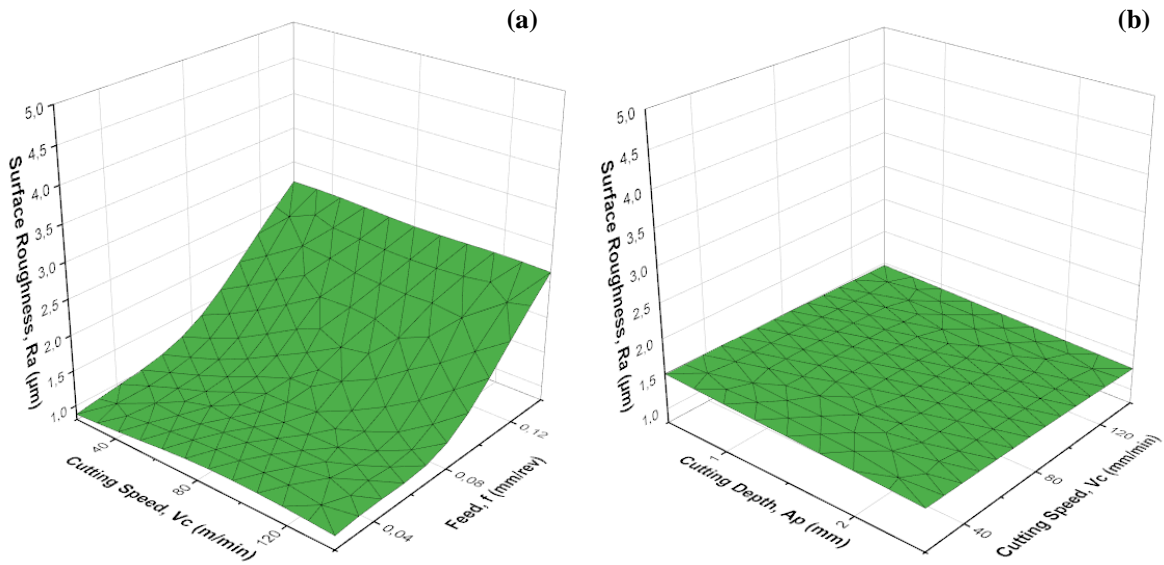


Figure 4. Experiment results with a 2-flute end mill. a) $A_p = 1\text{mm}$, Vc-f relationship b) A_p -Vc relationship

When Figure 4 is examined, it is observed that the surface roughness generally decreases with the increase of Vc in the 2-flute end mill, but this decrease is not very large. It has been determined that the increase of A_p also

decreases Ra, but this decrease is not significant. In Figure 5, the Ra values obtained from the experiments performed with the 4-flute end mill and their relations with the cutting parameters are shown.

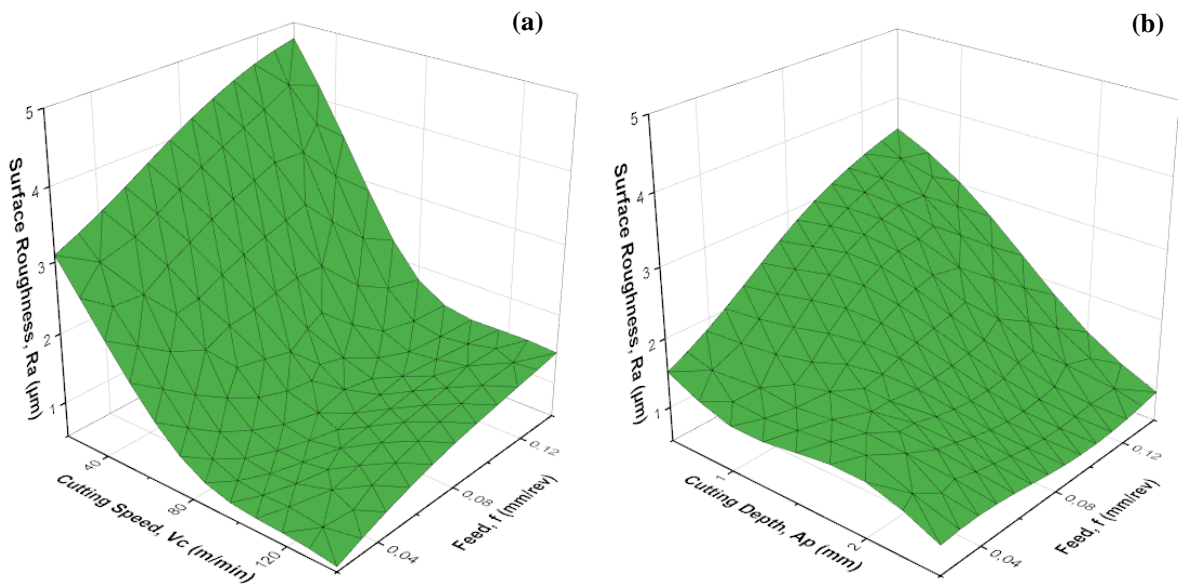


Figure 5. Experiment results with a 4-flute end mill. a) $A_p = 1\text{mm}$, Vc-f relationship b) A_p -Vc relationship

When Figure 5 is examined, the Ra value decreased significantly with the increased cutting speed in the experiments performed using 4-flute end mills. There is a significant increase with the increase in progress. An apparent effect of A_p on Ra was not observed. Figure 6

shows the comparison of 2- and 4-flute end mills. When Figure 6a is examined, it is observed that the 4-flute end mill produces larger Ra results than the 2-flute. Figure 6b shows that the 4-flute end mill produces higher Ra values at low cutting speeds than the 2-flute end mills, while it causes smaller Ra values at high cutting speeds.

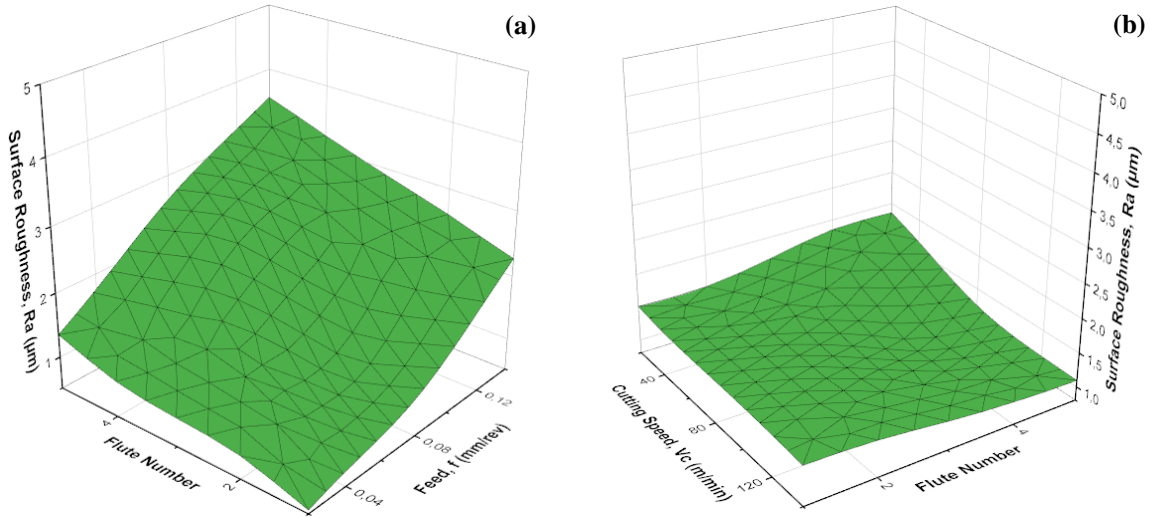


Figure 6. Comparison of test results with 2 and 4 flute end mills. a) $A_p=1\text{mm}$, b) $A_p=2\text{mm}$

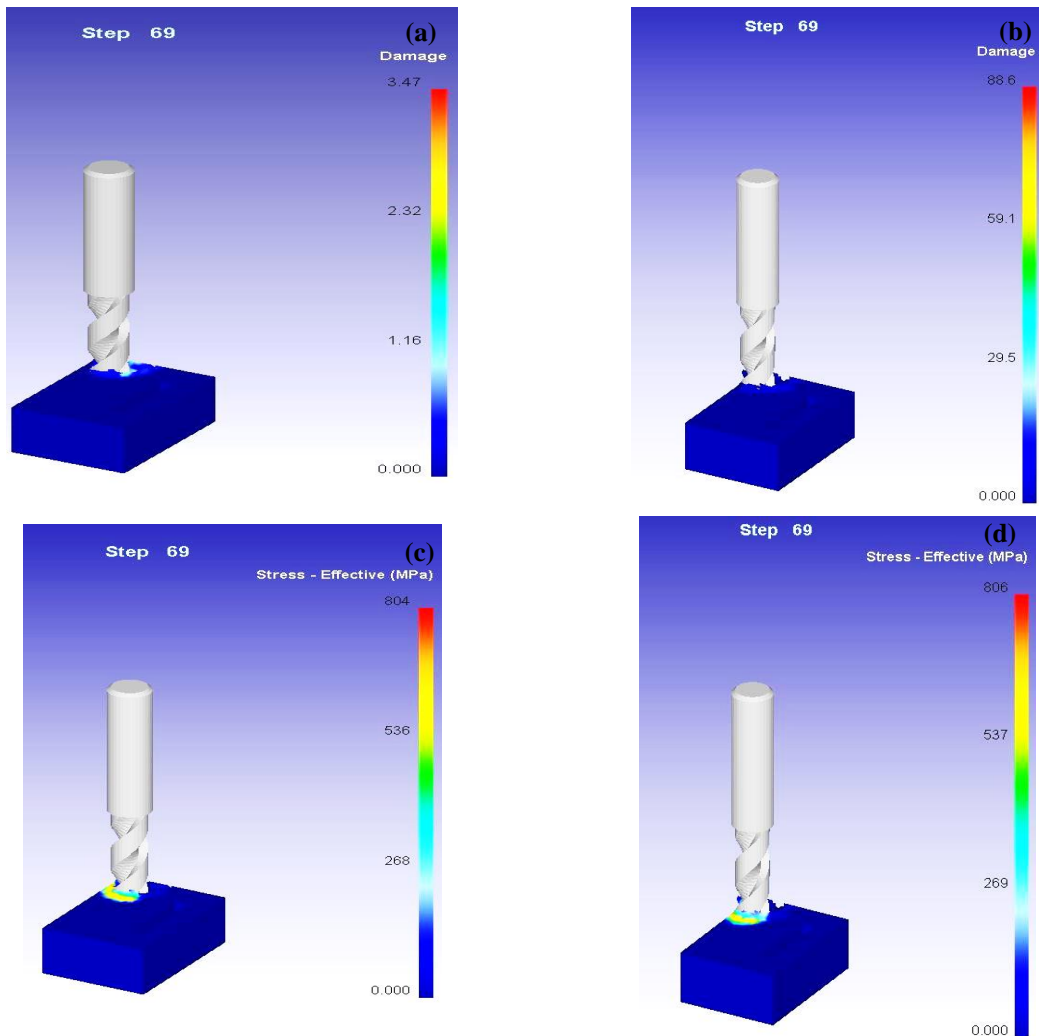


Figure 7. Damage-strain simulation results with a 2-flute end mill. a) $f=0.04\text{ mm/rev}$ damage result b) 0.12 mm/rev damage result, c) $f=0.04\text{ mm/rev}$ stress result, d) $f=0.12\text{ mm/rev}$ stress result

3.1. Deform 3D Results

Using the 3D cutting module of Deform 3D software, milling simulations of 2-flute and 4-flute end mills were created at different cutting parameters. The results of these simulations, such as damage, temperature, and force, are discussed. Figure 7 shows the damage and stress results of the simulation performed with a 2-flute end mill at a cutting speed of 40 m/min using 0.04 mm/rev and 0.12 mm/rev feed rate.

When Figures 7 c and d are examined, it has been determined that similar stress values occur in both feed rate values.

While the cutting tool contacted the workpiece more slowly at 0.04 mm/rev feed rate, the damage occurred at a maximum rate of 3.47, while at a 0.12 mm/rev feed rate, it occurred at a maximum of 88.6 as a result of a faster contact. This is illustrated in Figures 7 a and b. Feed rate is the cutting parameter that has the greatest influence on surface roughness [18]. Considering this situation, the temperature and force changes occurring at different progressions are presented in the simulation. Figure 8 shows the simulation's temperature and force results performed with a 2-flute end mill at different feed rates.

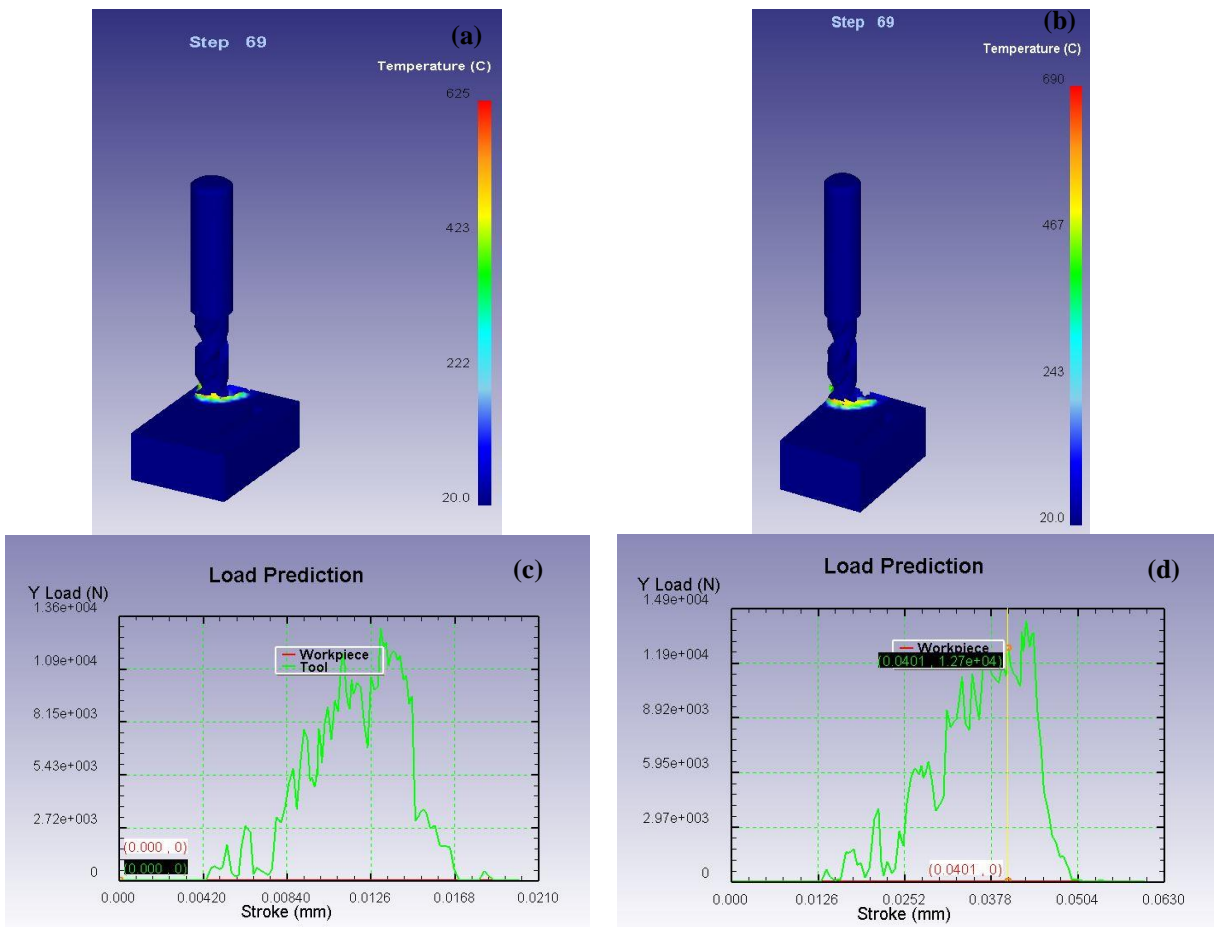


Figure 8. Temperature-force simulation results with a 2-flute end mill. a) $f=0.04$ mm/rev temperature result b) 0.12 mm/rev temperature result, c) $f=0.04$ mm/rev force on the Y axis, d) $f=0.12$ mm/rev result on the Y axis.

Figure 8 shows that the maximum temperature is 625 °C at 0.04 mm/rev feed rate, and it can go up to 690 °C at 0.12 mm/rev feed rate in Figure 8 b. At higher temperatures, due to the ductile nature of AA 7075 material, adhesion to the cutting tool occurs in greater amounts. This is a crucial case that increases it to the Ra parameter. Increasing feed rate increases cutting

forces. In Figures 8 c and d, the greatest force in the Y-axis was estimated as 74 N at 0.04 mm/rev feed rate, while this value was estimated to be approximately 81 N at 0.12 mm/rev feed rate. Similar results were obtained in temperature, stress, damage, and force outputs with the change of feed rate in simulations made with a 4-flute end mill. In Figure 9, damage rates of 2 and 4 flute end mills are given.

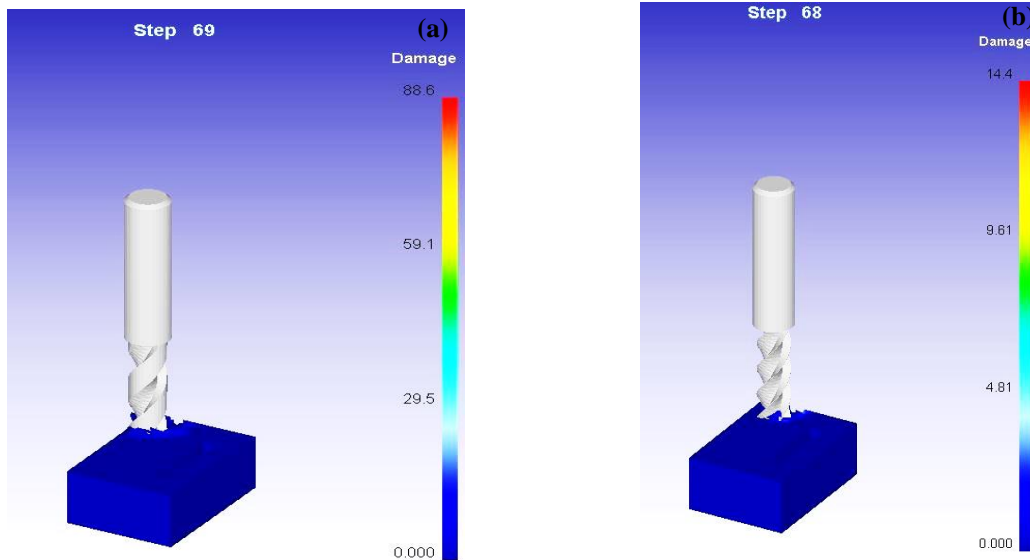


Figure 9. Damage results of 2 and 4 flute end mills at 0.12 mm/rev feed rate. a) 2 flutes b) 4 flutes.

Figure 9 shows that the 2-flute end mill causes greater damage to the AA 7075 material. However, this situation was reflected in contrast to the Ra parameter in actual experiments. The reason for this can be explained as the chips sticking to the cutting tool due to the ductile nature of the AA 7075 material. Since the amount of sticking chips is less in a 2-flute end mill, it causes minor damage to the machined surface, and Ra is lower.

4. Conclusion

AA 7075 material was machined under different cutting parameters with 2 and 4-flute end mills. Ra parameters of the machined surfaces were measured. In addition, milling simulation was made with Deform 3D software for different values of the feed rate parameter, which has the most significant effect on the Ra parameter. The simulation results and predictions supported experimental results. The obtained results can be listed as follows:

- Ra parameter decreased with the increase of cutting speed. Lower Ra values were measured at a 120 m/min cutting speed.
- The Ra parameter increased proportionally with the increase in the feed rate. In experiments with a feed rate of 0.12 mm/rev, Ra is measured larger.
- No significant effect of the depth of cut on Ra was revealed.
- While increasing the number of flutes increased the Ra parameter, it decreased the burrs on the surface.
- As a result of the milling simulation with Deform 3D, it is estimated that the increase in the feed rate will increase the temperature, damage, and cutting force.
- It has been determined that increasing temperature and cutting force have a negative effect on the Ra parameter.
- Milling simulation with Deform 3D has been successfully performed for 2 and 4 flute end mills.

Author's Contributions

The author carried out the experiments and simulations. Wrote and edited the article.

Ethics

There are no ethical issues after the publication of this manuscript.

References

- [1] Rendigs, K.H. 1997. "Aluminum structures used in aerospace Status and prospects"[J]. *Mater Sci Forum*.
- [2] Williams, J.C., Jr Starke E.A., 2003. "Progress in structural materials for aerospace systems [J]", *Acta Mater*.
- [3] Demirci, H., 2004. *Malzeme Bilgisi ve Malzeme Muayenesi Seçilmiş Temel Kavramlar ve Endüstriyel Uygulamalar*, Alfa Basım Yayın.
- [4] Kakati, A. K., Chandrasekaran, M., Mandal, A., Singh A.K. 2011. "Prediction of optimum cutting parameters to obtain desired surface in finish pass end milling of aluminium alloy with carbide tool using artificial neural network", *World Academy Of Science And Engineering and Technology*, Volume 5, Number 9, p.1929-1935.
- [5] Salguero Gómez, J. Analysis, 2013. *Evaluation and Proposals for Performance Enhancing in Highspeed Machining of Aeronautical Aluminum Alloys*. Ph.D. Thesis, University of Cadiz, Cadiz, Spain.
- [6] Baek, D.K.; Ko, T.J.; Kim, H.S. 2001. Optimization of feed rate in a face milling operation using a surface roughness model. *Int. J. Mach. Tools Manuf.*, 41, 451–462
- [7] Salguero, J.; Batista, M.; Calamaz, M.; Giro, F.; Marcos, M. 2013. Cutting forces parametric model for the dry highspeed contour milling of aerospace aluminum alloys. *Procedia Eng.*, 63, 735–742.
- [8] Cai, X.J.; Ming, W.W.; Chen, M. 2012. Surface integrity analysis on high speed end milling of 7075 aluminium alloy. *Adv. Mater. Res.*, 426, 321–324.
- [9] Ammula, S.C.; Guo, Y.B. 2005. Surface integrity of Al 7050-T7451 and Al 6061-T651 induced by high speed milling. *J. Aerosp.*

- [10] Yang, J. L.; Chen, J. C. 2001. A systematic approach for identifying optimum surface roughness performance in end-milling. // *J Ind Technol.* 17, 2, pp. 1-8.
- [11] Brezocnik, M.; Kovacic, M; Ficko, M. 2004. Prediction of surface roughness with genetic programming. // *J Mater Process Technol.* 157-158, pp. 28-36.
- [12] Wang, M. Y.; Chang, H. Y. 2004. Experimental study of surface roughness in slot end milling Al2014-T6. // *Int J Mach Tools Manuf.* 44, (2004), pp. 51-57.
- [13] Simunovic, G.; Simunovic, K.; Saric, T. 2013. Modelling and Simulation of Surface Roughness in Face Milling. // *International Journal of Simulation Modelling.* 12, 3, pp. 141-153.
- [14] Saric, T.; Simunovic, G.; Simunovic K. 2013. Use of Neural Networks in Prediction and Simulation of Steel Surface Roughness. // *International Journal of Simulation Modelling.* 12, 4, pp. 225-236.
- [15] Zaghbani, I., Songmene V. 2009. "A force-temperature model including a constitutive law for dry high speed milling of aluminium alloys", *Journal of Materials Processing Technology*, Volume 209, Number 5,
- [16] Hüseyinoğlu, M., 2008. 7075 Alüminyum Alaşımın Freze ile İşlenmesinde Minimum Soğutma Sıvısı Kullanmanın Performans Karakteristiklerine Etkisi. Fırat Ü. Fen Bilimleri Enstitüsü, Yüksek Lisans Tezi, 48s, Elazığ
- [17] Bayraktar, Ş., Turgut, Y, 2016. "Al-5083 Alaşımının Frezelenmesinde Kesme Kuvveti, Yüzey Pürüzlülüğü Ve Çapak Yüksekliğinin Optimizasyonu" 7th International Symposium On Machining, November 3-5, Marmara University, Istanbul
- [18] Erkan Ö., Yücel E. 2018 "Parmak frezelenen AA 7075 malzemenin yüzey pürüzlülüğünün kesme parametreleri ve takım geometrisi ile olan ilişkisinin optimizasyonu" International Eurasian Conference on Science, Engineering and Technology (EurasianSciEnTech 2018), November 22-23, 2018 Ankara, Turkey
- [19] Vishwakarma P., Sharma A., 2020 "3D Finite Element Analysis of milling process for non-ferrous metal using deform-3D", *Materials Today: Proceedings*, Volume 26, Part 2, Pages 525-528,
- [20] Natarajan, M.M., Chinnasamy, B., Alphonse, B.H.B., 2022 "Deform 3D Simulation and Experimental Investigation of Fixtures with Support Heads" *MECHANIKA* Volume 28(2): 130-138
- [21] Okokpujie, I.P.; Chima, P.C.; Tartibu, L.K. 2022, "Experimental and 3D-Deform Finite Element Analysis on ToolWear during Turning of Al-Si-Mg Alloy" *Lubricants*, 10, 341.

Investigation of Different Oriented 2D Straight Breakwater Under Dynamic Conditions

Mustafa Murat Yavuz¹ , Pınar Sarı Çavdar^{2*} 

¹ İzmir Democracy University, Department of Mechanical Engineering, 35140 İzmir, Türkiye

² İzmir Democracy University, Department of Civil Engineering, 35140 İzmir, Türkiye

*pinar.cavdar@idu.edu.tr

*Orcid No: 0000-0002-1989-4759

Received: 5 January 2023

Accepted: 8 June 2023

DOI: 10.18466/cbayarfbe.1229763

Abstract

There are limited studies in the literature on breakwaters, and studies of the flow structure between the breakwater and the shore are limited. In this study, flow behavior behind a breakwater was investigated for plane-based model. In the examination, straight models at different position angles were used for the breakwater. Dynamic inlet flow was utilized, and the commonly used two-row amplitude wave model was applied. The focus is on the area between the breakwater and the coastline, which is important for the use of breakwaters. $\theta=-8^{\circ}$ results mostly have the lowest total pressure values. The usage of $\theta=+8^{\circ}$ position in placement of straight breakwater gives the most suitable response because of the least dynamic pressure. The results were discussed in detail.

Keywords: Amplitude, breakwater, pressure, wave.

1. Introduction

With the importance given to maritime trade and maritime transport, marinas have gained a lot of popularity. Many studies have been put forward for the development of maritime transport and the design of new ports. Breakwater designs are one of the basic marina structures, and some studies [1-8] have been conducted on their resistance to the pressures which are exposed to them. Dynamic wave motions are complex and some case studies were investigated to understand their physics [9-10]. Different wave models [11] have directly interacted with the breakwater. However, ocean waves move in many directions and are variable. The structure [12] is continuously subjected to forces and moments. The absence or minimal occurrence of damage during the design phase affects the cost analysis of the structure's operation.

The accuracy of the project and the correct construction affect the life of the structure. Hence, structures were inspected and categorized based on whether they were in static or dynamic situations. A case study including wave flumes

[13] were analyzed under irregular waves on a vertical wall. The experimental study have a scale factor of 1:30 compared to a real model and the gained data could be used future designs. Case studies have been done on the effects of slope, and effects of overlapping layer thickness (OLT) and overlapping flow rate (OFV) were [14] investigated. The high variability of waves has necessitated more studies. While the performance of breakwaters [15] has increased with new designs, their structural condition has become more complex.

In the literature, there were few studies on flow behavior for flat breakwaters located in front of the shore. In this study, the flow formed behind a flat breakwater positioned in front of the shore was investigated numerically.

2. Modelling

A numerical model has been created to examine breakwaters operating in time dependent conditions. In Fig. 1, a flat breakwater was modelled in a control area and boundary conditions were shown. The figure also includes different breakwater models.

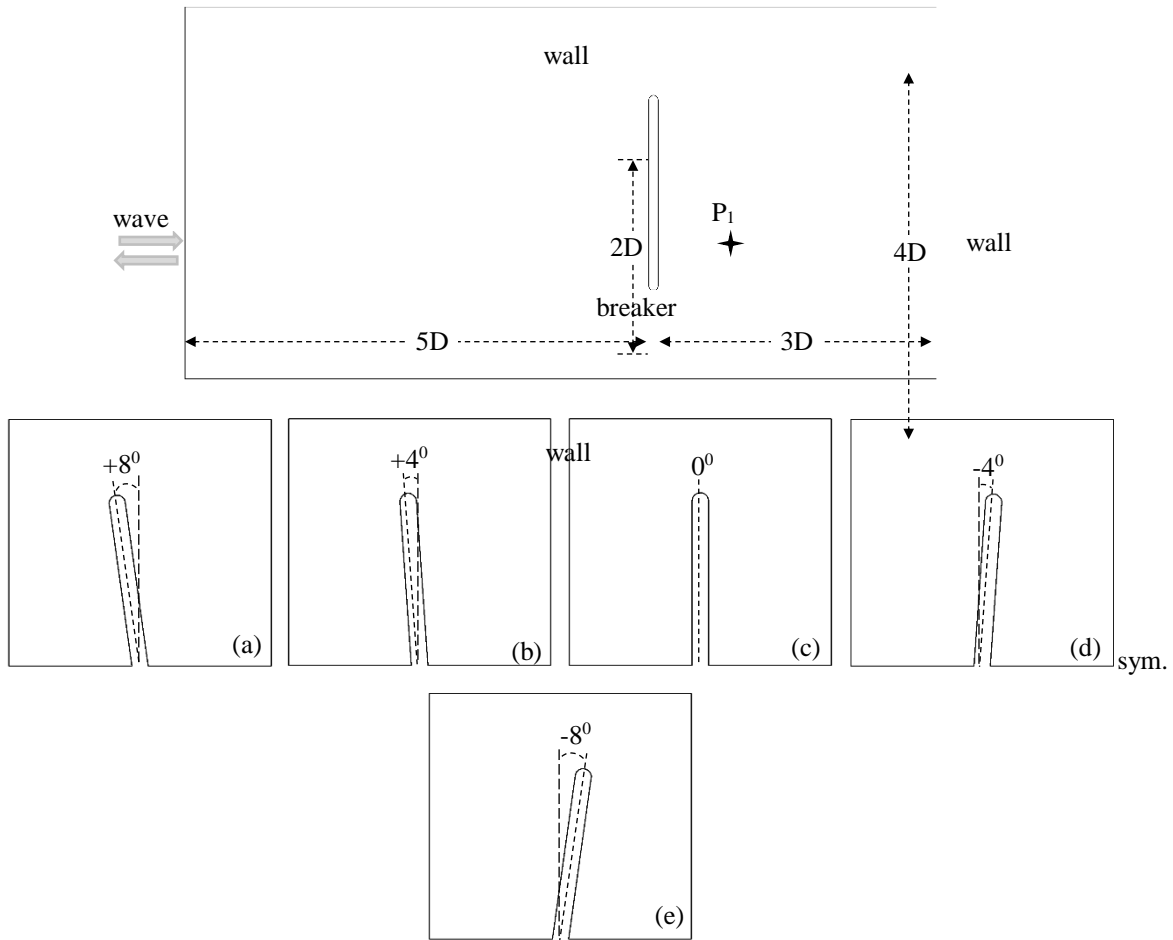


Figure 1. Analysis domain and straight wave breaker models.

As the boundary conditions, the place where the waves entered the control volume was defined as the velocity input. The same place was defined as the outlet to describe the retraction of waves. Breakwater and other edges were defined as wall. Breakwater length ($2D$) was 120 m and all other dimensions were defined according to this length. To measure the wave effects over time behind the breakwater, the P_1 point was defined at a distance of D away from the breaker. The results were obtained at certain time intervals from there. The straight breakwater model was positioned at 5 different angles. k -epsilon, k -omega and RNG (Re-normalization group) turbulence models [16] were generally used in investigations. In the examinations, the standard k -epsilon model was used in turbulence models in order to observe the eddies behind the breakwater structure. The k -epsilon turbulence model is one of the most suitable models among various models in terms of solution sensitivity and resolution time. ANSYS CFD software with default properties was used for simulations.

In Fig. 2, the wave entry velocity to the control volume was given according to time. Water was used as fluid. (density = 998.2 kg/m^3 and dynamic viscosity 0.001003 kg/ms). The analysis was done at 0.002 second intervals for a total of 9 sec.

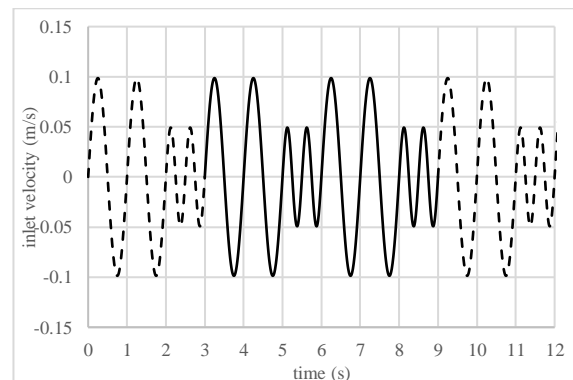


Figure 2. Inlet velocity frequency.

3. Results and Discussion

In Fig. 3, first, the difference between the number of grid elements and the results has been examined in order to see the accuracy and consistency of the numerical solution results. In order to see the results, an analysis was made and instantaneous static pressure on the frontal surface of breaker was considered. Half of the breakwater results was given with respect to symmetry condition. The path length is equal to length of frontal breakwater surface, $D=60$ m. When the results were evaluated, it was suitable for a solution with approximately 56000 elements.

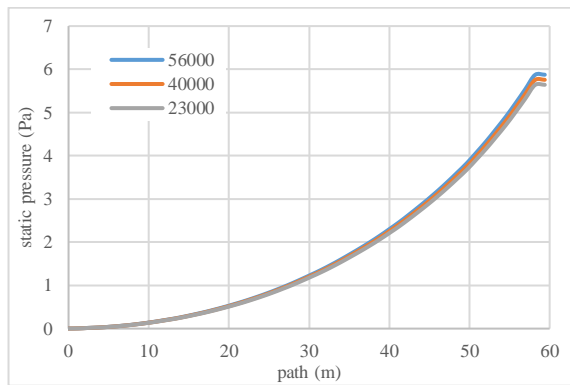


Figure 3. Static pressure on frontal surface of breakwater with respect to number of grid elements.

In order to see the sensitivity in the analysis, 3 different turbulence models were compared in Fig. 4. The k-epsilon turbulence model was used in the rest of the study due to its smaller eddy structure and more pronounced interaction with the breakwater compared to the other two turbulence models.

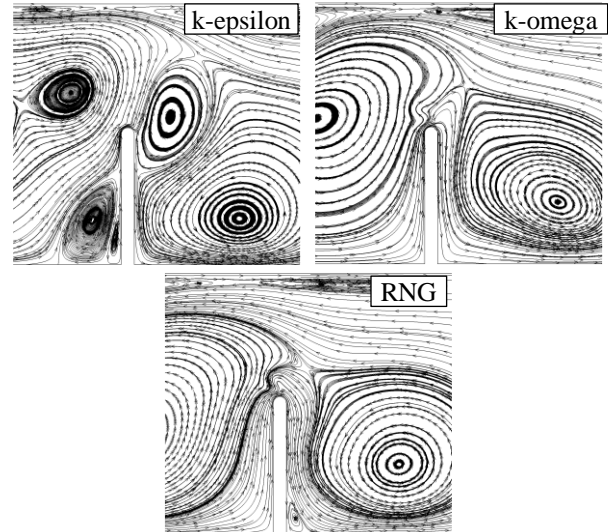
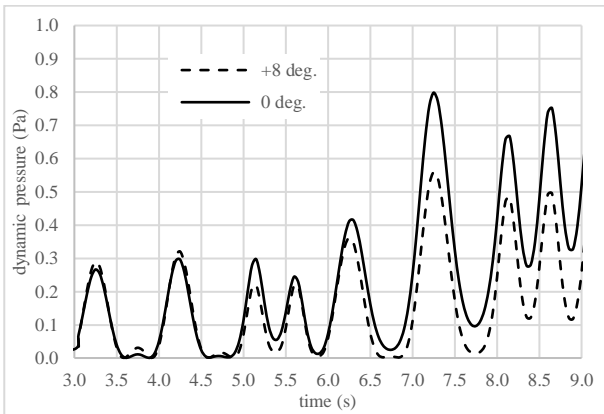


Figure 4. Instantaneous streamline results of different turbulence models at 9 sec.

Dynamic, static and total pressure results were shown at point P_1 over time in Table 1. In the results, the model with the times of low pressure as much as possible was preferred. In the results, mostly the lowest dynamic pressure values were found at $\theta=+8^\circ$. However, the lowest values of the total pressure in general were found at $\theta=-8^\circ$. Considering that the dynamic pressure effect will be more dominant, the $\theta=+8^\circ$ result was accepted as the most ideal according to the other results. $\theta=+8^\circ$ model was compared with $\theta=0^\circ$ straight model.

Table 1. Time dependent pressure values at point P_1 (units in Pa).

time (s)	$\theta=+8^\circ$			$\theta=+4^\circ$			$\theta=0^\circ$			$\theta=-4^\circ$			$\theta=-8^\circ$		
	Dyna.	Static	Total	Dyna.	Static	Total	Dyna.	Static	Total	Dyna.	Static	Total	Dyna.	Static	Total
3	0.027	-42.94	-42.91	0.032	-42.23	-42.19	0.036	-41.67	-41.64	0.025	-43.09	-43.06	0.019	-43.59	-43.57
3.5	0.032	42.03	42.06	0.037	42.87	42.91	0.040	42.05	42.09	0.048	42.52	42.56	0.049	41.97	42.02
4	0.036	-43.57	-43.53	0.055	-43.21	-43.16	0.050	-42.75	-42.70	0.063	-42.70	-42.64	0.070	-42.09	-42.02
4.5	0.028	42.03	42.06	0.062	41.39	41.46	0.024	41.00	41.03	0.030	40.50	40.53	0.030	39.93	39.96
5	0.069	-45.16	-45.09	0.151	-44.66	-44.51	0.112	-44.61	-44.49	0.211	-42.76	-42.55	0.266	-42.73	-42.47
5.5	0.089	-43.38	-43.29	0.080	-45.09	-45.01	0.136	-41.74	-41.61	0.180	-43.22	-43.04	0.261	-42.56	-42.30
6	0.058	-43.32	-43.26	0.093	-43.97	-43.88	0.072	-42.25	-42.18	0.302	-42.47	-42.17	0.723	-41.24	-40.52
6.5	0.075	42.76	42.84	0.345	42.61	42.96	0.164	42.70	42.86	0.712	41.93	42.64	0.827	43.17	44.00
7	0.110	-43.63	-43.52	0.448	-43.75	-43.31	0.250	-43.47	-43.22	0.576	-42.97	-42.39	0.633	-41.66	-41.02
7.5	0.175	42.94	43.11	0.385	42.55	42.93	0.326	42.39	42.71	0.363	42.01	42.37	1.111	41.19	42.30
8	0.242	-43.83	-43.58	0.397	-43.89	-43.49	0.414	-43.55	-43.14	0.438	-43.02	-42.58	1.562	-42.67	-41.10
8.5	0.271	-43.42	-43.14	0.314	-43.43	-43.11	0.476	-42.84	-42.37	0.372	-42.78	-42.41	1.245	-42.37	-41.13
9	0.256	21.01	21.27	0.249	20.96	21.21	0.512	20.71	21.22	0.323	20.44	20.76	0.883	19.90	20.78



In Fig. 4, dynamic pressure values are taken from the P_1 measurement point located behind the breakwater. The average of the solutions stabilized after 2.5 sec. In the vertically used $\theta=0^\circ$ model, the average dynamic pressure is higher and instantaneous results tend to decrease-increase more sharply.

Especially after the 2nd large wave amplitude, this situation seems clearer. The $\theta=+8^\circ$ model yielded the most favorable results, with less sensitivity to wave amplitudes.

Figure 4. Dynamic pressure results at P_1 .

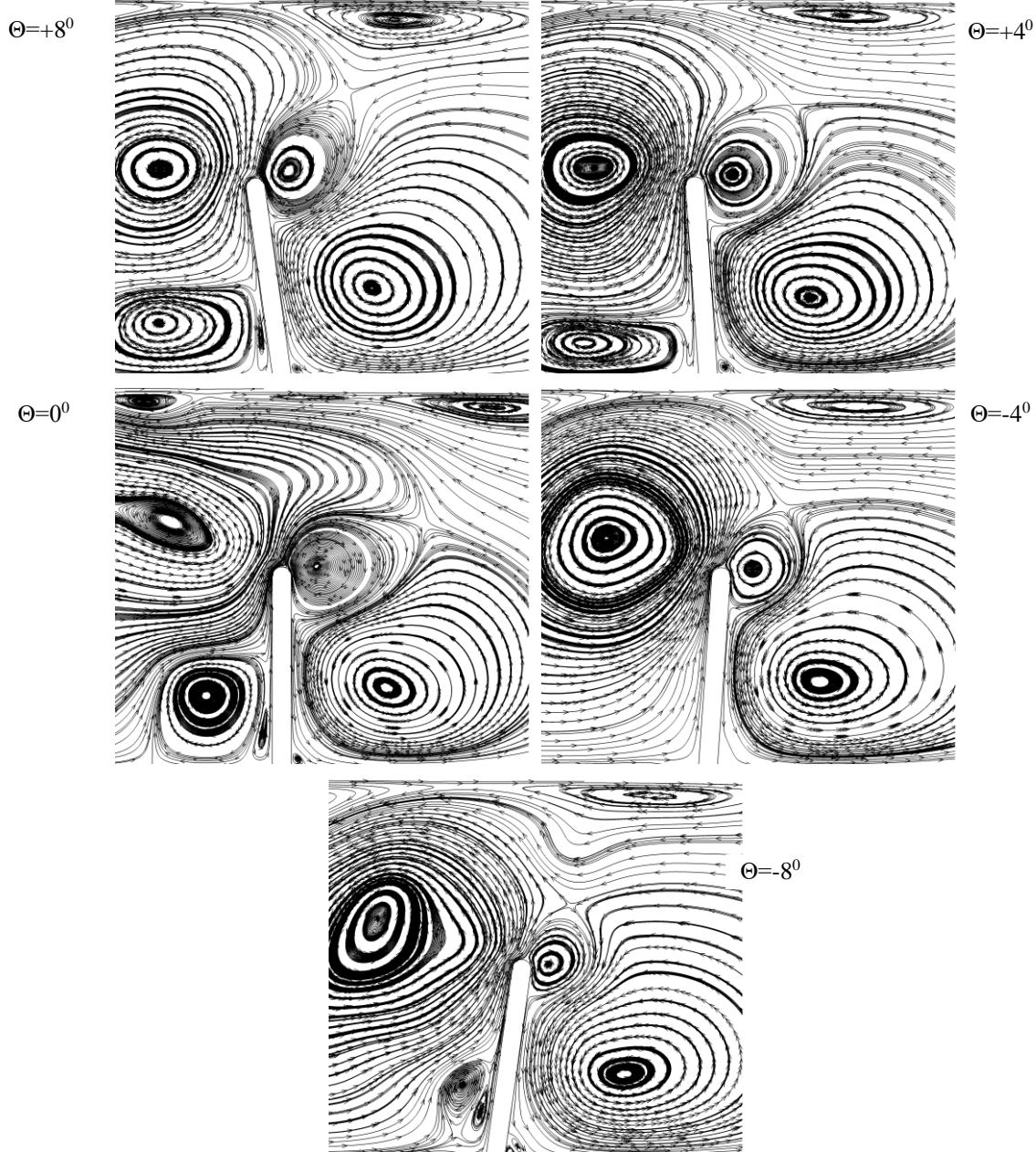


Figure 5. Streamlines of mean velocity at 9 sec.

Average velocity streamlines were shown in Fig. 5. The interaction of the waves with the breakwater and the shore appeared clearly in all results. In the model with $\theta=0^\circ$, a vortex was formed behind the breakwater. Vortex centered $0.5 D$ from the bottom edge and $0.7 D$ from the breakwater. The model results with $\theta=-4^\circ$ were similar. By observing the size of the vortex formed behind the breakwater, the effective distance of breakwater was approximately determined. Only the effective range has increased to $1.6 D$ horizontal length. Similar vortex profile occurred in $\theta=+4^\circ$ and $\theta=+8^\circ$ models, but the effective distance was lower than $1.5 D$. As a result of $\theta=-8^\circ$, the vortex eye has moved predominantly in the vertical direction. The circulation that occurred under the place where the vortex was formed created a flow separation zone.

The effective range of the breakwater has increased to about $2 D$. However, the flow irregularity increased.

The horizontal component of mean velocity profiles was given in Fig. 6. Velocity profiles were shown as the highest H^{++} in the positive direction and the highest L^{-} in the negative direction. The model in which these profiles formed the least behind the breakwater has occurred as a result of $\theta=+8^\circ$. On the tip of the breakwater, there was a separation zone where a high velocity profile formed. The highest velocity profile in the negative direction mostly formed in the vertical direction from the breakwater tip region. In the results of $\theta=-8^\circ$, the highest positive velocity region appeared to be the most unsuitable profile since it occurs behind the breakwater.

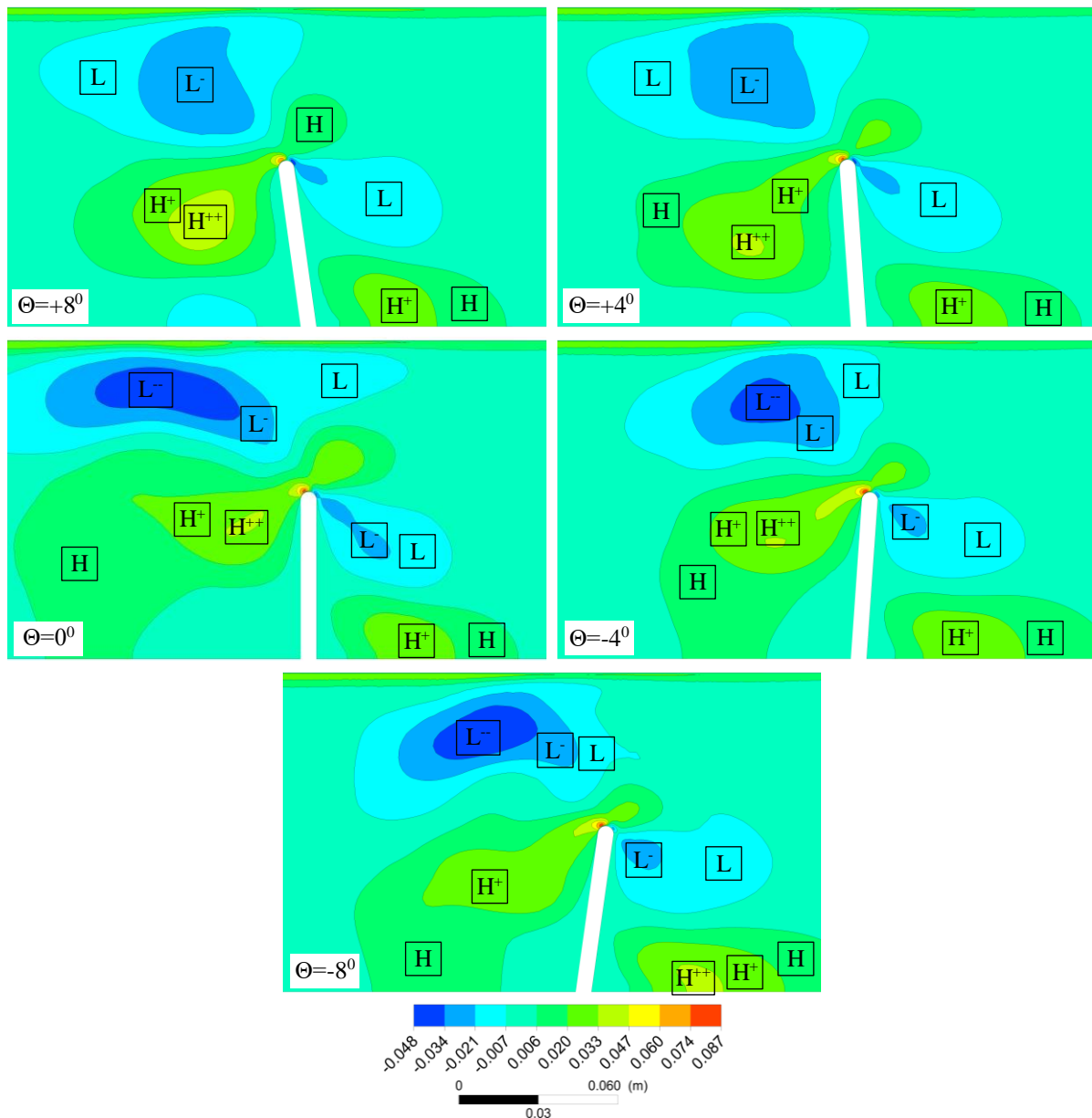


Figure 6. Mean velocity contours at 9 sec. (contour values are in m/s).

4. Conclusion

In this study, straight breakwater models with different position angles were examined numerically. Effect of position angles is given and compared. Time dependent analysis was used, and average results were considered. The results can be summarized;

- The position angle was effective on straight breakwater models and the usage of $\theta=+8^0$ has positive effects
- Most of the least total pressures occurred at $\theta=-8^0$
- The highest velocity profiles formed at the least behind the breakwater has occurred in the result of $\theta=+8^0$

Acknowledgement

This research did not receive any specific grant from funding agencies in the public, commercial, or not-for-profit sectors.

Author's Contributions

M. Murat Yavuz: Obtained and interpreted visuals and tables by doing numerical work.

Pınar Sarı Çavdar: Created the emphasis of the study by writing the literature review and introduction section

Ethics

There are no ethical issues after the publication of this manuscript.

References

- [1]. Miche, R. 1944. Mouvements ondulatoires de la mer in profondeur constante ou décroissante. *Annals des Ponts et Chaussées*; Paris, Vol. 114.
- [2]. Minikin, RR. 1950. Winds, waves and maritime Structures. *Charles Griffin*, London.
- [3]. Ito, Y, Tanimoto, K. 1971. Meandering damages of composite type breakwaters. *Tch.Note of Port and Harbour Res*; Inst., No 112. 20p. (in Japanese)
- [4]. Nagai, S. 1973. Wave forces on structures. *Advances in Hydroscience, Academic Press, New York*; 9: 253–324.
- [5]. Goda, Y. 1974. New wave pressure formulae for composite breakwaters. *Proc. 14th Int.Conf. on Coastal Engineering*; ASCE, 1702–1720.
- [6]. Goda, Y. 1985. Random seas and design of maritime structures. University of Tokyo.
- [7]. Ahrens, JP, Mc Cartney, BL. 1975. Wave period effect on the stability of riprap. *Proc. Civil Engineering in the Ocean III*; 2: 1019-1034.
- [8]. Takahashi, S, Tanimoto, K. 1994. Design and construction of caisson breakwaters – the Japanese experience. *Coastal Engineering*; 22(1–2): 57–77.
- [9]. Van der Meer, JW. 1988. Rock slopes and gravel beaches under wave attack. *Delft University of Technology, Doctoral Thesis*; No. 396, Delft.

[10]. Naimi, S, Özdemir, Z. 2020. Yapılarda yer altı suyunu karşı yapılan koruma sistemlerinin uygulanabilirliği ve güvenliğinin incelenmesi. *AURUM Journal of Engineering Systems and Architecture*; 4(1): 113-133.

[11]. Zhao, XL, Ning, DZ, Zou, QP, Qiao, DS, Cai, SQ. 2019. Hybrid floating breakwater-WEC system: a review. *Ocean Engineering*; 186: 106126.

[12]. Loukogeorgaki, E, Yagci, O, Kabdasli, MS. 2014. 3D Experimental investigation of the structural response and the effectiveness of a moored floating breakwater with flexibly connected modules. *Coastal Engineering*; 91: 164–180





[13]. Huang, J, Chen, G. 2022. Experimental study of wave impact on a vertical wall with overhanging horizontal cantilever slab and structural response analysis. *Ocean Engineering*; 247: 110765.

[14]. Mares-Nasarre, P, Argente, G, Gómez-Martín, ME, Medina, JR. 2019. Overtopping layer thickness and overtopping flow velocity on mound breakwaters. *Coastal Engineering*; 154: 103561.

[15]. Mustapa, MA, Yaakob, OB, Ahmed, YM, Rheem, C, Kohb, KK, Adnana, FA. 2017. Wave energy device and breakwater integration: A review. *Renewable and Sustainable Energy Reviews*; 77: 43–58.

[16]. Dentale, F, Reale, F, Leo, AD, Carratelli, EP. 2018. A CFD approach to rubble mound breakwater design. *International Journal of Naval Architecture and Ocean Engineering*; 10: 644-650.

Influence of Nanofibrillated Cellulose on Mechanical and Thermal Properties of Polyester Composites

Bayram Poyraz^{1*} , Şevki Eren² , Serkan Subaşı³ , Ayhan Tozluoğlu³ 

¹ Department of Civil Engineering, Faculty of Engineering, Düzce University, Düzce, Türkiye

² Vocational School, Kırşehir Ahi Evran University, Kırşehir, Türkiye

³ Department of Civil Engineering, Faculty of Engineering, Düzce University, Düzce, Türkiye

⁴ Forest Product Engineering, Faculty of Forestry, Düzce University, Düzce, Türkiye

*bayrampoyraz@duzce.edu.tr

* Orcid No: 0000-0003-1209-8095

Received: 17 March 2022

Accepted: 2 May 2023

DOI: 10.18466/cbayarfbe.1089023

Abstract

This study reports the effects of bio-based CNF (nano fibrillated cellulose) fillers on the properties of PE (Polyester) composites. In the study, the PE was mixed with CNF) in the ratios of 0.5, 1, and 1.5 % using Methyl Ethyl Ketone Peroxide (MEKP) and Cobalt octoate (CoOc) as initiator and catalyst, respectively. For characterization, chemical and thermal analyses were carried out with FT-IR and TGA. Mechanical properties were investigated with Universal Testing Machine, and morphological properties were investigated with SEM. In consequence, minor altered vibrations were observed in FT-IR while thermal stability decreased. The compressive strength of composites was lower than that of the neat PE composite whereas tensile strength increased. Mostly homogenous dispersion was also seen in the composites. This study reveals that CNF fillers are able to applicate in PE resin which used in the pipeline sector.

Keywords: Polyester, CNF, mechanical properties, thermal properties

1. Introduction

Recently, industries have begun to allow new projects related to the green material based composites which reveals high strength at a small specific weight as well as can be tailored for certain aims [1].

Fillers (silica, basalt, aramid, carbon fibers) are important in the composite production since used as a reinforcing agents. However, those materials are not well welcomed due to environmental concerns since mostly obtained from synthetic ways. Therefore, green material based filler for composite fabrication have attracted recently.

Although a number of green material are found in the environment, the most encountered green material is nanocellulose [2-5]. Nanocellulose which consisted of β -1,4 anhydroglucose monomer units revealed superior mechanical properties and biodegradability. And those are abbreviated as nano fibrillated cellulose (CNF), nano crystalline cellulose (CNC) and bacterial cellulose (BC) after isolating from vegetables or synthesizing from bacteria via with different process [6,7]. Of these types, CNF has gained more interest since reveals a

higher aspect ratio, and gerater interfacial adhesion. Thus, they are used in 3D bioprinting, membrane, medicine, polymer and electronic film [8].

The other important player in the composite production is resin. There are a variety of resins used in the composite industry. Unsaturated polyesters (UPs) which consisted of phthalic acid, maleic anhydride (C=C double bond), styrene (curing agent), toluene (solvent), and ethylene glycol (viscosity modifier), are the most widely used types since having cost-effective, ease of use, and superior mechanical properties. Thus, UP is preferred much more in the applications such as adhesives, automotive components, boat hulls, aircraft and appliance components.

Recently, pooling the polyester with biodegradable green material is of great interest. Therefore, several studies have been conducted to give detailed information on this aspect [9]. First study was carried out by Chirayil et al. that they produced CNF based PE composites to reveal their mechanical properties. They observed that CNF enabled higher tensile strength due to the fact that transferred the stress to the CNF effectively [10].

In another study, rheological parameters were investigated in detail by the same group that CNF's shear thinning behaviour was not initially changed during interaction whereas it was converted to Newtonian behaviour in the high shear. Also, lower gelation time was determined after CNF. This circumstance reveals that the CNF enabled faster cure-accelerating ability by carrying out early network formation [11]. In other study, Ansari et al. [12] conducted study to investigate CNF based PE composite's mechanical and thermal properties. The produced composites, at the high concentration, gave higher glass transition temperature, modulus, ductility as well as fracture toughness. Also, the study revealed that CNF based PE composites, having 40 wt %, was able to be produced with high thermal and mechanical properties [12]. Lavorati et al. [13] joined the trend and produced polyester composites having CNF. They observed that CNF enabled higher dynamic-mechanical properties as well as thermal stability whereas water absorption was not influenced significantly [13]. In the present study, CNF-PE composites were prepared with different CNF ratios (0.5 wt. %, 1 wt. % and 1.5 wt.%) via compression molding method. Afterward, chemical, thermal, mechanical and morphological properties of the produced CNF-PE composites were investigated.

2. Materials and Methods

2.1 Materials

In the present study, the orthophthalic acid resin (PE) (1.12 g/cm^3 , 66% solid content, Polipol 3562-SR, Turkey) . methyl ethyl keton peroxide (MEKP) (ER 59, Akperox, Turkey) and cobalt octaoate (CoOc) (RC88, Akkobalt, Turkey) was chosen as matrix, initiator and catalyst, respectively. The used CNF were prepared and produced with the method which explained before studies by applying enzymatic hydrolysis and high-pressure homogenizing (M-110Y, Microfluidics Corp., USA) [14].

2.2 Design of The Experiments

In the present study, CNF based polyester composites were fabricated via compression molding method with different ratios 0.5 wt. %, 1 wt. % and 1.5 wt.% in certain conditions (those are abbreviated as a PE-0,5 CNF, PE-1 CNF and PE-1,5 CNF). Afterward, chemical, thermal, morphological and mechanical

properties were investigated with Fourier Transform Infrared Spectroscopy (FT-IR), thermogravimetric analysis (TGA), scanning electron microscope (SEM), and Universal testing machine (UTM), respectively.

2.3 Composite Fabrication

Composite fabrication was carried out in three stages. In the first stage, orthophthalic resin and CNF were mixed and sonicated in the ultrasonic homogenizer (1 min at 35 KHz) (Bandelin, RK 100 H, Germany) to gain the homogeneity. In the second stage, MEKP, and CoOc were poured on the PE resin found in the beaker with micropipette (volume ratio of 100:1:1). Then, the former mixture was stirred in the magnetic stirrer (30 sec. at 300 rpm). The mixture was moved to the ultraturrex disperser to improve homogeneity and mixed again (30 sec. min at 800 rpm) (Heidolph, Hei TORQUE 100, Germany) before reaching resin's gelling time. Finally (as last stage), the prepared resin mixtures were moulded in the glass molds ($25\text{cm} \times 45\text{cm} \times 10\text{mm}$) to form CNF based PE composites and kept according to ISO 291 (4 h, $20 \pm 2^\circ\text{C}$ and one week, at 80°C). Pre-mold, release agent (Poliya, Polivaks SV-6, Turkey) were applied to the molds. Afterward, the produced composites were cut in laser cutting device for mechanical analysis with controlled levelling. Experimental demonstration was given in Figure 1.



Figure 1. Experimental demonstration.

- a: Interaction of PE resin, initiator and catalyst
- b: Addition of CNF filler
- c: Preparation of dog-bone shaped specimen
- d: Analysis of tensile strength
- e : Analysis of compressive strength

2.4 Composite Preparation

Chemical interaction carried out between CNF and PE was given in Figure 2.

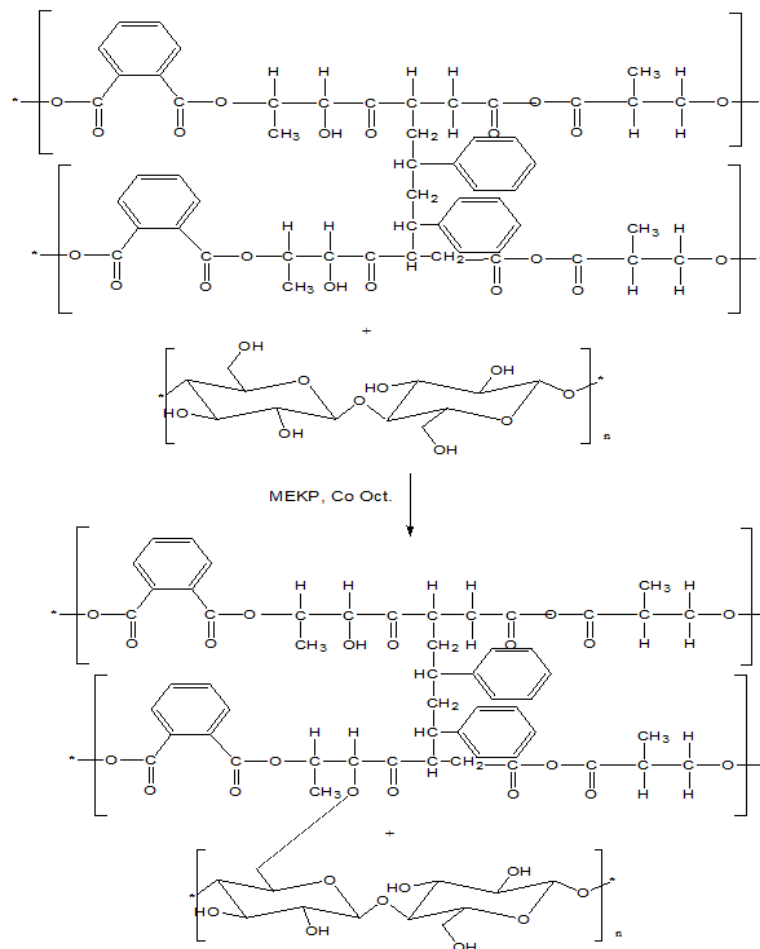


Figure 2. Chemical interaction between CNF and PE.

2.5 Chemical Analysis

The FTIR device (IR Prestige-21, Shimadzu, Japan) with attenuated total reflectance (ATR) attachment was used to investigate chemical interaction carried out between CNF and PE ($4000\text{-}600\text{ cm}^{-1}$, 20 scans, resolution of 4 cm^{-1}).

2.6 Thermogravimetric Analysis (TGA)

For TGA, composites were placed into Pt pan as 5-10 mg following dried overnight. Afterward temperature was applied to composites from room temperature to $800\text{ }^{\circ}\text{C}$ (heating rate of $10\text{ }^{\circ}\text{C}/\text{min}$, N_2 atm) (DTG 60, Shimadzu, Japan).

2.7 SEM

For determination of the morphology, the specimens were placed with tweezers onto a substrate with carbon tape and then coated with a thin layer of Au/Pd for

taking surface and cross-section pictures at SEM (FEI, Quanta 250, Netherland).

2.8 Mechanical analysis

For determination of the mechanical properties, tensile strength and compressive strength were applied to specimens in the universal testing machine (100 kN, BESMAK, Turkey). Tensile strength was performed until tensile failure occurred (cross-head speed of $5\text{ mm}/\text{min}$, $25\text{ }^{\circ}\text{C}$). Compressive test was carried out (loading speed of $41\text{ MPa}/\text{min}$, $25\text{ }^{\circ}\text{C}$) according to ASTM C 579-01[15].

3. Results and Discussion

3.1 Chemical Characterization

The FTIR spectra of the composites was given in Figure 3.

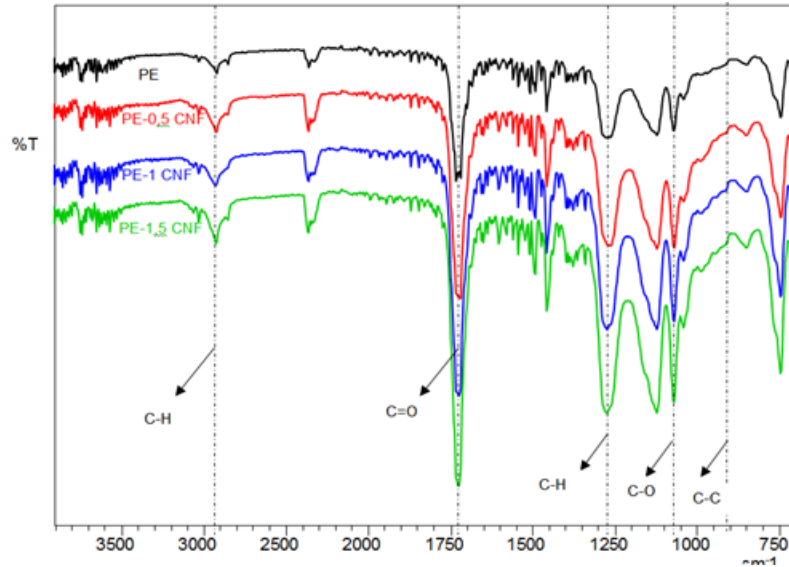


Figure 3. FTIR spectra of PE, PE+0,5 CNF, PE+1 CNF, PE+1,5 CNF.

The most observed vibrations sourced from methylene stretching were seen at 2920 cm^{-1} (asymmetric) and 2910 cm^{-1} (symmetric) for all composites. $\text{C}=\text{O}$ asymmetric vibration, which has only maleic anhydride, and $\text{C}-\text{O}$ symmetric vibration was seen at 1727 cm^{-1} and 1118 cm^{-1} , respectively. The considerable vibration in relation to the CNF were observed between 1000 cm^{-1} and 1200 cm^{-1} . Those vibrations is attributed to $\text{C}-\text{O}-\text{C}$ vibrations in the cellulose intra-molecular and inter-molecular structure. The vibration at 1160 cm^{-1} for CNF

is due to $\text{C}_1-\text{O}-\text{C}_5$ that give an insight about asymmetric bridge stretching. The $\text{C}_1-\text{O}-\text{C}_4$ vibration which give insight about the glycosidic main structural deformation were seen at 1029 cm^{-1} [16].

3.2 Thermal Characterization

TGA and DTG (derivative of TGA) analysis were carried out and the obtained thermograms were given in Figure 4.

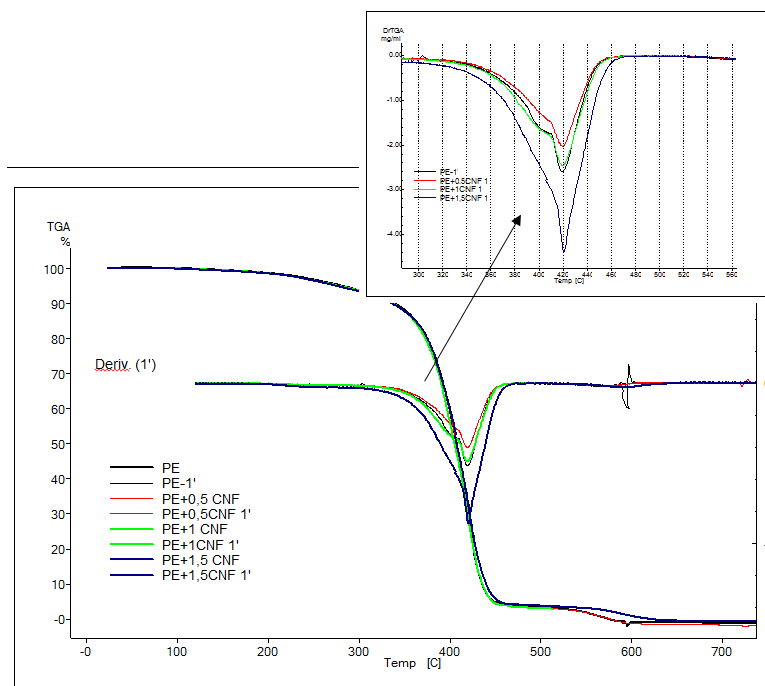


Figure 4. Thermogravimetric analysis test results.

All composites revealed similar thermal degradation trend. Mass loss of composites was investigated in the two regions: 25°C-200°C and 200°C-480°C to elucidate the degradation and thermal stability properties. The first region (25°C-200°C) gives an insight about low molecular weight as well as humidity whereas second region (200°C-480°C) give an insight about main structure degradation. It was observed that there was no considerable alteration among thermograms of the composites. When checked the derivative giving more detailed insight about thermal stability, two thermal degradations were seen for each composites with different degradation temperature. Those revealed that thermal stability improved with the CNF and the higher value was seen in the PE+1.5 CNF as 420.93 °C whereas lower value was seen in the PE as 419.26 °C. Shimazaki et al. conducted a study revealing the CNF effect favorably on PE's thermal stability. They claimed that organic fillers posed higher thermal stability [17]. In the present study, similar results were obtained as they found. This circumstance can be explained that the CNF fillers enabled chain mobility within the composite and this caused higher thermal stability [18].

3.3 Mechanical Properties

Tensile strength results of the composites were given in Figure 5.

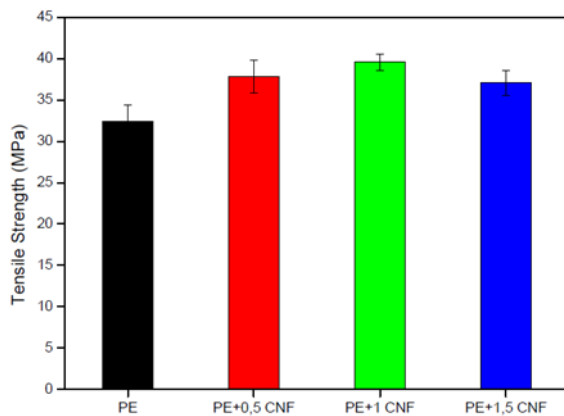


Figure 5. Tensile Strength values of the PE, PE+0.5 CNF, PE+1 CNF, PE+1.5 CNF.

Figure 5 reveals that tensile strength value of the PE+0.5CNF composite has 37.82 MPa, PE+1CNF has 39.6 MPa value, and PE+1.5CNF 37.7 MPa whereas the neat PE has 32.4 MPa. It was also observed that PE+0.5 CNF and PE+1.5 CNF values had close values to each other and the highest increment was seen in the PE+1CNF with 22%. Overall, with incorporation of the CNF, tensile strength of the composites increased. This circumstance could be ascribed to the CNF 3D network

structure as well as high aspect ratio. Because, this structure is enabled greater stress transfer for sticking the matrix particles to the filler surfaces. However, it was observed that the highest value was not seen in the PE+1.5 CNF. This circumstance may be ascribed in entanglement of CNF in the PE matrix. Therefore, it can be said that the most suitable CNF filler ratio in the PE matrix for forming CNF based PE is the 1% CNF.

Compressive strength is of important parameters for evaluating mechanical property of the composites. The obtained values were given in Figure 6.

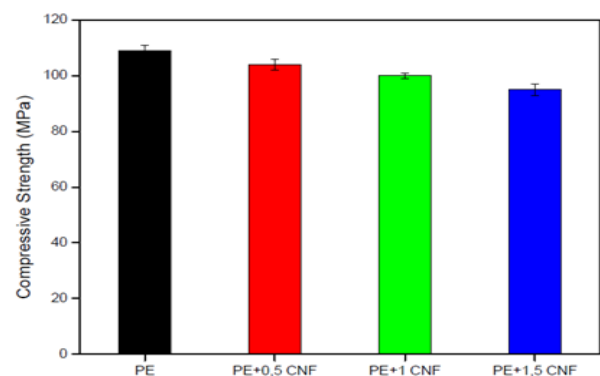


Figure 6. Compressive strength mean values of the PE, PE+0.5 CNF, PE+1 CNF, PE+1.5 CNF.

When Figure 6 was examined, the compressive strength value of the composites lowered with CNF and the progressively lower value was obtained. And, the lowest value was seen in the PE+1.5CNF composite with decreasing of 16 %. These results were as expected since PE resin which gained thermoset qualification has high elastic modulus and enabled the higher compressive strength values whereas bio-based CNF fibers caused lower. This is probably ascribed to the low density of CNF and the low hardness that can not carry the higher load. This circumstance was also explained by the buckling effect and weak interface by Sari et al. They studied the compressive strength of the fiber based PE composites and they observed lower compressive strength value as the fibers content increased. This is ascribed to the weak interface bonds between fibers and PE as well as the increased damage of the fibers sourced from buckling of the composites.

3.4 Morphological Characterization

The obtained SEM pictures were given in Figure 7 as surface and cross-section to reveal morphological alterations.

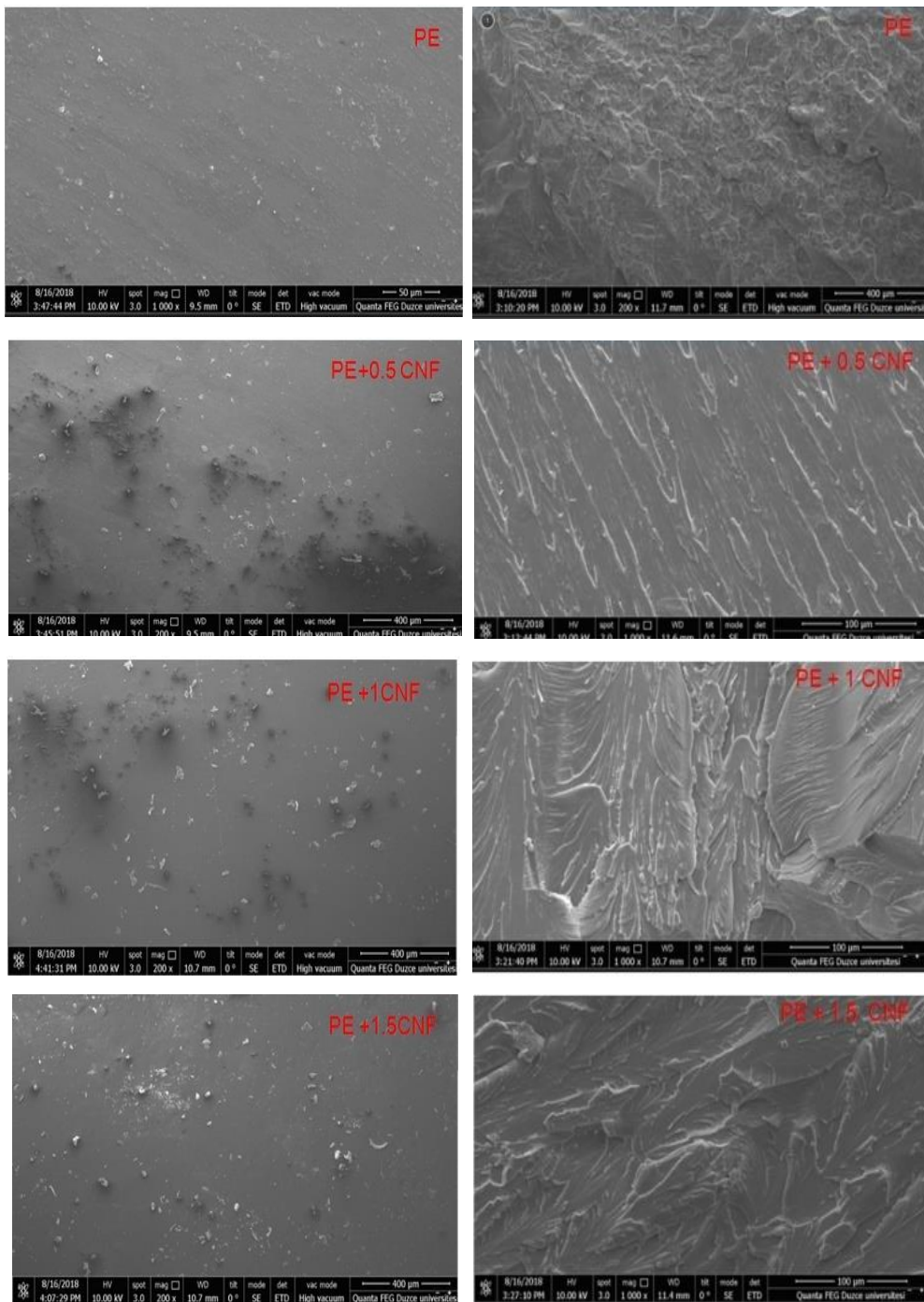


Figure 7. SEM pictures of the PE, PE+0.5 CNF, PE+1 CNF, and PE+1.5 CNF (Pictures were given as surfaces and cross section, respectively)

SEM surface images reveal that all of the CNF mostly dispersed homogeneously in the PE resin matrix. However, some minor agglomerations were observed in the PE-CNF composites that this agglomeration was increased progressively with CNF content. This phenomena reveal that there is no uniform distribution of CNF filler which resulted from overlapping of CNF

filler. However, there has not been considerable cracking and void in the structures.

In the cross-sections images, a layered morphology having a different orientation can be discerned. Besides, any signs related to CNF agglomeration were not observed. In addition, no individual CNF fibrils were also seen.

The images reveals the local plastic deformation was carried out in the composites. Therefore, it can be said that CNF filler's having low hardness can not carry to higher load. However, some cracking carried out since eluding the CNF from the surface of the matrix towards to sliding side following increasing load.

4. Conclusion

This study reports the effects of bio based CNF fillers on the chemical, thermal, mechanical, and morphological properties of PE composites. Considerable conclusions from the present study are as follows:

1. The neat PE and its composites with CNF were successfully produced in the presence of initiator and catalyst.
2. The CNF filler caused the minor chemical shifts in obtained PE composites.
3. CNF based composites showed higher thermo-stability.
4. The CNF was not dispersed homogenously and some regional agglomeration was observed.
5. The CNF filler enabled higher tensile strength over the neat PE due to the fact able to stress transfer.
6. The CNF filler caused lower compressive strength over the neat PE due to low hardness as well as the buckling effect.

This study reveals the applicability of CNF filler as reinforcing for higher tensile strength value in the PE polymer composites. Therefore, it can be said that this type of fiber is able to apply in the production of the PE based pipe which has glass reinforced plastic (GRP) industry.

Author's Contributions

The Authors contributed to the study as follows,

Bayram Poyraz: Investigation, Writing- Original draft preparation, Methodology, Formal analysis

Şevki Eren: Investigation, Methodology, Formal analysis.

Serkan Subaşı: Methodology and Preparation

Ayhan Tozluoğlu: Methodology and Preparation

Ethics

There are no ethical issues after the publication of this manuscript.

References

- [1]. Kalkan, E, Karakışla, MM, Saçak, M. 2018. Polypyrrole and silver particles coated poly (ethylene terephthalate) nonwoven composite for electromagnetic interference shielding. *Journal of Composite Materials*, 52(10): 1353-1362.
- [2]. Eichorn, S and Dufresne, A. 2018. Review: current international research into cellulose nanofibers and nanocomposite. *Journal of Material Science*, 45: 1-33.
- [3]. Klemm, D, Kramer, F, Moritz, S, Lindström, T, Ankerfors, M, Gray, D, Dorri, A. 2011. Nanocellulose: a new family of nature-based materials, *Angewandte Chemie International Edition*, 50: 5438–5466.
- [4]. Bismarck, S, Mishra, T, Lampke, M, Misra, LT. 2005. Plant fibers as reinforcement for green composites, in Mohanty AK (Ed.), *Natural Fibres, Biopolymers, and Biocomposites*, CRS Press.
- [5]. Spřrminš, E. 2006. Mechanical Properties of Flax Fibers and Their Composites, 971, Luleå University, Luleå, Sweden.
- [6]. Güven, O, Monteiro, S, Mourac, E, Drelich, J. 2016. Re-Emerging Field of Lignocellulosic Fiber – Polymer Composites and Ionizing Radiation Technology in their Formulation, *Polymer Reviews*, 56(4): 702-736.
- [7]. Lin, N and Dufresne, A. 2014. Nanocellulose in biomedicine: current status and future prospect, *European Polymer Journal*, 59: 302–325.
- [8]. Kim, DY and Stecki, AJ. 2010. Electrowetting on paper for electronic paper display, *ACS Applied Material Interaction*, 2(11): 3318–3323.
- [9]. Haghdan, S, and Smith, GD. 2016. Natural fiber reinforced polyester composites: A literature review *Journal of Reinforced Plastics and Composites*, 34(14): 1179-1190.
- [10]. Cintil, JC, Jithin, J, Lovely, M, Joachim, K, Sabu, T. 2014. Nanofibril reinforced unsaturated polyester nanocomposites: Morphology, mechanical and barrier properties, viscoelastic behavior and polymer chain confinement, *Industrial Crops and Products*, 56: 246–254.
- [11]. Cintil, JC, Jithin, J, Lovely, M, Hassan, PA, Miran, M, Sabu, T. 2014. Rheological behavior of nanocellulose reinforced unsaturated polyester nanocomposite, *International Journal of Biological Macromolecules*, 69: 274–281.
- [12]. Farhan, A, Mikael, S, Lars, B. 2015. Nanostructured biocomposites based on unsaturated polyester resin and a cellulose nanofiber network, *Composites Science and Technology*, 117: 298-30.
- [13]. Alessandra, L, Lisete, CS, Ademir, JZ. 2016. Dynamic-mechanical and thermomechanical properties of cellulose nanofiber/polyester resin composites, *Carbohydrate Polymers*, 136: 955–963.
- [14]. Poyraz, B, Tozluoğlu, A, Candan, Z, Demir, A. 2017. Influence of PVA and silica on chemical, thermo-mechanical and electric properties of Celluclast treated nano fibrillated cellulose composites, *International Journal of Biological Macromolecules*, 104: 384–392.
- [15]. ASTM (2012) C579-18. Standard test methods for compressive strength of chemical-resistant mortars. grouts. monolithic surfacings and polymer concretes. ASTM International, USA.
- [16]. Carrillo, F, Colom, X, Sunol, J, Saurina, J. 2004. Structural FTIR analysis and thermal characterization of lyocell and viscose-type fibers. *European Polymer Journal*, 40(9): 2229-2234.
- [17]. Shimazaki, Y, Yasuo, M, Yoshitaka, T, Masaya, N, Kentaro, A, Shinsuku, I, Hiroyuki, Y. 2007. Excellent thermal conductivity of transparent cellulose nanofiber/epoxy resin nanocomposites. *Biomacromolecules*, 8(9): 2976-2978.
- [18]. Zhua, J, Suying, W, Rahul, P, Ran, D, Ashwini, SK, Andrew, W, Zhang, G. 2011. Ionic liquid assisted electrospinning of quantum dots/elastomer composite nanofibers. *Polymer*, 52: 1954-1962.
- [19]. Sari, NH, Pruncu, CI, Sapuan, SM, Ilyas, RA, Catur, AD, Suteja, S, Pullen, G. 2020. The effect of water immersion and fibre content on properties of corn husk fibres reinforced thermoset polyester composite. *Polymer Testing*, 91: 106751.